Summer 8-15-2019

Toward Improved Understanding of Black and Brown Carbon Radiative Impacts over South Asia

Apoorva Pandey
Washington University in St. Louis

WASHINGTON UNIVERSITY IN ST. LOUIS

School of Engineering and Applied Sciences
Energy, Environmental and Chemical Engineering

Dissertation Examination Committee:
Rajan K. Chakrabarty, Chair
Raymond E. Arvidson
Pratim B. Biswas
Jay R. Turner
Brent J. Williams

Toward Improved Understanding of Black and Brown Carbon Radiative Impacts over South Asia

by
Apoorva Pandey

A dissertation presented to
The Graduate School
of Washington University in
partial fulfillment of the
requirements for the degree
of Doctor of Philosophy

August 2019
St. Louis, Missouri

Table of Contents

List of figures iv
List of tables ix
Acknowledgments x
Abstract xii
Chapter 1: Background and motivation 1
1.1. Black and organic carbon (BC and OC) aerosols: optical and chemical properties 4
1.2. Aerosol light absorption: measurement techniques and models 7
1.3. Aerosol emissions in South Asia 10
References 14
Chapter 2: Research objectives 19
References 23
Chapter 3: Accurate morphological representation of BC in optical parameterizations 25
3.1. BC optical properties as functions of measurable equivalent diameters 27
3.1.1. Relationships between fractal parameters and equivalent diameters of aggregates 28
3.1.2. Numerically estimated optical cross-sections and asymmetry parameter 31
3.2. Relationships between scattering directionality parameters for BC aggregates 35
3.2.1. The scattering phase function and definitions of scattering directionality 36
3.2.2. The Henyey-Greenstein phase function 39
3.2.3. Empirical relationships between the scattering directionality parameters 41
References 47
Chapter 4: Aerosol emission factors from field study of cookstove emissions in India 49
4.1. Experimental and data analysis techniques 50
4.2. Emission factors by fuel and combustion phase 58
4.3. Average emission factors by fuel category; comparison with previous studies 62
4.4. Thermal carbon fractions from TOR analysis 67
4.5. Insights from real-time measurements 68
4.6. Inventoried emissions for biomass cookstoves in India 70
References 72
Chapter 5: Estimating aerosol-phase light absorption from filter-based optics 75

5.1. Filter artifact correction literature 76
5.2. Significance of Teflon filter samples 80
5.3. Two-stream radiative transfer model of a filter-particle system 82
5.4. Experimental methods 89
5.5. Empirical correction scheme for filter artifacts 95
References 101
Chapter 6: Constraining OC contribution to light absorption by cookstove emissions 104
6.1. Attributing aerosol light absorption to OC and EC 105
6.2. Preliminary study of light absorption by cookstove OC emissions 108
6.2.1. Sampling and analysis 108
6.2.2. Appearance of filter samples and deposited particles 115
6.2.3. Absorbance and MAC values of PM, BC and OC 116
6.3. Analysis of comprehensive field study samples with updated filter correction 121
6.3.1. Sampling and analysis 121
6.3.2. Absorption emission factors and light absorption emissions of BC and OC 124
6.3.3. Intensive optical properties of OC and their radiative impact 127
6.4. Comparison with findings in literature 129
References 133
Chapter 7: Conclusions 138
7.1. BC optical parameterization 138
7.2. Aerosol emissions from biomass cookstoves 139
7.3. Filter artifact correction for UV-vis spectroscopy on Teflon membrane filters 140
7.4. Light absorption by cookstove OC emissions 141
References 143
Appendix 144
A1. Two-stream radiative transfer model 144
A2. List of aerosol emission factors by fuel and burn phase. 149
A3. Radiative forcing efficiency of cookstove emissions: probability distributions 151

List of figures

Figure 1.1: Direct and indirect aerosol climate effects and feedback loops. Source: Pöschl (2005). 2
Figure 1.2: Radiative forcing relative to 1750, categorized by pollutant type. Source: Stocker et al. (2013). 3
Figure 1.3: Continuum of carbonaceous aerosol properties. Source: Pöschl (2003). 6
Figure 1.4: Imaginary part of OC refractive index, at 550 nm wavelength observed from biomass combustion and controlled benzene/toluene combustion. Adapted from Saleh et al. (2018). 7
Figure 1.5: The photoacoustic effect showing that the (A) incident radiation absorbed by the particle (B) causes the particle to heat up, in turn (C) heating the surrounding air and generating a (D) pressure disturbance that is detected as a sound wave. Source: Moosmüller et al. (2009). 8
Figure 3.1: Variation of (a) C_{scat} (μm^2), (b) C_{abs} (μm^2), and (c) g, with mobility diameter, d_m (μm) of soot aggregates with D_f equal to 1.8 (fresh) and 2.6 (aged). 33
Figure 3.2: Variation of (a) C_{scat} (μm^2), (b) C_{abs} (μm^2), and (c) *g*, with mass equivalent diameter, d_{me} (μm) of soot aggregates with D_f equal to 1.8 (fresh) and 2.6 (aged). 34
Figure 3.3: Variation of (a) C_{scat} (μm^2), (b) C_{abs} (μm^2), and (c) *g*, with vacuum aerodynamic diameter, d_{Va} (μm) of soot aggregates with D_f equal to 1.8 (fresh) and 2.6 (aged)... 34
Figure 3.4: Illustration of a scattered waveform and the scattering angle relative to the incident radiation. 36
Figure 3.5: Normalized phase function S_{11} at 550 nm wavelength for D_f = 1.9 black carbon aggregates with varying (A) monomer diameter, (B) number of monomers, and (C) refractive index. For (A) and (B), the refractive index was fixed at 1.95-0.79i. For (B) and (C), the monomer diameter was fixed at 50 nm. For (A) and (C), the number of monomers was fixed at 32. 38
Figure 3.6: Scatter-plots of asymmetry parameter, g (panels A, C), and upscatter fraction, β (panels B, D), versus hemispherical backscattering fraction, *b*, for D_f = 1.9 and D_f = 3 aggregates, with varying monomer diameters. The number of monomers, refractive index and wavelength were fixed at 32, 1.95-0.79i, and 550 nm, respectively. 41
Figure 3.7: Scatter-plots of asymmetry parameter, g (panels A, C), and upscatter fraction, β (panels B, D), versus hemispherical backscattering fraction, *b*, for D_f = 1.9and D_f = 3 aggregates, with varying number of monomers. The monomer diameter, refractive index and wavelength were fixed at 50 nm, 1.95-0.79i, and 550 nm, respectively. 42

Figure 3.8: Relationships between (A) asymmetry parameter, *g*, and hemispherical backscattering fraction, *b*, (B) upscatter fraction, *β*, and *b*, and (C) *β* and *g*, at 550 nm wavelength, for D_f = 1.9 and D_f = 3 aggregates. The fits *g(b)*, *β(b)* and *β(g)* are given in Equation 3.15-3.17. 44
Figure 3.9: Scatter plots of simple forcing efficiency (W/g/nm) at 550 nm for upscatter fraction, *β*, estimated from a range of (A) backscatter fraction, *b*, values, using the HG approximation (equation 3.13) and *T*-matrix based relationship (equation 3.16), and (B) asymmetry parameter, *g*, values, using the HG approximation (equation 3.14) and *T*-matrix based relationship (equation 3.17). In equation 3.17, *g* was from *T*-matrix calculations for aggregates of different sizes, while Mie theory-based estimates of *g*, for equivalent spheres, were used in equation 3.14. 45
Figure 4.1: Traditional one-pot mud *chulha* used in this work..... 50
Figure 4.2: Schematic layout (top-view) of the kitchen. 55
Figure 4.3: Schematic representation of the experimental setup. S1 and S2 denote the position of the wireless optical sensors. 56
Figure 4.4: Raw signals from the PM sensors located at the sampling probe (Sensor1) and the Minivol $PM_{2.5}$ sampler (Sensor2) during one cooking test. 57
Figure 4.5: Box plots of (a) $PM_{2.5}$ emission factors, (b) OC emission factors, and (c) EC emission factors. All emission factorss are expressed in g-pollutant per kg of fuel burnt. Boxes denote lower and upper quartiles; whiskers are 1.5 times the interquartile ranges of the upper and lower quartiles. The numbers above the error bars in panel (c) indicate the number of samples for each fuel. 59
Figure 4.6: Fuel-wise average values of (a) $PM_{2.5}$ emission factors, (b) OC/EC ratios, (c) OC emission factors, and (d) EC emission factors, categorized by observed combustion phases. All emisssion factors are expressed in g-pollutant per kg of fuel burnt. One-sided error bars are shown to denote one standard deviation from the mean. The numbers above the error bars in panel (d) indicate the number of samples for each fuel and combustion phase. 60
Figure 4.7: Fuel-wise average values of CO emission factors categorized by observed combustion phases. Emisssion factors are expressed in g-pollutant per kg of fuel burnt. One-sided error bars are shown to denote one standard deviation from the mean. 61
Figure 4.8: Comparisons of (a) CO vs $PM_{2.5}$, EFs and (b) OC/EC ratios vs modified combustion efficiency (MCE) values. 61
Figure 4.9: Average $PM_{2.5}$ emission factors and OC/EC ratios for the three fuel categories in this study, compared with relevant studies. Error bars for values estimated in this study denote 95% confidence intervals based on standard errors of the means. Error bars for other studies are the bounds reported within those studies. 63

Figure 4.10: The relationship between OC and $PM_{2.5}$ emission factors from all the studies listed in Table 4.3. All WBT based measurements (lab or field) are grouped. The dashed line represents an ordinary least-squares fit (R^2=0.92)..... 67
Figure 4.11: Fraction of total carbon emissions contributed by the IMPROVE_A thermal carbon fractions. 68
Figure 4.12: Real-time measurements of (A) Sidepak $PM_{2.5}$ mass concentrations in $\mu g/m^3$, and (B) CO concentrations (solid) in and CO_2 concentration (dashed), both in ppm. 70
Figure 5.1: Transmission and reflection of radiation through a one-dimensional, uniformly multiple-scattering medium. 82
Figure 5.2: Two-layer model of a filter sample consisting of an aerosol laden layer 'l' and a clean layer 'f'. 84
Figure 5.3: Modeled values of filter optical depth measures (OD_c, *ATN* and OD_s) with increasing aerosol optical depth ($\tau_{a,s}$) of deposited highly absorbing (SSA=0.3) or highly scattering (SSA=0.95) aerosols. Fixed blank optics were assumed. 87
Figure 5.4: Change in sample-side reflectance as a function of the corresponding change in transmittance for predominantly absorbing (SSA=0.3) and scattering (SSA=0.95) aerosol types when blank optics are fixed. 88
Figure 5.5: Same as Figure 5.4 but for different assumed values of aerosol fractional penetration depth χ. 89
Figure 5.6: Schematic representation of the experimental setup. Inlet to the semi-volatile organic compound denuder was taken from either the chamber sampling port or the hood. IPN stands for integrated photoacoustic-nephelometer spectrometers. 91
Figure 5.7: Modeled filter optical depth (OD_s) for absorption optical depth and single scattering albedo values of the aerosols sampled in this study compared with the corresponding filter measurements. A 1:1 line is shown in red. The average ratio of modeled to measured OD_s is 0.79. 96
Figure 5.8: Relationship between *in-situ* aerosol optical depth ($\tau_{a,s}$) and filter optical depth OD_s for all (n=75) samples, measured at 375, 405 and 532 nm (N=225 data points). The best fit curve is given by equation 5.24, with R^2 = 0.87. The black perforated line has a fixed slope of 0.67 per Zhong and Jang (2011)). Uncertainties (1 standard deviation) in OD_s ranged 2-5%, while those in $\tau_{a,s}$ were 5-10%. 97
Figure 5.9: The relationship between experimentally measured *in-situ* aerosol optical depth ($\tau_{a,s}$) and modeled values of filter optical depth measures (OD_c, *ATN* and OD_s). Blank optics were randomly generated for each sample point from a normal distribution with mean=0.7 and standard deviation=0.02. 97
Figure 5.10: Relationship between *in-situ* aerosol optical depth ($\tau_{a,s}$) and measured values of filter optical depth measures OD_c and OD_s for a subset of 54 filter samples, measured at 375, 405 and 532 nm (N=162 data points). Uncertainties were as in Figure 5.8. 98

Figure 5.11: Correction factor C for filter artifacts as a function of single scattering albedo of the deposited aerosols. Error bars show one standard deviation around the mean. The numbers in parentheses denote the number of data points in each bin. 99
Figure 6.1: Absorption spectrum for a sample of dung emissions is deconvoluted by assigning all absorption at wavelengths greater than λ_t (chosen as 700 nm here) to BC and extrapolating BC absorption at smaller wavelengths using a fixed BC AAE (1.2 in the figure). 108
Figure 6.2: Average LAOC ABS values at 350 nm wavelength as functions of BC AAE for fuel-wood, agricultural residue, dung cake and mixed fuel..... 113
Figure 6.3: Images of Teflon filter samples of aerosols from the combustion of (A) fuel-wood, (B) agricultural residue, (C) dung-cake and (D) mixed fuel in traditional cookstoves..... 115
Figure 6.4: TEM images of (A) an amorphous OC particle typically emitted from fuels in this study and (B) OC particle with co-emitted BC aggregate. 116
Figure 6.5**:** Average biomass ABS values for (A) $PM_{2.5}$ emissions, and their (B) BC and (C) LAOC components. Error bars represent 95% CI around the means, based on the standard errors of the means. 116
Figure 6.6: Fuel-wise $PM_{2.5}$ MAC values (m^2/g) as a function of the wavelength of incident radiation. The error bars represent 95% CI around the means, based on the standard errors of the means. 119
Figure 6.7: Fuel-wise OC MAC values (m^2/g) as a function of the wavelength of incident radiation. The error bars represent 95% CI around the mean. Symbols represent the mean OC MAC values reported from wood burning in literature [circle = Kirchstetter et al. (2004) square = Washenfelder et al. (2015); triangle = Lack et al. (2012); star = Chen (2011)]. 120
Figure 6.8. (A) Fraction of the total aerosol absorbance attributed to light absorbing OC as a function of wavelength. (B) Fraction of solar radiation (in the 300-900 nm range) absorption (Wm^{-2} aerosol) attributed to LAOC, per biomass fuel type. Error bars represent 1 standard error about the mean. 121
Figure 6.9: $PM_{2.5}$ absorption emission factors, or AEF_{PM} in m^2kg^{-1} fuel consumed, (A) grouped by observed combustion phase: boxes denote the upper and lower quartiles and whiskers denote 1.5 times the interquartile range, outliers are shown as red + symbols, number of samples for each category are specified above the whiskers and (B) shown as a histogram of all samples, overlaid by a fitted lognormal distribution. 125
Figure 6.10: Absorption emission factors in m^2kg^{-1} fuel consumed: (A) AEF_{OC} grouped by observed combustion phase: boxes denote the upper and lower quartiles and whiskers denote 1.5 times the interquartile range, outliers are shown as red + symbols, number of samples..... 126

Figure 6.11: Spatial distribution of annual emissions expressed as light absorption cross-section (AE: Gm^2y^{-1}) at 550 nm attributed to (A) OC and (B) BC components of cookstoves emissions in India. BC AAE = 1.2 was used. 127
Figure 6.12: (A) The contribution of OC light absorption to MAC_{PM} at 550 nm, f_{OC}, decreases with increasing values of MAC_{PM}. This implies that (B) $MAC_{PM.no\text{-}OC}$ is positively correlated with MAC_{PM}. Linear fits between the two parameters are in Table 6.2. 128
Figure A1.1: Transmission and reflection of radiation through a one-dimensional, uniformly multiple-scattering medium. 144
Figure A1.2: Modeled filter optical depth (OD_s) as a function of single scattering albedo (SSA) and aerosol optical depth ($\tau_{a,s}$) of deposited aerosols. 148
Figure A3.1: Probability distributions of (A) MAC_{PM} and (B) $MAC_{PM,no\text{-}OC}$ for all samples in this study.. 151
Figure A3.2: Probability distributions of simple forcing efficiency of cookstove particulate emissions over (A) ground and (B) snow. Forcing was calculated with and without OC light absorption, with a fixed MSC =1.5 m^2g^{-1}.. 152
Figure A3.3: Probability distributions of simple forcing efficiency of cookstove particulate emissions attributed to OC light absorption over (A) ground and (B) snow. 153

List of tables

Table 3.1. Estimated equivalent aerosol diameters (nm) for fresh and aged soot aggregates as a function of monomer number (N) 31
Table 3.2. Best fit empirical equations connecting the mobility diameter, d_m (in μm) and the optical properties of fresh and aged SA. 32
Table 3.3. Best fit empirical equations connecting the mass equivalent diameter, d_{me} (in μm) and the optical properties of fresh and aged SA. 33
Table 3.4. Best fit empirical equations connecting the vacuum aerodynamic diameter, d_{Va} (in μm) and the optical properties of fresh and aged SA. 33
Table 4.1: Elemental composition and moisture content of the biomass fuels in this study. 52
Table 4.2: List of cooking experiments conducted during the 10-day intensive study period. Abbreviations for Indian states: U.P. = Uttar Pradesh, Raj. = Rajasthan, A.P. = Andhra Pradesh, Chh. = Chhattisgarh. 53
Table 4.3: Summary of reported mass emission factors of $PM_{2.5}$, EC and OC emissions from biomass cookstoves. All emission factors are expressed as mean (standard deviation). 65
Table 5.1: Number of burns conducted, and filter samples collected for each fuel type and combustion phase in this study. Intrinsic optical properties of emissions from each study condition are also given. 92
Table 5.2: Particle and filter properties for artifact correction. 95
Table 6.1: Ratio of OC to BC mass and optical properties (MAC and AAE) for aerosol samples by biomass fuel type. 118
Table 6.2: Slope (m), intercept (c) and adjusted R^2 for the linear fits: $MAC_{PM,no\text{-}OC}$ =m* MAC_{PM} + c. 128
Table 6.3: Simple forcing efficiency of cookstove emissions attributed to OC light absorption (in Wg^{-1} $PM_{2.5}$), MAC_{OC} (in Wg^{-1} PM), AAE_{OC}, and contribution of OC to $PM_{2.5}$ light absorption (percentage of total absorption). These estimates depend on the value of BC AAE used in absorption apportionment. All values are reported as mean±1 standard deviation. 129
Table 6.4: Summary of optical cross-sections of particulate emissions from biomass cookstoves 131
Table A2.1: Emission factors of $PM_{2.5}$, CO, OC and EC (in g pollutant kg^{-1} fuel) for each test fuel and combustion phase. 149

Acknowledgments

I would first like to thank my advisor Dr Rajan Chakrabarty for his guidance and support throughout my time at Washington University in St Louis. From him, I learned to stay curious and optimistic, finding interesting research opportunities in unexpected places. I deeply admire his creativity and persistence as a researcher and his kindness as a mentor.

Before I started my PhD, two mentors played a big role in my professional development. I sincerely thank Dr Ambuj Sagar and Dr Chandra Venkataraman for inspiring my interest in research and helping me accomplish my goals.

I also thank members of my dissertation committee—Drs. Pratim Biswas, Jay Turner, Brent Williams, Raymond Arvidson—for their time and expertise. They truly lead by example.

Many collaborators made important contributions to the projects on which I have worked. I am especially thankful to everyone involved with the cookstove field study in India: Sameer Patel for his help in planning and executing this project and analyzing the measurements from wireless particle sensors; Dr Shamsh Pervez and his students Madhuri Verma, Jeevan Matawale and Rakesh Sahu at Pt. Ravishankar Shukla University in Raipur, India for all their help in planning and conducting the study and also for their hospitality; Dr Gautam Yadama and Dr Ramesh Raliya for their help in procuring the fuels. In the case of laboratory work, I conservatively estimate that for every hour that yielded something useful, another hour was spent on making mistakes, learning and sometimes hitting dead ends. I am grateful for all the help I got during that process from many current and previous members of my lab: Nishit Shetty, Benjamin Sumlin, Yang Yu, Yuli Heinson and William Heinson. I also thank Alice Hsu, Ester Koh and Thomas Hildebrand for their contributions to my thesis research.

I appreciate my wonderful cohort, many of whom have been great friends: especially Claire Fortenberry, Deanna Lannigan, Jiayu Li, Pai Liu, Tolutola Oyetunde and Nathan Reed. Finally, I thank my husband, Darshit Mehta, for among many other things, always agreeing to proofread.

Apoorva Pandey

Washington University in St. Louis

August 2019

ABSTRACT OF THE DISSERTATION

Toward improved understanding of Black and Brown Carbon radiative impacts over South Asia

by

Apoorva Pandey

Doctor of Philosophy in School of Engineering and Applied Science

Department of Energy, Environmental and Chemical Engineering

Washington University in St. Louis, 2019

Atmospheric aerosols directly affect the Earth's radiative budget by absorbing and scattering solar radiation. Carbonaceous aerosols constitute 20-90% of the global aerosol mass burden and are recognized by the Intergovernmental Panel on Climate Change as important drivers of direct radiative forcing (DRF). Aerosol radiative impacts have been implicated in regional atmospheric warming in South Asia: changing Indian monsoon patterns, and accelerating melting of the Himalayan glaciers. There are systematic global discrepancies between estimates of aerosol absorption optical depths derived from observations and those from climate models. Over South Asia, models predict six times lower aerosol absorption than ground-based observations, leading to a low bias in modeled DRF. To resolve this bias, there is a need to (1) account for relevant emission source types, and associated emission rates, and (2) constrain aerosol optical properties: mass absorption cross-sections (MAC), single scattering albedo (SSA) and scattering directionality parameters (asymmetry parameter or upscatter fraction). To that end, two broad classes of light absorbing carbonaceous aerosols need to be separately dealt with: black carbon (BC) and brown carbon (BrC).

BC is known to strongly absorb visible solar radiation and its optical properties have been characterized using both direct measurements and optical models. BC aerosols exhibit aggregate morphologies, with fractal dimensions of 1.8 and 2.6 for fresh and aged particles, respectively. As a simplification, current climate models usually approximate BC aerosols as volume-equivalent spheres and use analytical solutions (known as the Lorenz-Mie theory) of Maxwell's equations for estimating their optical properties. Recent modeling studies employed the numerically-exact superposition transition-matrix method to compute optical cross-sections of fractal aggregates of varying sizes and fractal dimensions. These studies highlight the effect of morphology on BC optical behavior soot but their findings (expressed in terms of fractal properties) cannot be used directly by aerosol experimentalists and climate modelers. Exploiting the theoretical bases of aerosol sizing techniques, I determined empirical relationships between numerically-exact optical properties of fractal BC particles and their equivalent diameters, that can be measured by common aerosol instrumentation. In a related study, I reported improved relationships between scattering directionality parameters of BC aggregates, and compared them with the canonical equations which did not allow for treatment of particle morphology.

The second branch of my thesis is concerned with light absorbing organic carbon (OC). OC is conventionally modeled as purely light scattering in radiative transfer calculations. However, this approach has been challenged by mounting observational evidence of a class of OC aerosols exhibiting strong absorption in the near ultra-violet wavelengths and little to no absorption in the near-infrared region. This wavelength dependence of absorption leads to a brownish appearance, hence the name brown carbon. Absorption properties of BrC depend on fuel properties and combustion phase (flaming/smoldering): their observed values are source-specific, spanning an order of magnitude in literature. The focus of this part of my research is on the largest source of

OC emissions in South Asia: household biomass cookstoves. I conducted a field study in a household in central India in December 2015 and developed a dataset of emission rates for commonly used biomass fuels from various regions of India, which showed that (1) laboratory cookstove tests underestimated particulate mass emission factors by 2-4 times and (2) cookstove aerosol emissions were dominated by thermally stable OC, which is linked with stronger light absorption than volatile OC.

To constrain the MAC values for cookstove OC emissions, I performed optical (transmission and reflection) measurements on filter samples of aerosols collected during the field study. Filter optical measurements are associated with artifacts arising from the interaction of the filter medium with light. Through a laboratory study of a wide variety of combustion aerosols, I developed correction schemes for estimating aerosol-phase light absorption from filter-based measurements. This aided the estimation of absorption characteristics of cookstove particulate emissions and their OC components. We found that light absorbing OC contributes roughly as much as BC to total absorption cross-sections of cookstove emissions at 550 nm wavelength, enhancing their direct forcing efficiency. We proposed values for key absorption characteristics of cookstove OC emissions for use within climate impact assessment and mitigation efforts.

Chapter 1: Background and motivation

Atmospheric aerosols—liquid and/or solid particles suspended in air—originate from various natural and anthropogenic processes. They may be emitted directly to the atmosphere (primary) or formed from precursor gases through atmospheric reactions (secondary). The composition of atmospheric aerosols is source-dependent and varies across the globe and in time (Myhre et al., 2013). There are regional patterns in aerosol composition because of their short lifetime and seasonal patterns due to the facts that atmospheric conditions govern the evolution of their properties. Many physical processes that affect atmospheric aerosol are a function of particle size; broadly, aerosols are classified as coarse or fine mode.

The scientific interest in aerosols (Pöschl, 2005) and their complexity is in large part attributable to their range of climate (Stocker et al., 2013), health (Davidson et al., 2005) and visibility impacts. Aerosols affect the climate through several mechanisms–the direct effects involve a change in the atmospheric radiative budget from scattering and absorption by aerosols, while the indirect effects include their influence on cloud and ice formation and modification of the reflectance of snow and ice deposits (Pöschl, 2005; Bond et al., 2013; Stocker et al., 2013). Figure 1.1 shows a schematic of these direct and indirect mechanisms of aerosol climate effects and associate feedback loops that demonstrate the response of the climate system.

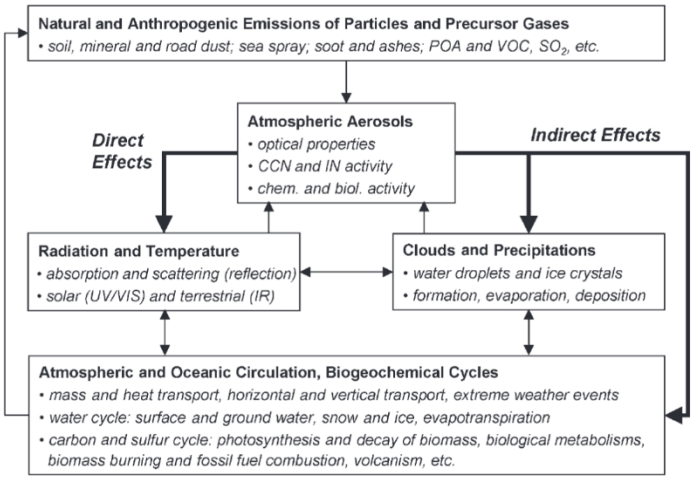

Figure 1.1: Direct and indirect aerosol climate effects and feedback loops. Source: Pöschl (2005).

The direct effects of aerosols are quantified as *radiative forcing* which is defined as the change in the net (downwelling – upwelling) solar and terrestrial energy flux (in Wm^{-2}) induced by a change in atmospheric composition relative to a baseline. In this definition, stratospheric temperatures are allowed to adjust to radiative equilibrium while surface and tropospheric temperatures are held fixed (implying that rapid adjustments in the troposphere are not included). Aerosol effects on clouds and snow, albeit involve more complicated physics, are also expressed as net changes in radiative flux or forcings. Aerosol radiative forcings for various aerosol types relative to a pre-industrial era (1750) are shown in Figure 1.2. These are in the context of all climate-relevant pollutants, such as greenhouse gases and short-lived gaseous forcers, included in the Intergovernmental Panel of Climate Change (IPCC) 2013 assessment of climate change (Stocker et al., 2013).

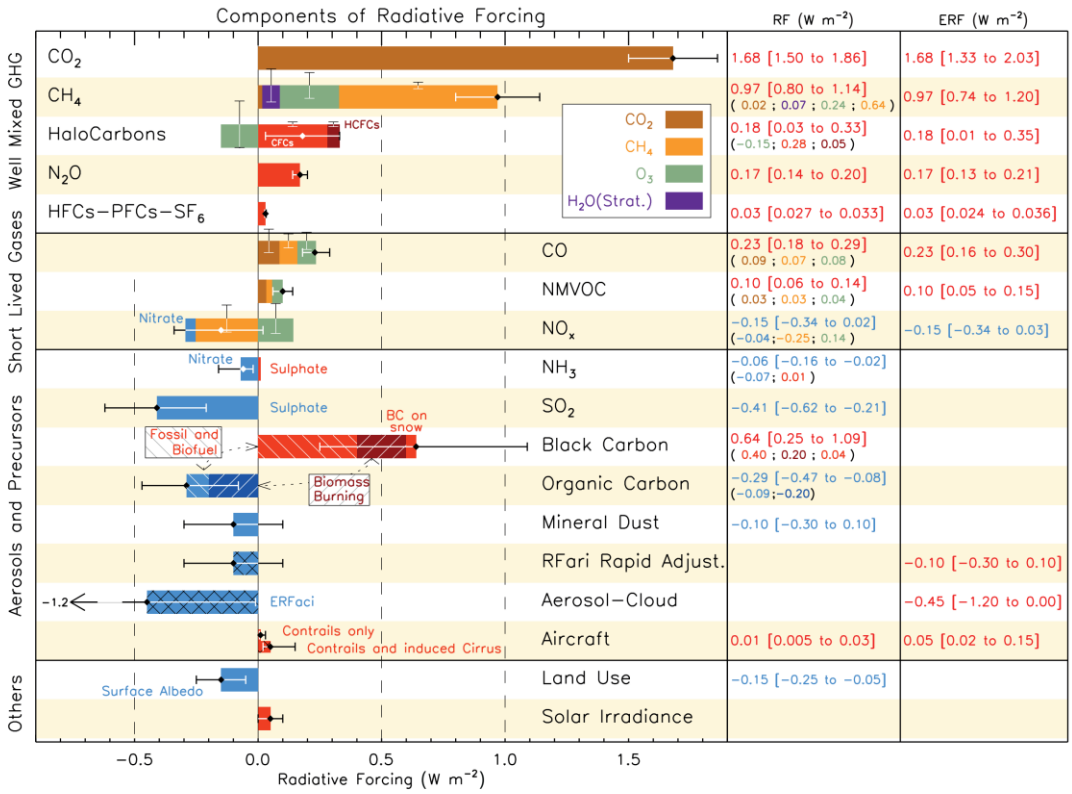

Figure 1.2: Radiative forcing relative to 1750, categorized by pollutant type. Source: Stocker et al. (2013).

Two of the emitted aerosol components in the figure above are particularly linked with the combustion of fossil and biomass fuels: organic carbon (OC) and black carbon (BC). These carbonaceous aerosol components, which are products of incomplete combustion of carbon fuels, are significant because of their ability to absorb solar radiation from ultraviolet to near-infrared wavelengths. My thesis focuses on contributing towards improving their representation in radiative models. Particularly, I will largely deal with mass emissions of BC and OC and their absorption and scattering efficiencies normalized to mass (mass absorption/scattering cross-sections: MAC/MSC in m^2g^{-1}). In Chapter 1.1, the state of knowledge regarding BC and OC optical and chemical characteristics is reviewed. This is followed by a discussion of measurement and modeling techniques for estimating the optical properties of aerosols (Chapter 1.2). Finally,

Chapter 1.3 examines aerosol emissions and their radiative effects over South Asia, to motivate the focus of my thesis research toward better characterizing an important aerosol emission source in that region.

1.1. Black and organic carbon (BC and OC) aerosols: optical and chemical properties

Black carbon is an optical definition of a form of carbonaceous aerosol—primarily emitted from flaming combustion—that strongly absorbs visible light. It is associated with the typical black appearance of smoke and is generally assumed to be equivalent to soot. Soot carbon is incepted in high-temperature flames as small spherules (monomers) from the condensation of large polyaromatic hydrocarbons; these monomers form aggregates whose morphologies and compositions are a function of flame properties (Sorensen et al., 1992). Most soot carbon is predominantly (85-95%) composed of elemental carbon (EC), is refractory and is insoluble in water and organic solvents. (Andreae and Gelencsér, 2006) BC and EC are widely considered synonymous to each other and to soot. In practice, they are both proxies for soot and both their measurements can be biased by the presence of other compounds as well as inherent analytical limitations (Andreae and Gelencsér, 2006; Bond and Bergstrom, 2006; Bond et al., 2013). With these caveats in mind, Bond and Bergstrom (2006) carefully reviewed BC MAC measurements in literature and constrained its value as 7.5 ± 1.2 m^2g^{-1} at 550 nm, with an inverse wavelength dependence. This dependence is parametrized by the absorption Ångström exponent or AAE ($MAC\sim\lambda^{-AAE}$); for BC aerosols AAE=1 throughout the visible spectrum. This wavelength dependence is consistent with the optical band-gap theory, a model for BC light absorption at the molecular level (Sun et al., 2007). In the atmosphere, BC might be internally-mixed (coated) with

non-absorbing inorganic/organic compounds which could enhance its MAC value by approximately 50% (Bond and Bergstrom, 2006; Cappa et al., 2012; Bond et al., 2013).

OC is an umbrella term for the carbon mass that is a part of aerosol phase organic compounds. Given the large chemical diversity in organic aerosols, OC physical and optical properties like refractoriness, polarity and crucially, absorption efficiency span a large inter-linked range (Figure 1.3). Generally, volatile, low molecular-weight organic compounds do not absorb light. While most climate models, and the IPCC climate assessment discussed above, treat all OC as purely light scattering, there is a large body of observations of weakly to moderately light-absorbing organic aerosols (Andreae and Gelencsér, 2006; Chakrabarty et al., 2010; Chen and Bond, 2010; Chakrabarty et al., 2013; Saleh et al., 2013; Saleh et al., 2014; Washenfelder et al., 2015; Saleh et al., 2018). These light absorbing aerosols are typically organic compounds with large molecular weights, with low volatility and high thermal stability (Sun et al., 2007; Saleh et al., 2018). Chemical speciation analyses have identified several such classes of compounds like nitroaromatic compounds, derivatives of polyaromatic hydrocarbons like quinones and charge transfer complexes of unsaturated organic compounds with transition metals (Phillips and Smith, 2014; Laskin et al., 2015; Lin et al., 2016; Bluvshtein et al., 2017).

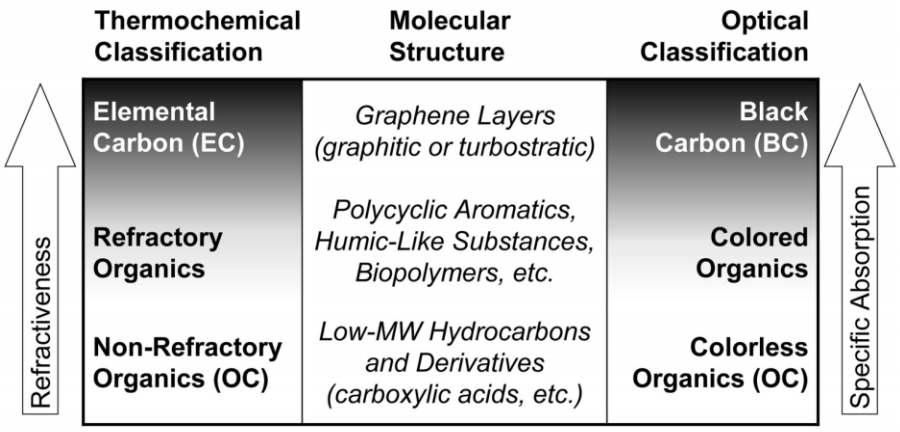

Figure 1.3: Continuum of carbonaceous aerosol properties. Source: Pöschl (2003).

The range of experimentally observed OC absorption characteristics—derived for primary OC emissions from a variety of biomass burning sources—span over an order of magnitude. In Figure 1.4, this variability is represented as the range of the imaginary parts (k) of OC refractive indices (which are determinants of MAC values) derived from observations of biomass combustion emissions. Cluster A in this figure shows k values for OC released from low-temperature (smoldering/pyrolysis) combustion of biomass (Chakrabarty et al., 2010; Chen and Bond, 2010; Saleh et al., 2013; Li et al., 2016) while cluster B shows those from flaming combustion (Kirchstetter et al., 2004; Saleh et al., 2013; Saleh et al., 2014), that produces BC along with OC. The difference between these clusters shows the dependence between OC absorption efficiency and combustion conditions, specifically the extent to which they favor BC formation (Saleh et al., 2014; Saleh et al., 2018; Cheng et al., 2019). In addition to observations linking combustion-related parameters to OC optical properties, these findings also necessitate the development of a source-linked database of OC MAC (or k) under realistic burn conditions. Despite the noted variability, a common feature of OC light absorption is a strong wavelength dependence with preferential absorption in near-UV wavelengths or AAE>2 (Andreae and Gelencsér, 2006; Sun et

al., 2007; Laskin et al., 2015). This gives rise to a yellowish-brown appearance (when sampled on a filter medium, shown in Figure 6.3), therefore, light absorbing OC is also termed brown carbon (BrC).

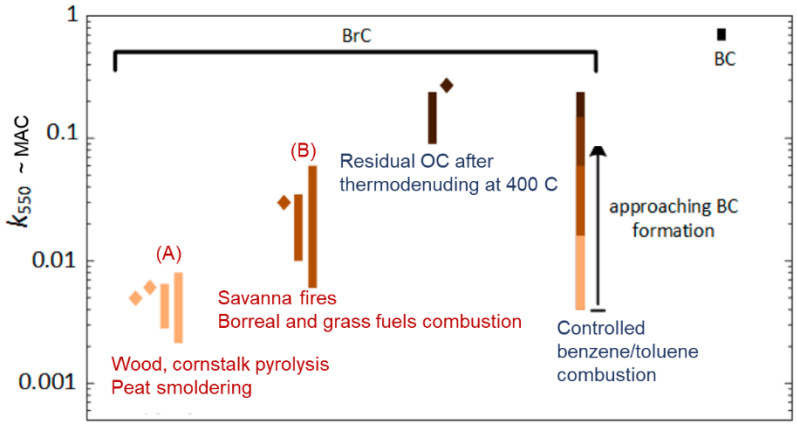

Figure 1.4: Imaginary part of OC refractive index, at 550 nm wavelength observed from biomass combustion and controlled benzene/toluene combustion. Adapted from Saleh et al. (2018).

1.2. Aerosol light absorption: measurement techniques and models

Aerosol light absorption measurement techniques (detailed review in Moosmüller et al. (2009)) can be broadly classified as *in-situ* (on particles in their native, suspended state) or filter-based (on deposits of particles on a filter substrate). A first-principle method of measuring *in-situ* aerosol light absorption is photoacoustic spectroscopy (PAS), which employs lasers at selected wavelengths to heat the aerosols, in turn heating the surrounding air and causing it to expand, thereby producing a detectable pressure (or acoustic) signal (Arnott et al., 1999). The photoacoustic principle is illustrated in Figure 1.5. The microphone signal can be calibrated against a reference material or a laser power extinction signal to provide an absorption coefficient (m^{-1}) value. Absorption can also be estimated as the difference between *in-situ* measurements of

extinction and scattering (Schnaiter et al., 2005; Sheridan et al., 2005). Properties of strongly light-absorbing, refractory materials like BC can be measured based on their incandescence under a high power laser beam; this forms the principle of the single particle soot photometer or the SP2 instrument (Stephens et al., 2003; Schwarz et al., 2006).

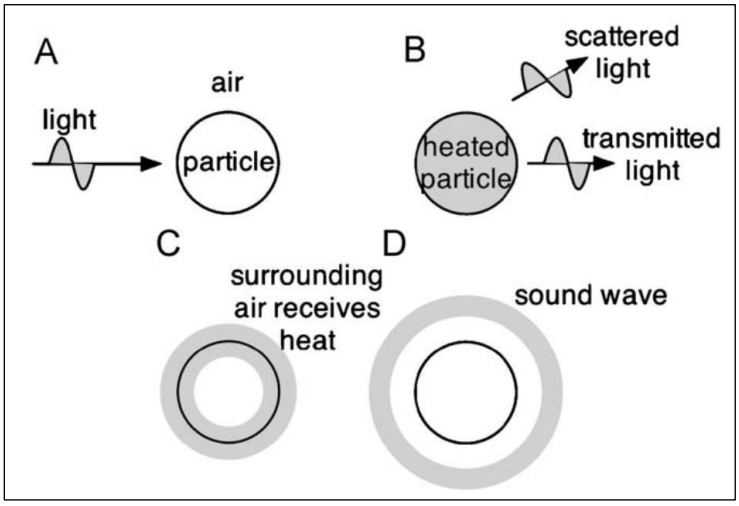

Figure 1.5: The photoacoustic effect showing that the (A) incident radiation absorbed by the particle (B) causes the particle to heat up, in turn (C) heating the surrounding air and generating a (D) pressure disturbance that is detected as a sound wave. Source: Moosmüller et al. (2009).

Alternatively, a commonly adopted technique for estimating light absorption uses measurements of transmittance and/or reflectance for aerosol particles collected on a filter substrate. Instruments based on this technique, including the aethalometer (Hansen et al., 1984) and the Particle Soot Absorption Photometer or PSAP (Virkkula et al., 2005), facilitate semi-continuous sampling of particles and produce time-averaged bulk absorption measurements. Particles may also be collected on a filter substrate and analyzed for their absorption using standalone spectrophotometers (Martins et al., 2009; Zhong and Jang, 2011; Pandey et al., 2016; White et al., 2016). The change in filter transmittance or reflectance due to the deposited particles is a measure of their light absorption. If this change could indeed be entirely attributed to aerosol light

absorption, attenuation of light through the filter medium would be exactly equal to the absorption optical depth of the aerosol deposits.

Filter-based measurements are attractive because of their ease of deployment in field settings and low cost, but they suffer from several artifacts. Particles embedded in a multiple-scattering medium experience a larger optical path length than in their native suspended state, leading to the appearance of enhanced light absorption (Clarke, 1982; Bond et al., 1999; Gorbunov et al., 2002). This is referred to the as the multiple scattering artifact and depends on the choice of filter medium. A higher loading of absorbing aerosols can diminish the effect of multiple scattering, inducing an aerosol dependent loading artifact (Weingartner et al., 2003; Arnott et al., 2005). Highly scattering aerosols could enhance multiple scattering and lead to increased backscatter, which leads to an overestimation of absorption (Weingartner et al., 2003; Lack et al., 2008). These artifacts have been evaluated for several commonly used filter-based instruments, such as those aforementioned, by comparing their measurements with contact-free aerosol light absorption measurements or using reference materials with known optical properties. Typically, correction algorithms (detailed in Chapter 5.1) for these artifacts are formulated as functions of some combination of filter and aerosol properties (Weingartner et al., 2003; Arnott et al., 2005; Collaud Coen et al., 2010; Virkkula, 2010) and are specific to a given measurement system.

For homogenous, spherical particles, Maxwell's equations for scattering and absorption of electromagnetic radiation have been analytically solved, in terms of the vector spherical harmonics of the incident plane wave (Mie, 1908; Bohren and Huffman, 2008). These solutions, known as the Lorenz-Mie theory, enable calculation of absorption and scattering cross-sections as functions of particle size, refractive index and wavelength of incident radiation. The availability of efficient Mie computational codes (Mishchenko and Travis, 2008) and the widespread characterization of

aerosol size in terms of equivalent diameters (based on, for example, electrical mobility and aerodynamic behavior) make them easy to implement in radiative transfer codes (Bond et al., 2013). Therefore, assumptions of spherical morphology are commonly made for BC particles. Homogenous particles of irregular shapes can be treated by the transition matrix (*T*-matrix) method (Mishchenko et al., 2004) in which the relationship between incident and scattered fields is described by a 2x2 matrix whose elements are computed by numerical integration over the surface of a particle. The discrete dipole approximation (DDA) involves modeling a particle as a collection of dipoles that interact with the incident radiation and with each other, making it suitable for even inhomogeneous particle with irregular morphologies (Purcell and Pennypacker, 1973). One approach to improving the parameterization of BC in climate models is to connect accurate modeling of BC in optical calculations with the requirements of the broader aerosol experimental and modeling research.

1.3. Aerosol emissions in South Asia

Aerosol burden over much of the Indian subcontinent is five times higher than that over developed countries like the United States, largely because of larger emissions of primary particles and aerosol-precursors (David et al., 2018). The Indian subcontinent has been termed a spot for anthropogenic emissions (Ramanathan and Carmichael, 2008). Carbonaceous aerosol burden over India is linked to surface dimming (Kambezidis et al., 2012), solar warming of the lower atmosphere (Ramanathan et al., 2001; 2007), changing regional monsoon patterns (Menon et al., 2002; Chung and Seinfeld, 2005; Ramanathan et al., 2005), and accelerated melting of Himalayan glaciers (Ramanathan et al., 2007). Particulate matter (PM) emissions—particularly particles with aerodynamic diameters less than 2.5 μm ($PM_{2.5}$)—are also associated with numerous adverse consequences for human health (Pope and Dockery, 2006; Pope et al., 2009). The Global Burden

of Disease study has identified indoor air pollution as the largest risk factor and outdoor air pollution as the seventh largest risk factor for disability-adjusted life years in India (Murray et al., 2013) . The knowledge of aerosol emissions characteristics like mass emission rates and optical properties for regionally significant sources is crucial for assessing source-specific aerosol radiative (and health) impacts.

The most recent emissions inventory for India indicated that residential biomass cookstoves are the largest contributors to total annual $PM_{2.5}$, EC and OC emissions (Pandey et al., 2014; Sadavarte and Venkataraman, 2014). In 2010, 67% of Indian households, more than 160 million total, relied primarily on solid fuels for cooking (Census, 2011). The solid fuels included fuel-wood, agricultural residues (like straws and stalks) and dried cattle dung. The above fraction does not capture household in a 'transition income band' that use biomass as a secondary fuel (in addition to LPG/kerosene) as a cost-saving measure (Venkataraman et al., 2010). Therefore, the emissions impact of biomass cookstoves is likely larger than current estimates.

Despite several national initiatives to promote the use of improved biomass stoves (Venkataraman et al., 2010), traditional mud stoves (or *chulha*) and three-stone type brick and metal stoves are commonly used (Kar et al., 2012). Operational challenges and the lack of adequate repair and maintenance services contributed to low user adoption rates of the stoves disseminated under the National Program on Improved Cookstoves (Kishore and Ramana, 2002). Moreover, the in-field emissions performance of the improved cooking devices was found to be similar to that of the traditional stoves (Ramakrishna et al., 1989). Stove performance is characterized by two efficiencies: (1) the combustion efficiency captures how much of the energy content of the fuel is converted to heat and carbon dioxide, and (2) the heat transfer efficiency relates to how much of the heat generated is absorbed by the pot. A third measure, the overall thermal efficiency, is the

fraction of the fuel energy absorbed by the pot: it can be obtained as the product of the first two efficiencies. Traditional cookstoves have low combustion efficiencies, resulting in incomplete combustion and high PM emissions (Smith et al., 2000). The early generation of improved cookstoves distributed in India provided fuel savings by increasing the heat transfer efficiency, through improved insulation of the combustion chamber, but largely failed to deliver emissions reductions. Although a new program, the National Cookstove Initiative was announced to develop and disseminate low-emissions cookstoves (Venkataraman et al., 2010), biomass cooking technology in India can still considered to be predominantly inefficient (Pandey et al., 2014).

Evaluating the contribution of biomass cookstoves to regional pollutant burdens requires the knowledge of their emissions performance, expressed as mass emission factors (g-pollutant kg^{-1}-fuel). Most of the emission factors used in inventory calculations were from laboratory cookstove tests (Bond et al., 2013; Pandey et al., 2014). These studies largely rely on a water-boiling test (WBT) with high and low power phases for simultaneous measurement of thermal and emissions performance, even if not all cooking actually involves the boiling of water in this manner (Johnson et al., 2009; Chen et al., 2012). There is study-to-study variation in test conditions such as amounts of water boiled, the length and definition of low and high power phases, the moisture content of the fuel, the use of a lid on the pot, the method of measuring emissions and other parameters, yet represent currently best available numbers. Field-based measurements, made during actual cooking processes, indicate significantly worse emissions performance of traditional stoves, than what was previously established through lab testing because of differences in burn rate and firing practice between laboratory and field settings, even for similar fuel characteristics (Roden et al., 2009; Chen et al., 2012; Jayarathne et al., 2018; Weyant et al., 2019). More evaluations of in-use

emissions performance of traditional cookstoves using common South Asian biomass fuels are needed, in addition to inputs for designing realistic laboratory burn cycles.

Discussions of the climate impacts of aerosol emissions from residential biomass use (Venkataraman et al., 2005; Grieshop et al., 2011) largely include only BC as a light absorbing component. Experimental observations (Kirchstetter et al., 2004; Andreae and Gelencsér, 2006; Kirchstetter and Thatcher, 2012; Saleh et al., 2014; Saleh et al., 2018) and recent modeling studies (Chung et al., 2012; Feng et al., 2013; Wang et al., 2014) indicate the potential significance of light absorbing OC to radiative forcing estimation. Accounting for light absorbing OC in radiative models may be a step towards resolving the factor of ~6 underestimation (Bond et al., 2013; Gustafsson and Ramanathan, 2016) of aerosol absorption optical depth over South Asia by climate models, in comparison with ground-based observation of the same. Estimating representative OC MAC values for cookstove emissions, to serve as inputs to climate models, is crucial for addressing the model bias.

References

Andreae, M. and Gelencsér, A.: Black carbon or brown carbon? The nature of light-absorbing carbonaceous aerosols, Atmos. Chem. Phys., 6, 3131-3148, 2006.

Arnott, W. P., Hamasha, K., Moosmüller, H., Sheridan, P. J., and Ogren, J. A.: Towards aerosol light-absorption measurements with a 7-wavelength aethalometer: Evaluation with a photoacoustic instrument and 3-wavelength nephelometer, Aerosol Sci. Technol., 39, 17-29, 2005.

Arnott, W. P., Moosmüller, H., Rogers, C. F., Jin, T., and Bruch, R.: Photoacoustic spectrometer for measuring light absorption by aerosol: instrument description, Atmos. Environ., 33, 2845-2852, 1999.

Bluvshtein, N., Lin, P., Flores, J. M., Segev, L., Mazar, Y., Tas, E., Snider, G., Weagle, C., Brown, S. S., and Laskin, A.: Broadband optical properties of biomass-burning aerosol and identification of brown carbon chromophores, J. Geophys. Res.: Atmos., 122, 5441-5456, 2017.

Bohren, C. F. and Huffman, D. R.: Absorption and scattering of light by small particles, John Wiley & Sons, 2008.

Bond, T. C., Anderson, T. L., and Campbell, D.: Calibration and intercomparison of filter-based measurements of visible light absorption by aerosols, Aerosol Sci. Technol., 30, 582-600, 1999.

Bond, T. C. and Bergstrom, R. W.: Light absorption by carbonaceous particles: An investigative review, Aerosol Sci. Technol., 40, 27-67, 2006.

Bond, T. C., Doherty, S. J., Fahey, D., Forster, P., Berntsen, T., DeAngelo, B., Flanner, M., Ghan, S., Kärcher, B., and Koch, D.: Bounding the role of black carbon in the climate system: A scientific assessment, J. Geophys. Res.: Atmos., 118, 5380-5552, 2013.

Cappa, C. D., Onasch, T. B., Massoli, P., Worsnop, D. R., Bates, T. S., Cross, E. S., Davidovits, P., Hakala, J., Hayden, K. L., and Jobson, B. T.: Radiative absorption enhancements due to the mixing state of atmospheric black carbon, Science, 337, 1078-1081, 2012.

Census: Houselisting and Housing Census Data Office of The Registrar General and Census Commissioner, M. o. H. A., Goverment of India. (Ed.), New Delhi., 2011.

Chakrabarty, R., Moosmüller, H., Chen, L.-W., Lewis, K., Arnott, W., Mazzoleni, C., Dubey, M., Wold, C., Hao, W., and Kreidenweis, S.: Brown carbon in tar balls from smoldering biomass combustion, Atmos. Chem. Phys., 10, 6363-6370, 2010.

Chakrabarty, R., Pervez, S., Chow, J. C., Watson, J. G., Dewangan, S., Robles, J., and Tian, G.: Funeral pyres in South Asia: Brown carbon aerosol emissions and climate impacts, Environ. Sci. Technol. Lett., 1, 44-48, 2013.

Chen, Y. and Bond, T.: Light absorption by organic carbon from wood combustion, Atmos. Chem. Phys., 10, 1773-1787, 2010.

Chen, Y., Roden, C. A., and Bond, T. C.: Characterizing biofuel combustion with patterns of real-time emission data (PaRTED), Environ. Sci. Technol., 46, 6110-6117, 2012.

Cheng, Z., Atwi, K., Onyima, T., and Saleh, R.: Investigating the dependence of light-absorption properties of combustion carbonaceous aerosols on combustion conditions, Aerosol Sci. Technol., 53, 419-434, 2019.

Chung, C. E., Ramanathan, V., and Decremer, D.: Observationally constrained estimates of carbonaceous aerosol radiative forcing, Proceedings of the National Academy of Sciences, 109, 11624-11629, 2012.

Chung, S. H. and Seinfeld, J. H.: Climate response of direct radiative forcing of anthropogenic black carbon, J. Geophys. Res.: Atmos., 110, 2005.
Clarke, A. D.: Effects of filter internal reflection coefficient on light absorption measurements made using the integrating plate method, Appl. Opt., 21, 3021-3031, 1982.
Collaud Coen, M., Weingartner, E., Apituley, A., Ceburnis, D., Fierz-Schmidhauser, R., Flentje, H., Henzing, J., Jennings, S. G., Moerman, M., and Petzold, A.: Minimizing light absorption measurement artifacts of the Aethalometer: evaluation of five correction algorithms, Atmos. Meas. Tech., 3, 457-474, 2010.
David, L. M., Ravishankara, A., Kodros, J. K., Venkataraman, C., Sadavarte, P., Pierce, J. R., Chaliyakunnel, S., and Millet, D. B.: Aerosol optical depth over India, J. Geophys. Res.: Atmos., 123, 3688-3703, 2018.
Davidson, C. I., Phalen, R. F., and Solomon, P. A.: Airborne particulate matter and human health: a review, Aerosol Sci. Technol., 39, 737-749, 2005.
Feng, Y., Ramanathan, V., and Kotamarthi, V.: Brown carbon: a significant atmospheric absorber of solar radiation?, Atmos. Chem. Phys., 13, 8607-8621, 2013.
Gorbunov, B., Hamilton, R., and Hitzenberger, R.: Modeling radiative transfer by aerosol particles on a filter, Aerosol Sci. Technol., 36, 123-135, 2002.
Grieshop, A. P., Marshall, J. D., and Kandlikar, M.: Health and climate benefits of cookstove replacement options, Energy Policy, 39, 7530-7542, 2011.
Gustafsson, Ö. and Ramanathan, V.: Convergence on climate warming by black carbon aerosols, Proceedings of the National Academy of Sciences, 113, 4243-4245, 2016.
Hansen, A., Rosen, H., and Novakov, T.: The aethalometer—an instrument for the real-time measurement of optical absorption by aerosol particles, Sci. Total Environ., 36, 191-196, 1984.
Jayarathne, T., Stockwell, C. E., Bhave, P. V., Praveen, P. S., Rathnayake, C. M., Islam, M., Panday, A. K., Adhikari, S., Maharjan, R., and Goetz, J. D.: Nepal Ambient Monitoring and Source Testing Experiment (NAMaSTE): emissions of particulate matter from wood-and dung-fueled cooking fires, garbage and crop residue burning, brick kilns, and other sources, Atmos. Chem. Phys., 18, 2259-2286, 2018.
Johnson, M., Edwards, R., Berrueta, V., and Masera, O.: New approaches to performance testing of improved cookstoves, Environ. Sci. Technol., 44, 368-374, 2009.
Kambezidis, H., Kaskaoutis, D., Kharol, S. K., Moorthy, K. K., Satheesh, S., Kalapureddy, M., Badarinath, K., Sharma, A. R., and Wild, M.: Multi-decadal variation of the net downward shortwave radiation over south Asia: The solar dimming effect, Atmos. Environ., 50, 360-372, 2012.
Kar, A., Rehman, I. H., Burney, J., Puppala, S. P., Suresh, R., Singh, L., Singh, V. K., Ahmed, T., Ramanathan, N., and Ramanathan, V.: Real-time assessment of black carbon pollution in Indian households due to traditional and improved biomass cookstoves, Environ. Sci. Technol., 46, 2993-3000, 2012.
Kirchstetter, T. W., Novakov, T., and Hobbs, P. V.: Evidence that the spectral dependence of light absorption by aerosols is affected by organic carbon, J. Geophys. Res.: Atmos., 109, 2004.
Kirchstetter, T. W. and Thatcher, T.: Contribution of organic carbon to wood smoke particulate matter absorption of solar radiation, Atmos. Chem. Phys., 12, 6067-6072, 2012.
Kishore, V. and Ramana, P.: Improved cookstoves in rural India: how improved are they?: A critique of the perceived benefits from the National Programme on Improved Chulhas (NPIC), Energy, 27, 47-63, 2002.

Lack, D. A., Cappa, C. D., Covert, D. S., Baynard, T., Massoli, P., Sierau, B., Bates, T. S., Quinn, P. K., Lovejoy, E. R., and Ravishankara, A.: Bias in filter-based aerosol light absorption measurements due to organic aerosol loading: Evidence from ambient measurements, Aerosol Sci. Technol., 42, 1033-1041, 2008.

Laskin, A., Laskin, J., and Nizkorodov, S. A.: Chemistry of Atmospheric Brown Carbon, Chem. Rev., 115, 4335-4382, 2015.

Li, X., Chen, Y., and Bond, T. C.: Light absorption of organic aerosol from pyrolysis of corn stalk, Atmos. Environ., 144, 249-256, 2016.

Lin, P., Aiona, P. K., Li, Y., Shiraiwa, M., Laskin, J., Nizkorodov, S. A., and Laskin, A.: Molecular characterization of brown carbon in biomass burning aerosol particles, Environ. Sci. Technol., 50, 11815-11824, 2016.

Martins, J. V., Artaxo, P., Kaufman, Y. J., Castanho, A. D., and Remer, L. A.: Spectral absorption properties of aerosol particles from 350–2500nm, Geophys. Res. Lett., 36, 2009.

Menon, S., Hansen, J., Nazarenko, L., and Luo, Y.: Climate effects of black carbon aerosols in China and India, Science, 297, 2250-2253, 2002.

Mie, G.: Beiträge zur Optik trüber Medien, speziell kolloidaler Metallösungen, Annalen der physik, 330, 377-445, 1908.

Mishchenko, M. I. and Travis, L. D.: Gustav Mie and the evolving discipline of electromagnetic scattering by particles, Bulletin of the American Meteorological Society, 89, 1853-1862, 2008.

Mishchenko, M. I., Videen, G., Babenko, V. A., Khlebtsov, N. G., and Wriedt, T.: T-matrix theory of electromagnetic scattering by particles and its applications: a comprehensive reference database, J. Quant. Spectrosc. Radiat. Transfer, 88, 357-406, 2004.

Moosmüller, H., Chakrabarty, R., and Arnott, W.: Aerosol light absorption and its measurement: A review, J. Quant. Spectrosc. Radiat. Transfer, 110, 844-878, 2009.

Murray, C. J., Vos, T., Lozano, R., Naghavi, M., Flaxman, A. D., Michaud, C., Ezzati, M., Shibuya, K., Salomon, J. A., and Abdalla, S.: Disability-adjusted life years (DALYs) for 291 diseases and injuries in 21 regions, 1990–2010: a systematic analysis for the Global Burden of Disease Study 2010, The lancet, 380, 2197-2223, 2013.

Myhre, G., Myhre, C. L., Samset, B., and Storelvmo, T.: Aerosols and their relation to global climate and climate sensitivity, Nature Education Knowledge, 4, 7, 2013.

Pandey, A., Pervez, S., and Chakrabarty, R. K.: Filter-based measurements of UV–vis mass absorption cross sections of organic carbon aerosol from residential biomass combustion: Preliminary findings and sources of uncertainty, J. Quant. Spectrosc. Radiat. Transfer, 182, 296-304, 2016.

Pandey, A., Sadavarte, P., Rao, A. B., and Venkataraman, C.: Trends in multi-pollutant emissions from a technology-linked inventory for India: II. Residential, agricultural and informal industry sectors, Atmos. Environ., 99, 341-352, 2014.

Phillips, S. M. and Smith, G. D.: Light absorption by charge transfer complexes in brown carbon aerosols, Environ. Sci. Technol. Lett., 1, 382-386, 2014.

Pope, C. A., Burnett, R. T., Krewski, D., Jerrett, M., Shi, Y., Calle, E. E., and Thun, M. J.: Cardiovascular mortality and exposure to airborne fine particulate matter and cigarette smoke, Circulation, 120, 941-948, 2009.

Pope, C. A. and Dockery, D. W.: Health effects of fine particulate air pollution: lines that connect, Journal of the air & waste management association, 56, 709-742, 2006.

Pöschl, U.: Aerosol particle analysis: challenges and progress, Analytical and bioanalytical chemistry, 375, 30-32, 2003.

Pöschl, U.: Atmospheric aerosols: composition, transformation, climate and health effects, Angew. Chem. Int. Ed., 44, 7520-7540, 2005.
Purcell, E. M. and Pennypacker, C. R.: Scattering and absorption of light by nonspherical dielectric grains, The Astrophysical Journal, 186, 705-714, 1973.
Ramakrishna, J., Durgaprasad, M., and Smith, K. R.: Cooking in India: the impact of improved stoves on indoor air quality, Environment International, 15, 341-352, 1989.
Ramanathan, V. and Carmichael, G.: Global and regional climate changes due to black carbon, Nature geoscience, 1, 221-227, 2008.
Ramanathan, V., Chung, C., Kim, D., Bettge, T., Buja, L., Kiehl, J., Washington, W., Fu, Q., Sikka, D., and Wild, M.: Atmospheric brown clouds: Impacts on South Asian climate and hydrological cycle, Proc. Natl. Acad. Sci. U.S.A., 102, 5326-5333, 2005.
Ramanathan, V., Crutzen, P., Kiehl, J., and Rosenfeld, D.: Aerosols, climate, and the hydrological cycle, Science, 294, 2119-2124, 2001.
Ramanathan, V., Ramana, M. V., Roberts, G., Kim, D., Corrigan, C., Chung, C., and Winker, D.: Warming trends in Asia amplified by brown cloud solar absorption, Nature, 448, 575-578, 2007.
Roden, C. A., Bond, T. C., Conway, S., Pinel, A. B. O., MacCarty, N., and Still, D.: Laboratory and field investigations of particulate and carbon monoxide emissions from traditional and improved cookstoves, Atmos. Environ., 43, 1170-1181, 2009.
Sadavarte, P. and Venkataraman, C.: Trends in multi-pollutant emissions from a technology-linked inventory for India: I. Industry and transport sectors, Atmos. Environ., 99, 353-364, 2014.
Saleh, R., Cheng, Z., and Atwi, K.: The brown–black continuum of light-absorbing combustion aerosols, Environ. Sci. Technol. Lett., 5, 508-513, 2018.
Saleh, R., Hennigan, C., McMeeking, G., Chuang, W., Robinson, E., Coe, H., Donahue, N., and Robinson, A.: Absorptivity of brown carbon in fresh and photo-chemically aged biomass-burning emissions, Atmos. Chem. Phys., 13, 7683-7693, 2013.
Saleh, R., Robinson, E. S., Tkacik, D. S., Ahern, A. T., Liu, S., Aiken, A. C., Sullivan, R. C., Presto, A. A., Dubey, M. K., and Yokelson, R. J.: Brownness of organics in aerosols from biomass burning linked to their black carbon content, Nature geoscience, 7, 647-650, 2014.
Schnaiter, M., Schmid, O., Petzold, A., Fritzsche, L., Klein, K.-F., Andreae, M. O., Helas, G., Thielmann, A., Gimmler, M., and Möhler, O.: Measurement of wavelength-resolved light absorption by aerosols utilizing a UV-VIS extinction cell, Aerosol Sci. Technol., 39, 249-260, 2005.
Schwarz, J., Gao, R., Fahey, D., Thomson, D., Watts, L., Wilson, J., Reeves, J., Darbeheshti, M., Baumgardner, D., and Kok, G.: Single-particle measurements of midlatitude black carbon and light-scattering aerosols from the boundary layer to the lower stratosphere, J. Geophys. Res.: Atmos., 111, 2006.
Sheridan, P. J., Arnott, W. P., Ogren, J. A., Andrews, E., Atkinson, D. B., Covert, D. S., Moosmüller, H., Petzold, A., Schmid, B., and Strawa, A. W.: The Reno Aerosol Optics Study: An evaluation of aerosol absorption measurement methods, Aerosol Sci. Technol., 39, 1-16, 2005.
Smith, K. R., Uma, R., Kishore, V. V. N., Lata, K., Joshi, V., Zhang, J., Rasmussen, R. A., and Khalil, M. A. K.: Greenhouse gases from small-scale combustion devices in developing countries: Phase IIA, Household stoves in India, US EPA, Washington DC, 89 pp., 2000.

Sorensen, C., Cai, J., and Lu, N.: Light-scattering measurements of monomer size, monomers per aggregate, and fractal dimension for soot aggregates in flames, Appl. Opt., 31, 6547-6557, 1992.

Stephens, M., Turner, N., and Sandberg, J.: Particle identification by laser-induced incandescence in a solid-state laser cavity, Appl. Opt., 42, 3726-3736, 2003.

Stocker, T. F., Qin, D., Plattner, G.-K., Tignor, M., Allen, S. K., Boschung, J., Nauels, A., Xia, Y., Bex, V., and Midgley, P. M.: Climate change 2013: The physical science basis. Cambridge University Press Cambridge, 2013.

Sun, H., Biedermann, L., and Bond, T. C.: Color of brown carbon: A model for ultraviolet and visible light absorption by organic carbon aerosol, Geophys. Res. Lett., 34, 2007.

Venkataraman, C., Habib, G., Eiguren-Fernandez, A., Miguel, A., and Friedlander, S.: Residential biofuels in South Asia: carbonaceous aerosol emissions and climate impacts, Science, 307, 1454-1456, 2005.

Venkataraman, C., Sagar, A., Habib, G., Lam, N., and Smith, K.: The Indian national initiative for advanced biomass cookstoves: the benefits of clean combustion, Energy for Sustainable Development, 14, 63-72, 2010.

Virkkula, A.: Correction of the calibration of the 3-wavelength Particle Soot Absorption Photometer (3λ PSAP), Aerosol Sci. Technol., 44, 706-712, 2010.

Virkkula, A., Ahlquist, N. C., Covert, D. S., Arnott, W. P., Sheridan, P. J., Quinn, P. K., and Coffman, D. J.: Modification, calibration and a field test of an instrument for measuring light absorption by particles, Aerosol Sci. Technol., 39, 68-83, 2005.

Wang, X., Heald, C., Ridley, D., Schwarz, J., Spackman, J., Perring, A., Coe, H., Liu, D., and Clarke, A.: Exploiting simultaneous observational constraints on mass and absorption to estimate the global direct radiative forcing of black carbon and brown carbon, Atmos. Chem. Phys., 14, 10989-11010, 2014.

Washenfelder, R., Attwood, A., Brock, C., Guo, H., Xu, L., Weber, R., Ng, N., Allen, H., Ayres, B., and Baumann, K.: Biomass burning dominates brown carbon absorption in the rural southeastern United States, Geophys. Res. Lett., 42, 653-664, 2015.

Weingartner, E., Saathoff, H., Schnaiter, M., Streit, N., Bitnar, B., and Baltensperger, U.: Absorption of light by soot particles: determination of the absorption coefficient by means of aethalometers, J. Aerosol Sci, 34, 1445-1463, 2003.

Weyant, C. L., Chen, P., Vaidya, A., Li, C., Zhang, Q., Thompson, R., Ellis, J., Chen, Y., Kang, S., and Shrestha, G. R.: Emission measurements from traditional biomass cookstoves in South Asia and Tibet, Environ. Sci. Technol., 2019. 2019.

White, W. H., Trzepla, K., Hyslop, N. P., and Schichtel, B. A.: A critical review of filter transmittance measurements for aerosol light absorption, and de novo calibration for a decade of monitoring on PTFE membranes, Aerosol Sci. Technol., 50, 984-1002, 2016.

Zhong, M. and Jang, M.: Light absorption coefficient measurement of SOA using a UV–Visible spectrometer connected with an integrating sphere, Atmos. Environ., 45, 4263-4271, 2011.

Chapter 2: Research objectives

My first research objective was to aid **accurate morphological representation of black carbon in optical parameterizations**, bridging the gap between optical models that explicitly handle the fractal morphology of BC aggregates and radiative transfer models that assume spherical morphology for all aerosols. Optical models that account for BC morphology are (1) able to predict BC MAC values very close to the average of those experimentally observed and (2) demonstrate that an equivalent sphere of the same mass or a group of non-interacting individual spherules show very large deviations from these ideal predictions (Liu and Mishchenko, 2007; Liu et al., 2008; Sorensen et al., 2018). However, radiative modules within global climate models do not include computationally-expensive, detailed morphological representations and may opt to scale optical calculations to match observations (Bond et al., 2013). Further, observations of BC size distribution are based on common aerosol sizing instruments; descriptors of fractal size and shape can only be measured using more sophisticated techniques, like small-angle light scattering (Heinson et al., 2016). To surmount these obstacles, I developed empirical relationships between BC optical cross-sections and widely used equivalent diameters. These results, discussed in Chapter 3.1, have been reported in Pandey et al. (2015). A second goal was to test the validity of the prevalent relationships between scattering directionality parameters of BC (Moosmüller and Ogren, 2017). These relationships are based on an analytical approximation of the angular distribution of radiations scattered by (any type of) particles: the Henyey-Greenstein phase function (Henyey and Greenstein, 1941). In Pandey and Chakrabarty (2016), I examined the errors

associated with using the above relationships for estimating scattering directionality of BC aggregates (Chapter 3.2).

Given the magnitude of particulate pollution in India and the bias in the modeled values of aerosol light absorption in this region (modeled values are much smaller than observations), it is crucial to assess which model inputs can be improved. I focused on the largest source of primary particle emissions in India: residential biomass cookstoves. My second research objective was to estimate **aerosol emission factors from field study of cookstove emissions in India**. Mass-based emission factors are critical inputs to inventory models which are then used to calculate pollutant burdens. A small number of field observations showed that laboratory cookstove studies (which formed the bulk of the observations included in inventory models) significantly underestimate particle emission rates. In Chapter 4, I report $PM_{2.5}$, EC and OC emission factors from a field study of common biomass fuels in India (Pandey et al., 2017). One goal was to determine the emissions performance of a traditional stove, using fuels locally scavenged from regions that have large biomass user populations, during real-world operation that involved preparing common meal items. Another was to examine the relationship between emission factors and (1) fuel-type and (2) the stage of combustion (ignition or fueling, flaming, smoldering). This can inform future studies by identifying factors that control emissions behavior: for example, whether it is necessary to speciate emissions by (and therefore perform measurements on) a large variety of fuel types.

To utilize the filter samples of cookstove emissions from the aforementioned field study for estimating the absorption characteristics of these emissions, I used filter-based ultraviolet-visible (UV-vis) spectroscopy. The artifacts involved in estimating aerosol phase light absorption from filter optical measurements are instrument specific: published correction schemes apply only to a limited number of instruments. Much of the artifact correction literature deals with the scattering

effects of inorganic aerosols (Bond et al., 1999; Weingartner et al., 2003; Arnott et al., 2005; Virkkula, 2010) and the validity of these schemes has not been tested for liquid-like organics (Subramanian et al., 2007) that spread on filter fibers. Finally, these correction methods require an independent measurement of aerosol light scattering concurrent with filter sampling. Therefore, my third objective involved **estimating aerosol-phase light absorption from filter-based optics** using a correction scheme applicable to biomass burning aerosols, potentially without the need for scattering observations (Chapter 5). The requisite experimental plan involved generating combustion aerosols with a wide range of intrinsic properties (therefore, representative of various types of biomass burning) and allowing for comparison between *in-situ* (PAS based) and filter optical properties. A radiative transfer model of the filter-particle system supplemented experimental findings and a measurement method capable of meeting the above requirements was identified (Pandey et al., 2019).

Few studies report MAC values of cookstove particulate emissions, fewer still attribute the total absorption to BC and OC. This poses a challenge in expanding the conventional discussion of aerosol climate impacts where OC light absorption is neglected. In Chapter 6, I describe my final objective: **constraining the contribution of organic carbon to light absorption by cookstove emissions.** First, I discuss initial estimates of OC absorption properties based on a preliminary round of sampling (prior to the more comprehensive field study) cookstove emissions in India, in the context of the challenges inherent to this analysis (Pandey et al., 2016). The methods used then were later updated to reflect the improvements in filter artifact correction and applied to the field study samples. Assumptions on the spectral behavior of BC (its AAE value) also required updating, based on observations and models of coated BC aggregates (Gyawali et al., 2013; Liu et al., 2018). With a range of probable values of AAE_{BC}, MAC and AAE for cookstove emitted OC

were constrained. Another goal of this research was to examine the contribution of OC to direct radiative forcing associated with cookstove emissions. Though the estimation of the magnitude forcing efficiency requires scattering cross-sections—not measured in my work—in addition to absorption, the portion of forcing efficiency attributable of OC light absorption can be well-constrained independent of any assumptions regarding scattering. These calculations indicate that OC light absorption could likely tip the net direct radiative impact of cookstove emissions from cooling to warming.

References

Arnott, W. P., Hamasha, K., Moosmüller, H., Sheridan, P. J., and Ogren, J. A.: Towards aerosol light-absorption measurements with a 7-wavelength aethalometer: Evaluation with a photoacoustic instrument and 3-wavelength nephelometer, Aerosol Sci. Technol., 39, 17-29, 2005.
Bond, T. C., Anderson, T. L., and Campbell, D.: Calibration and intercomparison of filter-based measurements of visible light absorption by aerosols, Aerosol Sci. Technol., 30, 582-600, 1999.
Bond, T. C., Doherty, S. J., Fahey, D., Forster, P., Berntsen, T., DeAngelo, B., Flanner, M., Ghan, S., Kärcher, B., and Koch, D.: Bounding the role of black carbon in the climate system: A scientific assessment, J. Geophys. Res.: Atmos., 118, 5380-5552, 2013.
Gyawali, M., Arnott, W. P., Zaveri, R. A., Song, C., Pekour, M., Flowers, B., Dubey, M. K., Setyan, A., Zhang, Q., and Harworth, J.: Evolution of multispectral aerosol optical properties in a biogenically-influenced urban environment during the CARES campaign, Atmospheric Chemistry and Physics Discussions, 13, 7113-7150, 2013.
Heinson, Y. W., Maughan, J. B., Heinson, W. R., Chakrabarti, A., and Sorensen, C. M.: Light scattering Q-space analysis of irregularly shaped particles, J. Geophys. Res.: Atmos., 121, 682-691, 2016.
Henyey, L. G. and Greenstein, J. L.: Diffuse radiation in the galaxy, The Astrophysical Journal, 93, 70-83, 1941.
Liu, C., Chung, C. E., Yin, Y., and Schnaiter, M.: The absorption Ångström exponent of black carbon: from numerical aspects, Atmos. Chem. Phys., 18, 6259-6273, 2018.
Liu, L. and Mishchenko, M. I.: Scattering and radiative properties of complex soot and soot-containing aggregate particles, J. Quant. Spectrosc. Radiat. Transfer, 106, 262-273, 2007.
Liu, L., Mishchenko, M. I., and Arnott, W. P.: A study of radiative properties of fractal soot aggregates using the superposition T-matrix method, J. Quant. Spectrosc. Radiat. Transfer, 109, 2656-2663, 2008.
Moosmüller, H. and Ogren, J. A.: Parameterization of the aerosol upscatter fraction as function of the backscatter fraction and their relationships to the asymmetry parameter for radiative transfer calculations, Atmosphere, 8, 133, 2017.
Pandey, A. and Chakrabarty, R. K.: Scattering directionality parameters of fractal black carbon aerosols and comparison with the Henyey–Greenstein approximation, Opt. Lett., 41, 3351-3354, 2016.
Pandey, A., Chakrabarty, R. K., Liu, L., and Mishchenko, M. I.: Empirical relationships between optical properties and equivalent diameters of fractal soot aggregates at 550 nm wavelength, Opt. Express, 23, A1354-A1362, 2015.
Pandey, A., Patel, S., Pervez, S., Tiwari, S., Yadama, G., Chow, J. C., Watson, J. G., Biswas, P., and Chakrabarty, R. K.: Aerosol emissions factors from traditional biomass cookstoves in India: insights from field measurements, Atmos. Chem. Phys., 17, 13721-13729, 2017.
Pandey, A., Pervez, S., and Chakrabarty, R. K.: Filter-based measurements of UV–vis mass absorption cross sections of organic carbon aerosol from residential biomass combustion:

Preliminary findings and sources of uncertainty, J. Quant. Spectrosc. Radiat. Transfer, 182, 296-304, 2016.
Pandey, A., Shetty, N. J., and Chakrabarty, R. K.: Aerosol light absorption from optical measurements of PTFE membrane filter samples: sensitivity analysis of optical depth measures, Atmos. Meas. Tech., 12, 1365-1373, 2019.
Sorensen, C. M., Yon, J., Liu, F., Maughan, J., Heinson, W. R., and Berg, M. J.: Light scattering and absorption by fractal aggregates including soot, J. Quant. Spectrosc. Radiat. Transfer, 217, 459-473, 2018.
Subramanian, R., Roden, C. A., Boparai, P., and Bond, T. C.: Yellow beads and missing particles: Trouble ahead for filter-based absorption measurements, Aerosol Sci. Technol., 41, 630-637, 2007.
Virkkula, A.: Correction of the calibration of the 3-wavelength Particle Soot Absorption Photometer (3λ PSAP), Aerosol Sci. Technol., 44, 706-712, 2010.
Weingartner, E., Saathoff, H., Schnaiter, M., Streit, N., Bitnar, B., and Baltensperger, U.: Absorption of light by soot particles: determination of the absorption coefficient by means of aethalometers, J. Aerosol Sci, 34, 1445-1463, 2003.

Chapter 3: Accurate morphological representation of BC in optical parameterizations

Black carbon, also known as soot, is formed from high-temperature, incomplete combustion of a variety of fuels. In a typical combustion system, BC particles are first formed as spherical monomers (30-50 nm diameter) from the condensation of polyaromatic hydrocarbon precursors, after which they undergo Brownian collisions in 3-dimensional (3-d) space to form clusters of monomers (hereafter referred to as "aggregates") (Chakrabarty et al., 2014). This aggregate formation mechanism is now well studied as the Diffusion Limited Cluster Aggregation (DLCA) process (Sorensen, 2001; Chakrabarty et al., 2014). The resulting non-spherical morphology of the BC aggregates (interchangeably referred to as soot aggregates or SA) can be represented by the fractal scaling law for length-scales much greater than the monomer size (Sorensen et al., 1992; Liu et al., 2008; Chakrabarty et al., 2014):

$$N = k_0 \times \left(\frac{R_g}{r_0}\right)^{D_f} \tag{3.1}$$

where N is the number of particles enclosed within a radius of gyration R_g, r_o is the average monomer radius, D_f is the non-integral fractal dimension, and k_o is a constant prefactor. Thus, the structure of fractal aggregates can be completely defined using the parameters D_f and k_o, which quantify the aggregate geometry and packing factor of monomers, respectively (Wu and Friedlander, 1993). Both parameters are governed by the aggregate formation mechanism and the

aging processes encountered in the atmosphere (Zhang et al., 2008). Fresh aggregates formed by the DLCA mechanism have been universally observed to yield D_f and k_o values of ≈ 1.8 and 1.2, respectively (Sorensen et al., 1992; Chakrabarty et al., 2014). After release into the atmosphere, BC could change their morphology owing to atmospheric processing to form more compact, near-spherical structures with a D_f ≈2.6 [1].

BC particles are important drivers of climate change: they are strong visible-light absorbers, affect cloud formation and associated properties and alter the albedo of ice. Uncertainty in the radiative forcing estimates due to these particles plagues current climate models (Liu et al., 2008; Bond et al., 2013). Estimation of forcing from aerosols requires knowledge of their intrinsic optical properties–single scattering albedo (ω) and asymmetry parameter (g) or upscatter fraction (β) as a function of wavelength (Chakrabarty et al., 2014). The value of ω is a measure of brightness; it is 0 for a perfectly absorbing particle and 1 for a perfectly scattering particle. At a given wavelength, ω is defined as the ratio of the scattering cross-section (C_{scat}) to extinction cross-section, which is the sum of scattering and absorption (C_{abs}) cross-sections. The directionality of aerosol light scattering is represented in aerosol radiative transfer models using single-valued parameters–β or g (Wiscombe and Grams, 1976; Chylek and Wong, 1995; Bond and Bergstrom, 2006).

The following analytical expression (Bond and Bergstrom, 2006) describes the direct radiative forcing efficiency (termed simple forcing efficiency or SFE), per unit aerosol mass:

$$\frac{dSFE}{d\lambda} = -\frac{1}{4}\frac{dS(\lambda)}{d\lambda}\tau^2{}_{atm}(\lambda)(1-F_c)\times[2(1-a^2{}_s)\beta(\lambda)\,MSC(\lambda)-4a_s\,MAC(\lambda)] \quad (3.2)$$

where $dS(\lambda)/d\lambda$ is the spectral solar irradiance, τ_{atm} is the atmospheric transmissivity (typically fixed at 0.79), F_c is the cloud cover fraction (fixed at 0.6), a_s is the surface albedo (0.19 earth average), β is the value of upscatter fraction, MSC is the mass scattering cross-section and MAC is the mass absorption cross-section (C_{scat} and C_{abs}, respectively, normalized to the mass of the

particle). Average values for MSC and MAC of freshly emitted BC particles are 2.5 and 7.5 m^2/g, respectively, at 550 nm wavelength (Bond and Bergstrom, 2006; Chen, 2011). This calculation (with the prescribed values of τ_{atm}, F_c and a_s above) provides a reasonable approximation of top-of-the-atmosphere aerosol forcing under clear sky conditions (Moosmüller et al., 2009). The simplicity of this approximation lends itself to investigating the sensitivity of forcing to one or more of the aerosol properties.

Radiative transfer calculations made within climate models use more sophisticated forcing estimates than equation 3 but the same fundamental absorption and scattering (including directionality of scattering) properties are calculated in their aerosol optical models. Global models do not treat the morphological complexity of BC particles and employ a spherical approximation, despite significant discrepancies between MAC and MSC values predicted for spherical BC and those estimated from direct measurements (Bond et al., 2013).

3.1. BC optical properties as functions of measurable equivalent diameters

Current radiative transfer models usually approximate BC aggregates as equivalent spheres and use Lorenz-Mie analytical solutions for estimating their radiative properties. The aggregate structure of BC leads to interactions in the scattering and absorption behavior of neighboring monomers, which cannot be captured by the classical Lorenz-Mie theory (Liu et al., 2009; DeCarlo et al., 2004). Several studies conducted in recent years take into account the fractal nature of BC and calculate its numerically-exact optical properties (Liu et al., 2008; Moosmüller et al., 2009; Mishchenko et al., 2010). The absorption cross-section of a fractal soot aggregate (freshly emitted, D_f =1.8) is roughly 1.12-1.3 times that of a corresponding number of externally-mixed monomers but could be 0.85-1.5 times that of a volume equivalent sphere (Liu and Mishchenko, 2005b; Liu

et al., 2008). These discrepancies are much more exaggerated in the scattering cross-section and scattering directionality of aggregates. Without exception, the studies discussed above calculated the optical properties as a function of aggregate D_f and N. Although these results highlight the stark differences in optical properties between spherical and fractal morphology, they are ultimately found to be unusable by aerosol experimentalists and climate modelers in their research. Common instruments used for measuring equivalent aerosol diameters include the Scanning Mobility Particle Sizer (SMPS), the Single Particle Soot Photometer (SP2), and the Soot Particle - Aerosol Mass Spectrometer (SP-AMS). The SMPS, which is the most widely used aerosol size characterization instrument, measures a number size distribution for aerosols based on their electrical motilities (DeCarlo et al., 2004). It measures the particle mobility diameter, d_m, which is the diameter of a sphere having the same electrical mobility as that of an unknown particle. The SP2, on the other hand, calculates a mass equivalent diameter, d_{me}, for BC aggregates by measuring the visible-range radiation emitted from the refractory fraction of carbon in a particle as it is heated to its boiling point (Laborde et al., 2012). The SP-AMS is a combination of time-of-flight aerosol mass spectrometer (ToF AMS) and the SP2, and measures the vacuum aerodynamic diameter d_{Va} of a particle (Onasch et al., 2012). This diameter is defined as the diameter of a sphere with a density of 1 kg/m^3 and has the same settling velocity as the investigated non-spherical particle in the free-molecular regime (DeCarlo et al., 2004; Lindskog and Nordin, 2009). The motivation behind this work was to provide simple mathematical formulations connecting numerically-exact optical properties of BC aggregates and their measurable equivalent diameters.

3.1.1. Relationships between fractal parameters and equivalent diameters of aggregates

Computer simulation of a statistically significant number of 3-d BC aggregates with D_f =1.8 and 2.6, mimicking freshly-emitted and atmospherically aged BC particles, respectively, were first

performed. The prefactor k_o in our simulations was fixed at 1.19 per past recommendation (Sorensen and Roberts, 1997). For each D_f, at least one hundred aggregates were generated with N chosen randomly between 10 and 300 for each aggregate. A soot monomer diameter of 50 nm, typically observed in real-world particles (Liu et al., 2008), was used in our calculations. Each 3-d aggregate was oriented in 25 random orientations, with ~15 orientations, on an average, identified to be stable. For every identified stable orientation, three aggregate equivalent diameters – d_m, d_{me} and d_{Va} – were calculated. The d_m of an aggregate, in the transition flow regime, is equal to its stably-oriented projected area equivalent diameter as estimated from electron microscopy images (Park et al., 2004). Following this observation, d_m size distributions for our simulated aggregates were calculated from their stably-oriented projected images. The d_{me} of an aggregate was calculated as:

$$d_{me} = d_{mono} \times N^{\frac{1}{3}} \tag{3.3}$$

where d_{mono} (= 50 nm) is the diameter of monomers and N is the number of primary particles of an aggregate. The aggregate vacuum aerodynamic diameter d_{Va} was calculated using the established equation (DeCarlo et al., 2004):

$$d_{Va} = \frac{\rho_p}{\rho_o} \times \frac{d_{ve}}{\chi} \tag{3.4}$$

where ρ_p is the particle density (1.8 kg/m^3 for BC: (Bond et al., 2013)), ρ_o is the standard density (1 kg/m^3), d_{ve} is the volume equivalent diameter and χ is the dynamic shape factor in the free-molecular regime. In this work, d_{ve} was assumed to be equal to d_{me}, implying that the aggregates do not have any internal voids (DeCarlo et al., 2004). This is a reasonable assumption for chain-like freshly-emitted BC, but aged BC may have up to 10% internal voids (Bond and Bergstrom, 2006). The dynamic shape factor χ, in a given flow regime, is a measure of the increase in drag

force because of the non-spherical shape of the aggregate. The general expression for the shape factor for any flow regime is obtained as (DeCarlo et al., 2004):

$$\chi = \frac{d_m}{d_{ve}} \times \frac{C(Kn_{ve})}{C(Kn_m)} \quad (3.5)$$

Here C is the Cunningham slip correction factor and Kn_{ve} and Kn_m are the Knudsen numbers corresponding to d_{ve} and d_m, respectively. A mean free path of 4 m, representative of the high vacuum (10^{-3} to10^{-4} Pa) region at the end of the expansion zone in an AMS (DeCarlo et al., 2004), was used for calculating χ using Equation (3.5).

The calculated mean values of the three aerosol equivalent diameters are presented in Table 3.1. While d_{me} of an aggregate is independent of its D_f, the d_m values are observed to be decreasing with increasing D_f. This decrease becomes significant (as much as 25%) with increasing N. An explanation of this phenomenon is that D_f = 1.8 aggregates are open-ended fractals, which yield a larger 2-d projected area and d_m compared to the more collapsed and compact structured D_f = 2.6 aggregates. An alternate way of stating this is that D_f = 1.8 aggregates experience more drag force and therefore have lower mobility, which translates to a larger equivalent sphere diameter. From the perspective of drag force, D_f = 1.8 aggregates have smaller terminal velocities, which results in smaller d_{Va} than those of D_f = 2.6 aggregates for a fixed N. This effect of drag force on an aggregate is captured by the shape factor χ (Equation 3.5), which is a direct measure of the increase in drag force for a particle with its structural departure from spherical shape.

Table 3.1. Estimated equivalent aerosol diameters (nm) for fresh and aged soot aggregates as a function of monomer number (*N*)

N	Mobility diameter[1] (nm)		Mass equivalent diameter[2] (nm)	Vacuum aerodynamic diameter[1] (nm)	
	Fresh soot (D_f =1.8)	Aged soot (D_f =2.6)	Fresh and aged soot	Fresh soot (D_f =1.8)	Aged soot (D_f =2.6)
5	114±0.6	105±4.2	85	86±0.7	101±5.7
10	151±4.8	135±6.2	107	98±4.4	123±8.0
25	227±8.4	198±10	146	109±5.7	143±10.2
50	317±10.5	260±7.5	184	112±5.3	166±6.0
100	427±7.0	341±12	232	123±0.6	193±9.7
150	531±15	402±5.0	265	119±4.8	209±4.3
200	605±18.6	455±28	292	123±5.3	217±18.9
250	663±15.4	489±20	315	128±4.2	234±14.7
300	703±44	530±12	333	136±12.1	240±8.1

[1] All values given as mean+95% confidence intervals
[2] No standard deviation is associated with the mass equivalent diameter for a known N and D_f

3.1.2. Numerically estimated optical cross-sections and asymmetry parameter

The numerically-exact superposition transition matrix (*T*-matrix) method (Liu et al., 2008; Moosmüller et al., 2009) was used to determine the scattering and absorption cross-sections (C_{scat} and C_{abs}, respectively) and asymmetry parameter (g), of the simulated aggregates as a function of N and D_f. This method expresses the incident and transmitted fields as series of vector spherical functions. The relationship between the incident and transmitted electromagnetic field is captured by a 2 x 2 transition super matrix (or the *T*-matrix), which is a function of the intrinsic properties of the particle and the coordinate system (Mackowski and Mishchenko, 1996a; Mishchenko et al., 2002; Moosmüller et al., 2009). Each element of the matrices within this super matrix is calculated by numerically integrating the vector spherical functions of the incident and scattered fields over the particle surface. Past computational investigations conducted using this method have shown that D_f is an important parameter for accurately estimating the optical properties of an aggregate (Liu and Mishchenko, 2005a). Interactions between the monomers are significant for chain-like structures and become even more important as aggregates age and form closely packed compact

structures (Liu et al., 2008). A complex refractive index of 1.95–0.79i was chosen for the soot monomers in this work following the recommendation of Bond and Bergstrom for atmospherically relevant BC aggregates (Bond and Bergstrom, 2006).

Relationships between optical properties and equivalent aerosol diameters were determined using a non-linear least squares optimization technique known as the Trust-Region-Reflective Least Squares, implemented using the MATLAB Curve Fitting Toolbox. The goodness of fit for these equations is characterized by adjusted R-squared (R^2) and Root Mean Square Error (RMSE). Empirical equations correlating the numerically-exact aggregate optical properties C_{scat}, C_{abs} and g with the three aerosol diameters, d_m, d_{Va}, and d_{me} are reported for fresh (D_f = 1.8) and aged (D_f = 2.6) BC (Tables 3.2-3.4). The aggregate optical cross-sections exhibit simple power-law dependencies on the equivalent aerosol diameters. For correlating g, simple polynomial functional forms were found give the best fits to the data. At minimum, all the equations fits satisfy adjusted $R^2 \geq 0.86$ and RMSE < 0.03.

Table 3.2. Best fit empirical equations connecting the mobility diameter, d_m (in µm) and the optical properties of fresh and aged SA.

Optical property	Fresh SA (D_f =1.8)		Aged SA (D_f =2.6)	
	Equation	Adjusted R^2	Equation	Adjusted R^2
C_{scat}	$0.24\times(d_m^{2.8})$	0.998	$0.93\times(d_m^{3})$	0.998
C_{abs}	$0.4\times(d_m^{2.1})$	0.998	$0.8\times(d_m^{2.3})$	0.998
g	$-1.94\times d_m^{2}+2.51\times d_m-0.13$	0.993	$-3.7\times d_m^{2}+4.14\times d_m-0.36$	0.991

Table 3.3. Best fit empirical equations connecting the mass equivalent diameter, d_{me} (in µm) and the optical properties of fresh and aged SA.

Optical property	Fresh SA (D_f =1.8)		Aged SA (D_f =2.6)	
	Equation	Adjusted R^2	Equation	Adjusted R^2
C_{scat}	$5.83\times(d_{me}^{3.76})$	0.999	$6.75\times(d_{me}^{3.55})$	0.999
C_{abs}	$5.83\times(d_{me}^{3.76})$	1	$3.64\times(d_{me}^{2.70})$	0.999
g	$-9.77\times d_{me}^{2}+6.32\times d_{me}-0.35$	0.995	$-8.32\times d_{me}^{2}+6.55\times d_{me}-0.45$	0.998

Table 3.4. Best fit empirical equations connecting the vacuum aerodynamic diameter, d_{Va} (in µm) and the optical properties of fresh and aged SA.

Optical property	Fresh SA (D_f =1.8)		Aged SA (D_f =2.6)	
	Equation	Adjusted R^2	Equation	Adjusted R^2
C_{scat}	$2.9\times10^{6}\times(d_{Va}^{8.61})$	0.863	$595\times(d_{Va}^{5.88})$	0.994
C_{abs}	$4.43\times10^{5}\times(d_{Va}^{7.26})$	0.863	$96.28\times(d_{Va}^{4.38})$	0.996
g	$-112.7\times d_{Va}^{2}+38.12\times d_{Va}-2.38$	0.922	$-14.92\times d_{Va}^{2}+10.84\times d_{Va}-0.92$	0.972

Figures 3.1-3.3 show the best fit curves for the relationship between aggregate optical properties and equivalent diameters. These plots are typically non-linear, owing to the complex electromagnetic interactions between the point-contacting monomers in an aggregate.

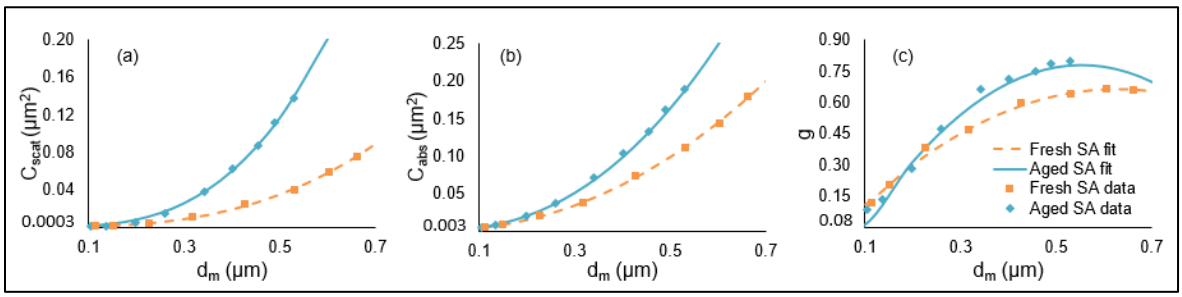

Figure 3.1: Variation of (a) C_{scat} (µm^2), (b) C_{abs} (µm^2), and (c) g, with mobility diameter, d_m (µm) of soot aggregates with D_f equal to 1.8 (fresh) and 2.6 (aged).

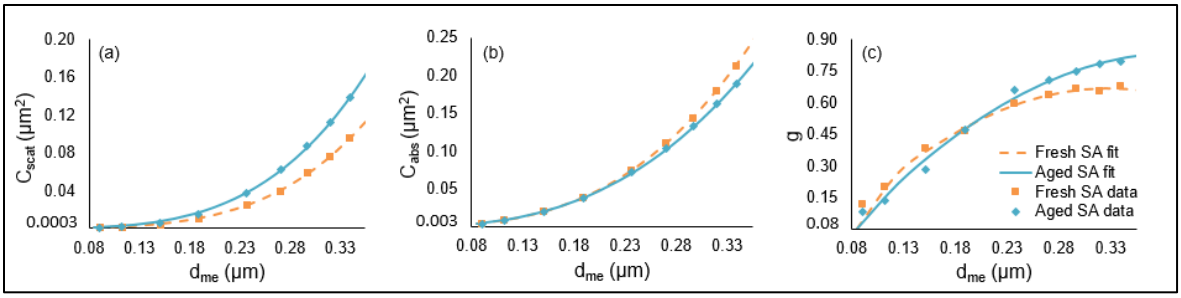

Figure 3.2: Variation of (a) C_{scat} (µm^2), (b) C_{abs} (µm^2), and (c) *g*, with mass equivalent diameter, d_{me} (µm) of soot aggregates with D_f equal to 1.8 (fresh) and 2.6 (aged).

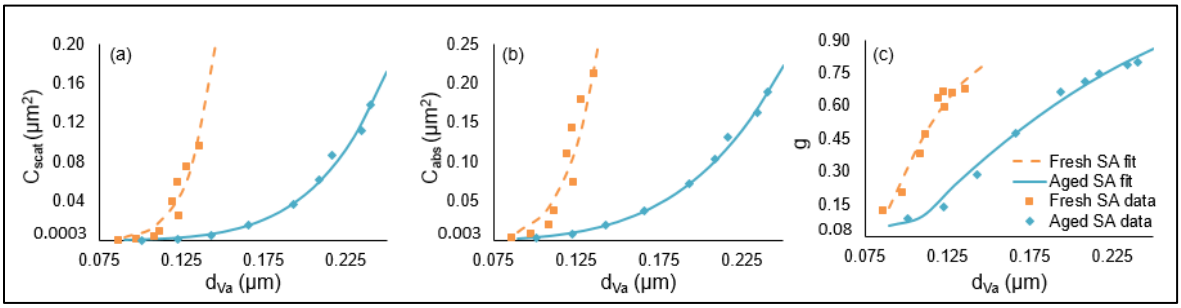

Figure 3.3: Variation of (a) C_{scat} (µm^2), (b) C_{abs} (µm^2), and (c) *g*, with vacuum aerodynamic diameter, d_{va} (µm) of soot aggregates with D_f equal to 1.8 (fresh) and 2.6 (aged).

From Figure 3.1, it can be seen that the aggregate optical cross-sections of aged BC aggregates have a steeper variation with mobility diameter compared to those of fresh BC. As aggregate D_f changes from 1.8 to 2.6, the aggregate morphology becomes more compact giving rise to intensification of monomer-monomer electromagnetic wave interactions. This manifests as a non-linear change in the aggregate scattering cross-sections and directionality which in turn affects the ω and *g* values. It must be noted that for a given value of d_m, an aged SA would contain a larger number of monomers (see Table 3.1), or a larger amount of material that can scatter and absorb light, than a fresh SA. This effect is partly responsible for the large gap between the fresh and aged SA curves in Figure 3.1. On the other hand, d_{me} is only a function of *N* and therefore the fresh and

aged SA curves in Figure 3.2 only reflect the increase in monomer-monomer interaction with aging. This significantly affects C_{scat} and g, while the change in C_{abs} due to aging is very small.

The variation of optical properties with d_{Va} is steeper for fresh SA than for aged SA (Figure 3.3), because a given value of d_{Va} corresponds to a larger number of monomers for a fresh SA than for an aged SA (Table 3.1). We found that for fresh SA, optical properties are not as strongly correlated with d_{Va} as they are with d_m and d_{me}. For fresh SA, d_{Va} shows a non-monotonic variation with N, wherein the same value of d_{Va} could correspond to two different values of N. In contrast, the investigated optical properties monotonically increase with N. This leads to a many-to-one relationship between optical properties and d_{Va}, resulting in relatively lower R^2 values for fresh SA (Table 3.4).

It should be noted that variations in refractive index of BC could alter the reported empirical relationships, especially for mass-equivalent aerosol diameter. Also noteworthy to mention is that freshly-emitted BC may have variations in their fractal prefactors, while aged BC may be hydrophilic in nature thereby resulting in different composition and/or surface structures than those simulated in this study. The fractal generation methodology and T-matrix calculations used in this work do not account for this effect. A thorough sensitivity analysis of varying fractal parameters and refractive index on the equivalent diameter and optical properties of BC is needed. Future work is also needed to investigate the influence of monomer overlap and sintering in comparison to point-contacting (as done in this study) on the variation in optical properties.

3.2. Relationships between scattering directionality parameters for BC aggregates

Scattering directionality parameters are condensed representations of the scattering phase function S_{11} of the aerosol system under study (illustrated in Figure 3.5). The Henyey-Greenstein (HG)

phase function (Henyey and Greenstein, 1941b; Marshall et al., 1995) is a simple, analytical function that is widely used for calculating and relating these parameters for atmospheric aerosols (Sagan and Pollack, 1967; Wiscombe and Grams, 1976; Sheridan and Ogren, 1999; Andrews et al., 2006). It does not explicitly take particle size and shape into consideration. Experimentally, the aerosol backscatter fraction b is measured using a nephelometer, and using the HG phase function relationships, approximate values of g and β are estimated. Alternatively, for spherical particles, g can be calculated using Mie theory for a known particle size (or size distribution) and refractive index. Improving the representation of radiative properties for BC particles in climate models and satellite retrieval algorithms has been an ongoing effort (Bond et al., 2013). Revising the approximate relationships between their g, β and b parameters with more accurate ones is a step towards that direction.

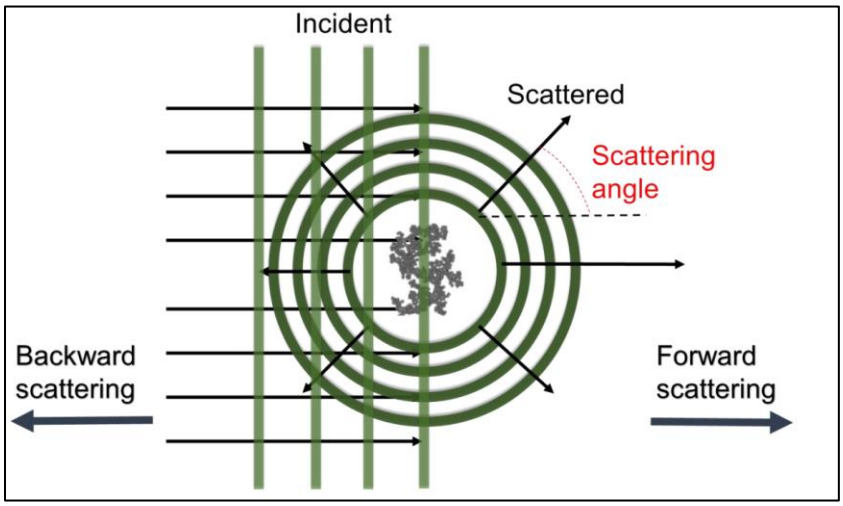

Figure 3.4: Illustration of a scattered waveform and the scattering angle relative to the incident radiation.

3.2.1. The scattering phase function and definitions of scattering directionality

The Stokes scattering matrix for a particle is a black representation of the relationship between the incident field and scattered field, as a function of the scattering angle (Mishchenko et al., 1996).

The first element of the matrix, that is S_{11}, satisfies the following normalization condition (Wiscombe and Grams, 1976):

$$\frac{1}{2}\int_0^{\pi} S_{11}(\theta)\sin\theta\, d\theta = 1 \qquad (3.6)$$

where θ is the scattering angle.

In this study, we examined the variations in β, g and b with BC aerosol morphology, for particle sizes and shapes typically found in the atmosphere. We used the numerically exact superposition *T*-matrix method to perform quantitative calculation of these parameters for simulated BC aggregates with varying mass fractal dimensions D_f (Mackowski and Mishchenko, 1996b; Mishchenko et al., 1996; Liu and Mishchenko, 2005b, 2007). We performed several simulations for generating aggregates with varying *N* and monomer diameter *d*. We assigned a range of values for the complex refractive index, *m*, of these aggregates based on past recommendations for atmospheric BC (Bond and Bergstrom, 2006). The choice of the wavelength of incident light was 550 nm, the peak of the visible solar spectrum.

Figure 3.6 shows the normalized S_{11} for D_f = 1.9 aggregates with varying values of *d*, *N*, and *m*. Increasing *d* or *N*, both of which correspond to an increase in the overall aggregate size, results in higher values of the S_{11} peak, or the near-forward scattering intensity. The S_{11} curves converge around scattering angle of 60°. By varying *m*, the normalized angular distribution of scattered radiation is unaltered. This behavior could be explained by the fact that scattering directionality is predominantly affected by variations in particle size and shape, and not *m* (Marshall et al., 1995; Liu and Mishchenko, 2005b). A similar invariant behavior of S_{11} was also observed for D_f = 3.0 aggregates (not shown here). Therefore, we excluded *m* as a varying parameter and fixed its value at 1.95-0.79i for all future analyses (Bond and Bergstrom, 2006).

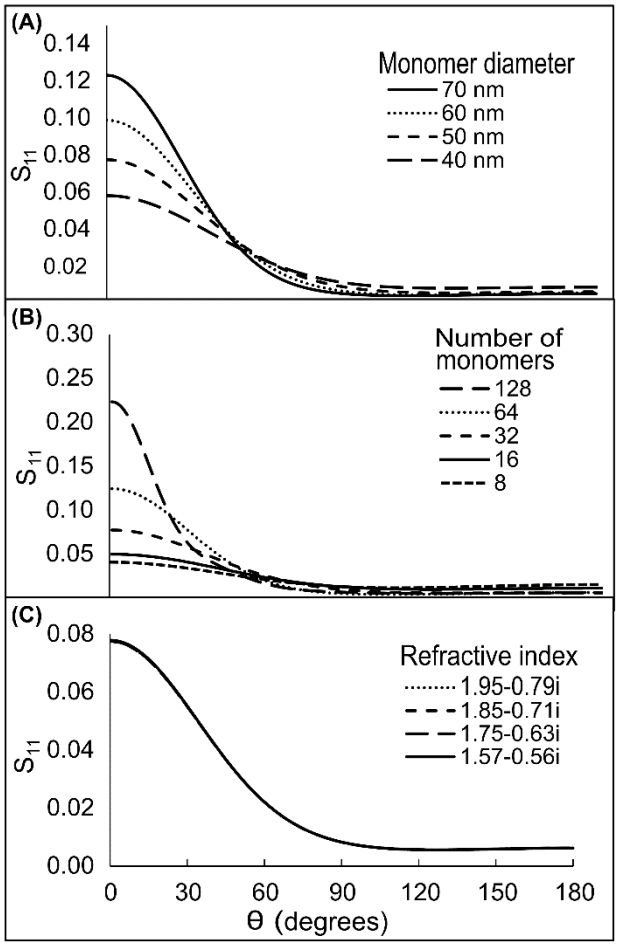

Figure 3.5: Normalized phase function S_{11} at 550 nm wavelength for D_f = 1.9 black carbon aggregates with varying (A) monomer diameter, (B) number of monomers, and (C) refractive index. For (A) and (B), the refractive index was fixed at 1.95-0.79i. For (B) and (C), the monomer diameter was fixed at 50 nm. For (A) and (C), the number of monomers was fixed at 32.

The β values our simulated aggregates can be estimated from the following definition:

$$\beta = \int_0^{\frac{\pi}{2}} \beta_{\theta_0} \sin\theta_0 \, d\theta_0 \tag{3.7}$$

where β_{θ_0} is the fraction of solar radiation scattered towards the upward hemisphere for a solar zenith angle of θ_0 and is a function of S_{11} as (Wiscombe and Grams, 1976; Schwartz, 1996):

$$\beta_{\theta_0} = \frac{1}{2\pi}\int_{\frac{\pi}{2}-\theta_0}^{\frac{\pi}{2}+\theta_0} S_{11}(\theta)\sin\theta\cos^{-1}(\cot\theta_0\cot\theta)d\theta + \frac{1}{2}\int_{\frac{\pi}{2}+\theta_0}^{\pi} S_{11}(\theta)\sin\theta\, d\theta \quad (3.8)$$

Note that b equals β for the case of zero solar zenith angle. The values of g and b were calculated using equations 3.9 and 3.10, respectively (Wiscombe and Grams, 1976; Andrews et al., 2006):

$$g = \frac{1}{2}\int_0^{\pi} S_{11}\sin\theta\cos\theta\, d\theta \quad (3.9)$$

$$b = \beta(\theta_0 = 0) = \frac{1}{2}\int_{\frac{\pi}{2}}^{\pi} S_{11}\sin\theta\, d\theta \quad (3.10)$$

3.2.2. The Henyey-Greenstein phase function

An approximate analytical expression for the angular distribution of light scattered by interstellar dust was developed by Henyey and Greenstein (1941b) and is widely used in atmospheric sciences for deriving the desired particle light-scattering directionality parameter from a measurement (b) or a modeled value (g). This phase function $P_{HG}(\theta)$ describes the angular distribution of the scattered light with the asymmetry parameter, g, as (Henyey and Greenstein, 1941a; Marshall et al., 1995; Boucher, 1998a)

$$P_{HG}(\theta) = \frac{1-g^2}{(1+g^2-2g\cos\theta)^{3/2}} \quad (3.11)$$

From equation 3.10 (plugging in P_{HG} as S_{11}), b_{HG} can be calculated as a function of g. However, this function cannot be inverted to yield an explicit function for calculating g as a function of b (as would be required in practice. Instead, a third-order polynomial approximation for the inverse relationship is typically used (Andrews et al., 2006):

$$g_{HG} = 7.143889b^3 + 7.464439b^2 - 3.9635b + 0.9893 \quad (3.12)$$

Similarly, Sheridan and Ogren (1999) have integrated the HG phase function to compute β_{HG} and b_{HG} (per equations 3.8 and 3.10, respectively) and provided a second-order polynomial to calculate the former in terms of the latter parameter:

$$\beta_{HG} = -2.9682b^2 + 1.8495b + 0.0817 \quad (3.13)$$

Finally, the following approximate relationship is available to calculate β_{HG} as a function of g_{HG} (Sagan and Pollack, 1967):

$$\beta_{HG} = \frac{(1-g_{HG})}{2} \quad (3.14)$$

Previous evaluations of the HG phase function (Marshall et al., 1995; Boucher, 1998b) for spherical particles have indicated discrepancies between asymmetry parameters derived using the phase function (g_{HG} from measured b) and those calculated using Mie theory for a measured size distribution.

3.2.3. Empirical relationships between the scattering directionality parameters

Scatter plots of *g* versus *b*, and *β* versus *b* are shown for varying values of *d* (Figure 3.7) and N (Figure 3.8). For values of *d* between 40-70 nm, the relationships between *g* and *b*, and *β* and *b* are nearly linear for both D_f = 1.9 and 3.0 aggregates. For D_f = 3.0 aggregates, with increasing *N*, *g* increases; while *β* decreases in an approximately linear fashion with increasing *b*. Contrarily, for D_f = 1.9 aggregates, the relationships of *g* and *β* with *b*, for different values of *N*, are non-linear, and not one-to-one. Consistent with our findings, previous *T*-matrix calculations for BC aggregates (Liu and Mishchenko, 2005b) have shown that g increases with increasing *N* for $N \leq 100$, beyond which the value of *g* saturates. Expectedly, *β* and *b* also show a similar behavior.

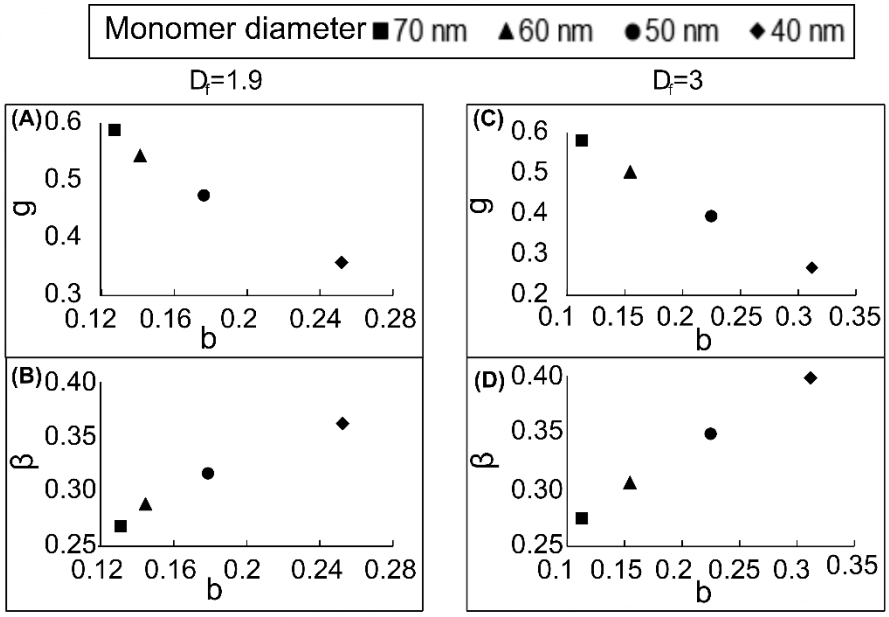

Figure 3.6: Scatter-plots of asymmetry parameter, g (panels A, C), and upscatter fraction, β (panels B, D), versus hemispherical backscattering fraction, *b*, for D_f = 1.9 and D_f = 3 aggregates, with varying monomer diameters. The number of monomers, refractive index and wavelength were fixed at 32, 1.95-0.79i, and 550 nm, respectively.

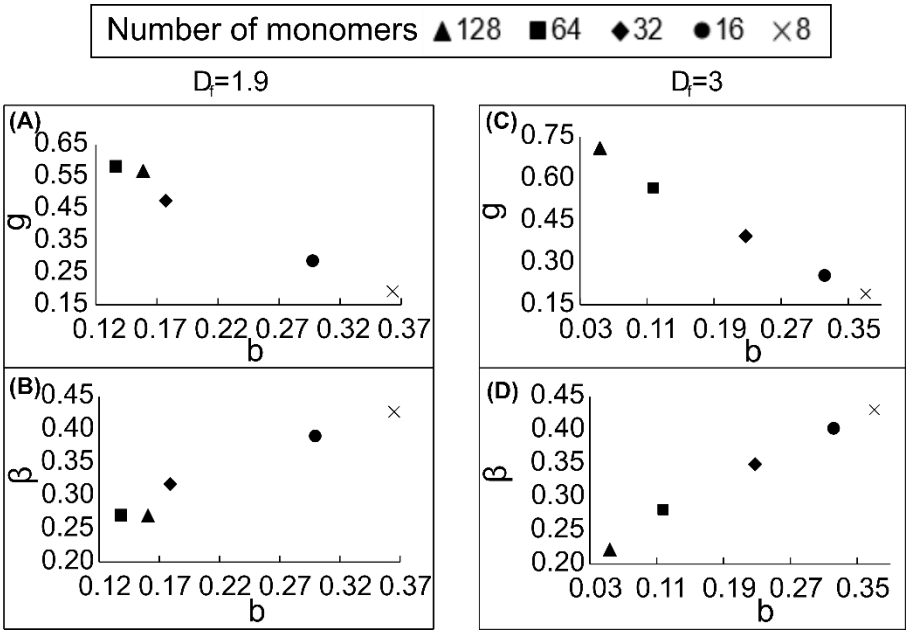

Figure 3.7: Scatter-plots of asymmetry parameter, g (panels A, C), and upscatter fraction, β (panels B, D), versus hemispherical backscattering fraction, *b*, for D_f = 1.9and D_f = 3 aggregates, with varying number of monomers. The monomer diameter, refractive index and wavelength were fixed at 50 nm, 1.95-0.79i, and 550 nm, respectively.

In Figure 3.9, we show the relationships between g and b (panel A), β and b (panel B), and β and g (panel C) calculated using *T*-Matrix for all aggregates simulated in this study. The g_{HG} and β_{HG} values obtained using equations 3.12-3.14 are plotted for comparison purposes. Values of g calculated using the HG phase function agree very well (within 5%) with those calculated using *T*-matrix for $0.4>b>0.2$. For $b<0.2$, use of equation 3.12 over-predicts g values by 5-10% for D_f = 3.0 aggregates, it under-predicts them for D_f = 1.9 aggregates. For D_f = 3 aggregates, we propose the following empirical expression for predicting the value of g for $0 \leq b < 0.4$ (with an adjusted-R^2 of 0.9988):

$$g = 0.9686b^2 - 2.021b + 0.8055 \qquad (3.15)$$

We find that equation 3.13 under-predicts β, by up to 25%, for D_f = 3 aggregates. A better relationship between β and b for these aggregates is (adjusted-R^2 of 0.9959):

$$\beta = -0.5582b^2 + 0.8973b + 0.1723 \quad (3.16)$$

For D_f = 1.9 aggregates, equation 7 under-predicts β values for 0.4>b>0.2. In this range of b, we suggest the use of equation 3.16 instead of equation 3.13. For b<0.2, use of equation 3.12 gives smaller error values (~5-8%) compared to equation 3.16. Finally, for both aggregate morphologies, the approximate equation 8 under-predicts the value of β, for a given value of g, by 10-35%. The following universal linear relationship between β and g was found to give significantly better predictions of β than equation 3.14, in the entire range of relevant g values (adjusted-R^2 of 0.9987):

$$\beta = -0.3978g + 0.505 \quad (3.17)$$

We further assessed the error that could be introduced in direct radiative forcing of BC from using the HG phase function approximation. The direct radiative forcing efficiency (W/g/nm) at 550 nm was calculated using equation 3.2: with $\frac{dS(\lambda)}{d\lambda}$ = 1.755 W/m^2/nm at 550 nm, MSC = 2.and MAC= 7.5 m^2/g. The upscatter fractions based on the HG phase function were estimated using two approaches. First, for the range of b values in this study, which can be measured in practice, we calculated the values of β from equations 3.13 and 3.16. The x- and y-axes of Figure 3.10A show the estimated $\frac{dSFE}{d\lambda}$using β from equations 3.13 and 3.16, respectively. Second, mass equivalent diameters were calculated for aggregates of different sizes, as $(N \times d^3)^{1/3}$. Values of g were calculated for these equivalent spheres using Mie theory (Mätzler, 2002) and corresponding β values were estimated using equation 3.14. To compare the deviation of these approximate β values from exact ones, we used equation 3.17 to estimate β based on the *T*-matrix method for the same set of aggregates (that is, same values of N, d and m). The values of $dSFE/d\lambda$ from Mie theory and

equation 3.14 are plotted on the x-axis of Figure 3.10B; the y-axis shows the corresponding values from *T*-matrix and equation 3.17.

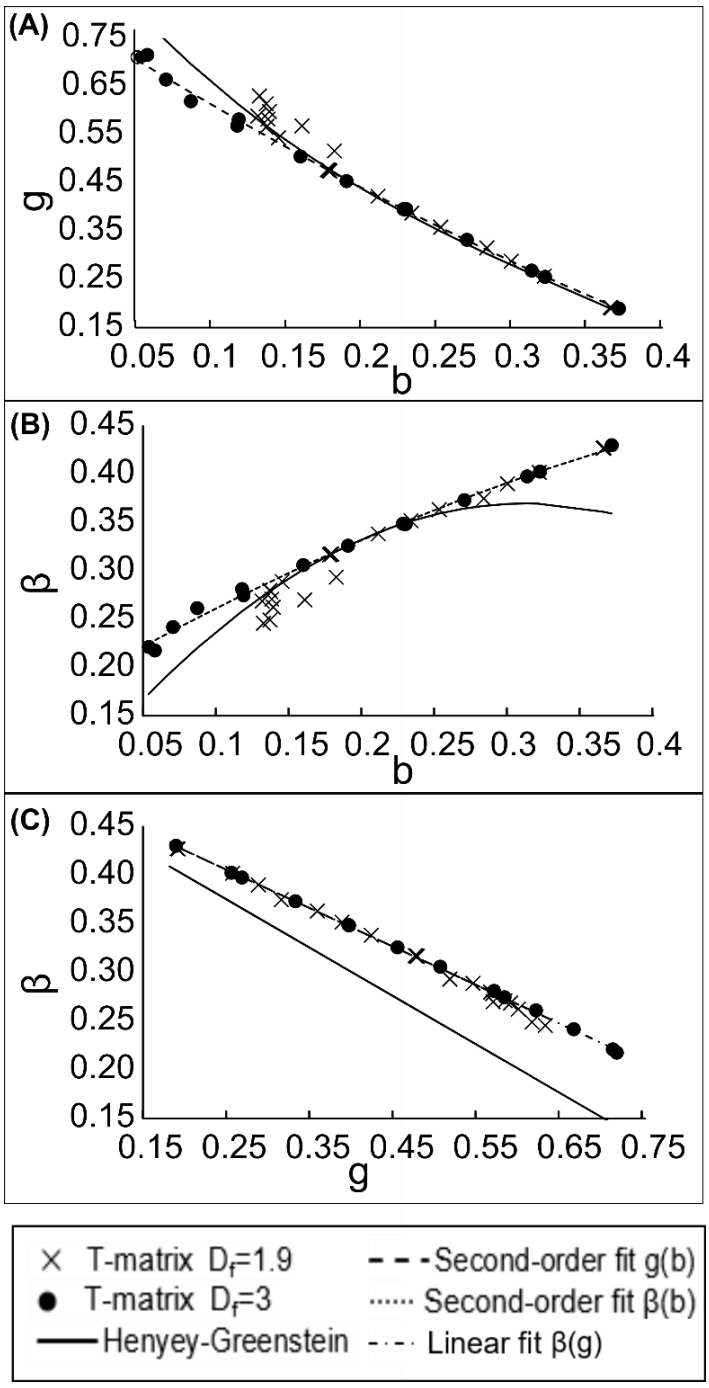

Figure 3.8: Relationships between (A) asymmetry parameter, *g*, and hemispherical backscattering fraction, *b*, (B) upscatter fraction, *β*, and *b*, and (C) *β* and *g*, at 550 nm wavelength, for D_f = 1.9 and D_f = 3 aggregates. The fits *g(b)*, *β(b)* and *β(g)* are given in Equation 3.15-3.17.

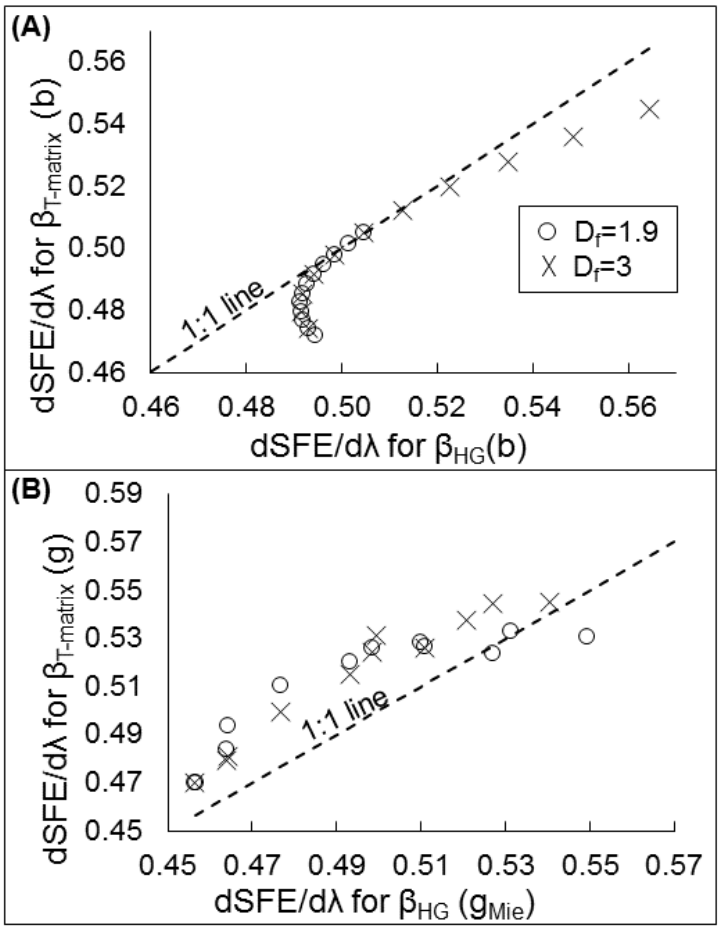

Figure 3.9: Scatter plots of simple forcing efficiency (W/g/nm) at 550 nm for upscatter fraction, β, estimated from a range of (A) backscatter fraction, *b*, values, using the HG approximation (equation 3.13) and *T*-matrix based relationship (equation 3.16), and (B) asymmetry parameter, *g*, values, using the HG approximation (equation 3.14) and *T*-matrix based relationship (equation 3.17). In equation 3.17, *g* was from *T*-matrix calculations for aggregates of different sizes, while Mie theory-based estimates of *g*, for equivalent spheres, were used in equation 3.14.

The simple forcing efficiencies estimated using the first method showed that the HG phase function based parameterization resulted in underestimation of β by 2-25% and overestimation of the forcing by up to 5%. In the second method, using Mie theory expectedly resulted in underestimation of *g* (Liu and Mishchenko, 2005b, 2007), which along with the use of the HG approximation, led to overestimation of β by 5-35%. This corresponded to underestimation of the forcing efficiency by up to 8%. The strongly absorbing nature of BC (MAC ~ 3 times of MSC),

implies that the second term (in brackets) on the RHS of equation 3.17 dominates. Therefore, while the use of the HG phase function approximation using equations 3.11-3.13 could cause significant errors in estimates of g and β, the resulting errors have relatively small contributions to forcing efficiency.

References

Andrews, E., Sheridan, P., Fiebig, M., McComiskey, A., Ogren, J., Arnott, P., Covert, D., Elleman, R., Gasparini, R., and Collins, D.: Comparison of methods for deriving aerosol asymmetry parameter, J. Geophys. Res.: Atmos., 111, 2006.

Bond, T. C. and Bergstrom, R. W.: Light absorption by carbonaceous particles: An investigative review, Aerosol Sci. Technol., 40, 27-67, 2006.

Bond, T. C., Doherty, S. J., Fahey, D., Forster, P., Berntsen, T., DeAngelo, B., Flanner, M., Ghan, S., Kärcher, B., and Koch, D.: Bounding the role of black carbon in the climate system: A scientific assessment, Journal of Geophysical Research: Atmospheres, 118, 5380-5552, 2013.

Boucher, O.: On Aerosol Direct Shortwave Forcing and the Henyey-Greenstein Phase Function, J. Atmos. Sci., 55, 128-134, 1998a.

Boucher, O.: On aerosol direct shortwave forcing and the Henyey–Greenstein phase function, Journal of the atmospheric sciences, 55, 128-134, 1998b.

Chakrabarty, R. K., Beres, N. D., Moosmüller, H., China, S., Mazzoleni, C., Dubey, M. K., Liu, L., and Mishchenko, M. I.: Soot superaggregates from flaming wildfires and their direct radiative forcing, Nature Scientific reports, 4, 2014.

Chen, Y.: Characterization of carbonaceous aerosols from biofuel combustion: emissions and climate relevant properties, 2011. Lawrence Berkeley National Laboratory, 2011.

Chylek, P. and Wong, J.: Effect of absorbing aerosols on global radiation budget, Geophys. Res. Lett., 22, 929-931, 1995.

DeCarlo, P. F., Slowik, J. G., Worsnop, D. R., Davidovits, P., and Jimenez, J. L.: Particle morphology and density characterization by combined mobility and aerodynamic diameter measurements. Part 1: Theory, Aerosol Sci. Technol., 38, 1185-1205, 2004.

Henyey, L. G. and Greenstein, J. L.: Diffuse Radiation in the Galaxy, Astrophys. J., 93, 70-83, 1941a.

Henyey, L. G. and Greenstein, J. L.: Diffuse radiation in the galaxy, The Astrophysical Journal, 93, 70-83, 1941b.

Laborde, M., Schnaiter, M., Linke, C., Saathoff, H., Naumann, K., Möhler, O., Berlenz, S., Wagner, U., Taylor, J., and Liu, D.: Single Particle Soot Photometer intercomparison at the AIDA chamber, Atmos. Meas. Tech., 5, 3077-3097, 2012.

Lindskog, M. and Nordin, E.: Ageing of Diesel Aerosols: Design and Implementation of a Teflon Simulation Chamber, Master, Engineering Physics, Ergonomics and Aerosol Technology, Department of Design Sciences, Lund University, 2009.

Liu, L. and Mishchenko, M. I.: Effects of aggregation on scattering and radiative properties of soot aerosols, Journal of Geophysical Research: Atmospheres (1984–2012), 110, 2005a.

Liu, L. and Mishchenko, M. I.: Effects of aggregation on scattering and radiative properties of soot aerosols, J. Geophys. Res.: Atmos., 110, 2005b.

Liu, L. and Mishchenko, M. I.: Scattering and radiative properties of complex soot and soot-containing aggregate particles, J. Quant. Spectrosc. Radiat. Transfer, 106, 262-273, 2007.

Liu, L., Mishchenko, M. I., and Arnott, W. P.: A study of radiative properties of fractal soot aggregates using the superposition T-matrix method, J. Quant. Spectrosc. Radiat. Transfer, 109, 2656-2663, 2008.

Mackowski, D. W. and Mishchenko, M. I.: Calculation of the T-matrix and the scattering matrix for ensembles of spheres, JOSA A, 13, 2266-2278, 1996a.

Mackowski, D. W. and Mishchenko, M. I.: Calculation of the T matrix and the scattering matrix for ensembles of spheres, JOSA A, 13, 2266-2278, 1996b.
Marshall, S. F., Covert, D. S., and Charlson, R. J.: Relationship between asymmetry parameter and hemispheric backscatter ratio: Implications for climate forcing by aerosols, Appl. Opt., 34, 6306-6311, 1995.
Mätzler, C.: MATLAB functions for Mie scattering and absorption, version 2, IAP Res. Rep, 8, 2002.
Mishchenko, M. I., Travis, L. D., and Lacis, A. A.: Scattering, absorption, and emission of light by small particles, Cambridge university press, 2002.
Mishchenko, M. I., Travis, L. D., and Mackowski, D. W.: T-matrix computations of light scattering by nonspherical particles: a review, J. Quant. Spectrosc. Radiat. Transfer, 55, 535-575, 1996.
Mishchenko, M. I., Zakharova, N. T., Videen, G., Khlebtsov, N. G., and Wriedt, T.: Comprehensive T-matrix reference database: A 2007-2009 update, Journal of Quantitative Spectroscopy and Radiative Transfer, 111, 650-658, 2010.
Moosmüller, H., Chakrabarty, R., and Arnott, W.: Aerosol light absorption and its measurement: A review, J. Quant. Spectrosc. Radiat. Transfer, 110, 844-878, 2009.
Onasch, T., Trimborn, A., Fortner, E., Jayne, J., Kok, G., Williams, L., Davidovits, P., and Worsnop, D.: Soot particle aerosol mass spectrometer: development, validation, and initial application, Aerosol Sci. Technol., 46, 804-817, 2012.
Park, K., Kittelson, D. B., and McMurry, P. H.: Structural properties of diesel exhaust particles measured by transmission electron microscopy (TEM): Relationships to particle mass and mobility, Aerosol Sci. Technol., 38, 881-889, 2004.
Sagan, C. and Pollack, J. B.: Anisotropic nonconservative scattering and the clouds of Venus, J. Geophys. Res., 72, 469-477, 1967.
Schwartz, S. E.: The whitehouse effect—Shortwave radiative forcing of climate by anthropogenic aerosols: An overview, J. Aerosol Sci, 27, 359-382, 1996.
Sheridan, P. J. and Ogren, J. A.: Observations of the vertical and regional variability of aerosol optical properties over central and eastern North America, J. Geophys. Res.: Atmos., 104, 16793-16805, 1999.
Sorensen, C.: Light scattering by fractal aggregates: a review, Aerosol Sci. Technol., 35, 648-687, 2001.
Sorensen, C., Cai, J., and Lu, N.: Light-scattering measurements of monomer size, monomers per aggregate, and fractal dimension for soot aggregates in flames, Appl. Opt., 31, 6547-6557, 1992.
Sorensen, C. M. and Roberts, G. C.: The prefactor of fractal aggregates, J. Colloid Interface Sci., 186, 447-452, 1997.
Wiscombe, W. and Grams, G.: The backscattered fraction in two-stream approximations, Journal of the Atmospheric Sciences, 33, 2440-2451, 1976.
Wu, M. K. and Friedlander, S. K.: Note on the power law equation for fractal-like aerosol agglomerates, J. Colloid Interface Sci., 159, 246-248, 1993.
Zhang, R., Khalizov, A. F., Pagels, J., Zhang, D., Xue, H., and McMurry, P. H.: Variability in morphology, hygroscopicity, and optical properties of soot aerosols during atmospheric processing, Proc. Natl. Acad. Sci. U. S. A., 105, 10291-10296, 2008.

Chapter 4: Aerosol emission factors from field study of cookstove emissions in India

Emissions performance of cookstoves is commonly expressed in terms of mass-based emission factors (EFs) or mass of pollutant emitted per unit mass of fuel burned. PM emission rates depend on fuel properties, combustion device, operator behavior and cooking patterns (Roden et al., 2009; Sahu et al., 2011; Leavey et al., 2015). Cookstove heating efficiencies and EFs are often measured in a laboratory setting using a water-boiling test (WBT) with high- (boiling) and low- (simmering) power phases (Smith et al., 2000; Habib et al., 2008; MacCarty et al., 2008). These standardized tests are useful for comparing different stove-fuel combinations, but they do not represent real-world stove behaviors found in the field (Roden et al., 2006; Smith, 2007; Roden et al., 2009). Habib et al. (2008) changed the amount of water boiled from 0.5 kg to 1.5 kg in the WBT test, thereby changing the fuel burn rate and burn cycle duration and observed a factor of ~2.7 increase in the $PM_{2.5}$ EF and a factor of ~2 increase in the OC fraction. A real-world study of Honduran wood-burning cookstoves (Roden et al., 2006) found higher $PM_{2.5}$ EFs and OC content than those from previous laboratory studies. Roden et al. (2006; 2009) found that real-world fire tending and cooking practices (and therefore burn conditions) were important factors determining PM EFs and compositions.

Real-world EFs for commonly used fuel types and cooking technologies in India are needed for accurate bottom-up emission estimates (Bond et al., 2004; Bond et al., 2013; Pandey et al., 2014). Inventoried emission rates serve as inputs to regional and global atmospheric transport models that predict spatiotemporal profiles of pollutant burdens and associated impacts on climate and human

health (Schulz et al., 2006; Bond et al., 2013; Guttikunda and Calori, 2013; Sadavarte et al., 2016). Alternatively, these inventories are used in conjunction with impact metrics such as intake fraction (Grieshop et al., 2011) and global warming potential (Shindell et al., 2012) to evaluate mitigation policies (MHFW, 2015; Sagar et al., 2016). Such measurements identify key parameters to be monitored during laboratory testing and appliance certification.

4.1. Experimental and data analysis techniques

With the above goals, we measured cookstove emission characteristics in a rural Indian household (Pandey et al., 2017). Local meals were prepared with a traditional mud stove or *chulha* (Figure 4.1) using biomass fuels collected from different regions of India. Real-time measurements of emitted gas concentrations were conducted, and $PM_{2.5}$ filter samples were collected at regular time intervals during each cooking cycle. $PM_{2.5}$, OC and EC EFs are reported here as a function of fuel-type and combustion phase. Thermal carbon fractions provided by the IMPROVE_A protocol are also examined.

Figure 4.1: Traditional one-pot mud *chulha* used in this work.

Thirty separate cooking tests were conducted between December 19 and 30th of 2015 in a rural household on the outskirts of Raipur, a city located in the central Indian state of Chhattisgarh (abbreviated as Chh.). ~77% of Chhattisgarh households are located in rural areas and rely almost

entirely on solid biomass fuels for cooking (Census, 2011). On a national level, fuel-wood, agricultural residue and dung are used as primary cooking fuels by 49%, 9% and 8% Indian households respectively (Census, 2011). Accounting for average combustion efficiencies and calorific values of these fuels, annual fuel usage estimates are 250 MT fuel-wood, 73 MT agricultural residue and 100 MT dung (Pandey et al., 2014). For this study, fuel-wood was obtained from Uttar Pradesh (U.P.), Rajasthan (Raj.), Andhra Pradesh (A.P.), Bihar, and Punjab which collectively account for 35% of the total fuel-wood user base in India. All wood fuels were in the form of chunks with typical dimensions of 5 – 15 cm. Cattle dung (in the form of dung cakes dried in the sun) was collected from U.P. and Bihar, which account for 60% of the dung use for cooking in India. Agricultural residues from *tur* crops (a type of woody stalk) and rice straw were procured from a village near the study location. Test fuels were collected and stored in sealed bags, and later analyzed for elemental (carbon, oxygen, hydrogen, nitrogen) composition and moisture content. Fuel compositions are compared in Table 4.1. Per real-world practice, fuel samples were naturally dried in the sun and stored indoors, bringing moisture contents to < 9%. These compositions are consistent with those reported in other tests (Smith et al., 2000; Habib et al., 2008).

Table 4.1: Elemental composition and moisture content of the biomass fuels in this study.

Fuel	Elemental composition (%)				Moisture content (%)
	Carbon	Hydrogen	Oxygen	Nitrogen	
U.P. dung	33.1	4.0	30.0	1.6	7.5
Bihar dung	41.4	5.1	33.6	2.1	8.6
Chh. rice straw	40.7	5.5	39.0	0.8	5.3
Chh. *tur* stalk	48.4	6.5	42.7	0.6	4.8
Punjab wood	50.3	0.2	40.9	0.4	6.2
Raj. Wood	49.7	5.6	42.9	0.1	8.1
U.P. wood	49.9	0.1	41.8	0.2	5.6
A.P. wood	48.3	0.1	43.4	0.7	3.1

Table 4.2 describes the fuels used and the foods cooked; replicate tests were made for some of these combinations with at least three for each fuel. Dung (20-50 g) was doused with approximately 10 ml kerosene for initial ignition and the test fuel was added after a steady flame was achieved. Additional fuel of the same type was added as needed to complete the recipe. A ten-minute period following lighting of the fire is designated as *ignition* phase. The remainder of the cooking cycle was designated as the *flaming* phase when a visible flame was present. Combustion entered the *smoldering* phase when the flame died down. The U.P. dung and Chh. rice straw could not sustain the flaming phase for more than a few minutes. Dung is typically smoldered for low-power cooking applications, and it is used as kindling material for igniting fuel-wood in a typical rural household. The low carbon content of U.P. dung (Table 4.1) possibly hinders its ability to sustain a flame, more so than Bihar dung. Rice straw has a low material density and high surface-to-volume ratio, and therefore tends to burn out very quickly. It also produces large amounts of smoke, making its use as a standalone fuel impractical and harmful for the cook's health. To

circumvent these limitations, a few experiments established a steady flame using U.P. dung/Chh. rice straw mixed with U.P. wood (approximately 2.5:1 ratio of test fuel mass to wood mass).

Table 4.2: List of cooking experiments conducted during the 10-day intensive study period. Abbreviations for Indian states: U.P. = Uttar Pradesh, Raj. = Rajasthan, A.P. = Andhra Pradesh, Chh. = Chhattisgarh.

Day	Primary fuel used	No. of replicate experiments	Food cooked
1	Bihar dung	1	lentil-rice
2	U.P wood	2	rice, vegetables
3	U.P wood	1	tea
	Raj. wood	4	lentils, rice, vegetables
4	U.P. wood	2	lentils
	A.P. wood	1	rice
5	A.P. wood	2	rice, vegetables
	Bihar dung	1	tea
6	Chh. *tur* stalks	3	rice, vegetables, tea
7	U.P. dung[a]	3	vegetables, rice
	Bihar dung	1	tea
8	Chh. rice straw[a]	3	rice, vegetables
	Chh. wood	1	tea
9	Raj. wood	4	water heated, rice and curry
10	Punjab wood	1	milk porridge

[a] Two experiments for each fuel conducted with fuel-wood mixed with the test fuel

The test kitchen (Figure 4.2) was on the first floor of house, separate from all other rooms. A permanently open door was the only entry from an open terrace. A partially covered window was a second ventilation source. The sampling and measurement systems are shown in Figure 4.3. The combustion device was a traditional mud *chulha*; such stoves have poor heat insulation, poor combustion efficiency and do not allow proper mixing of fuel and air (Smith et al., 2000;

Venkataraman et al., 2010). An eight-armed stainless steel probe (based on Roden et al. (2006)) sampled naturally-diluted emissions at ~1.2 m above the top of the stove. Each arm of the probe was 0.5 m in length, with 4 uniformly placed holes facing the plume. This probe was connected to three real-time instruments−a Kanomax Portable Mobility Particle Sizer (PAMS) (Kulkarni et al., 2016), a TSI Sidepak (Zhu et al., 2007), and a Testo-350 gas analyser (Wang et al., 2012). The PAMS recorded particle size distributions from 10 – 400 nm mobility diameter. The Sidepak provides a light-scattering (670 nm) surrogate for measured $PM_{2.5}$ mass that is calibrated with Arizona Road Dust (O'Shaughnessy and Slagley, 2002). PM concentrations exceeded the upper measurement limits of these instruments during high emission episodes. The Testo-350 gas analyzer was factory-calibrated prior to the experiments for carbon monoxide (CO) and carbon dioxide (CO_2). Measured concentrations (acquired every second) were at least five times the detection limits of 1 ppm CO and 0.01 % CO_2 by volume. $PM_{2.5}$ was collected on 47 mm Teflon-membrane and pre-baked quartz-fiber filters several times during a cooking cycle using Minivol (5 L min^{-1}) samplers (AirMetrics Model 4.2) with greased impactor inlets located in the plume ~0.9m above the stove. Filter sample durations ranged from 0.5 to 4 minutes, based on the continuous SidePak reports, to prevent filter overloading. Field blanks were collected (minimum sampling duration of 15 minutes) each day before testing. The Teflon filters were weighed before and after sampling to obtain the net mass deposit which was divided by the sample volume (flow rate times duration) to obtain the concentration. The mass of Teflon filter deposits ranged 50 – 300 µg. Quartz filters were analyzed using the Interagency Monitoring of Protected Visual Environments – A (IMPROVE_A) thermal-optical reflectance (TOR) method (Chow et al., 2007b; 2011) to determine elemental and organic carbon fractions in the sampled particulates. The

minimum detection limits of the TOR analysis are about 9 µg for OC and 1 µg for EC (Solomon et al., 2014).

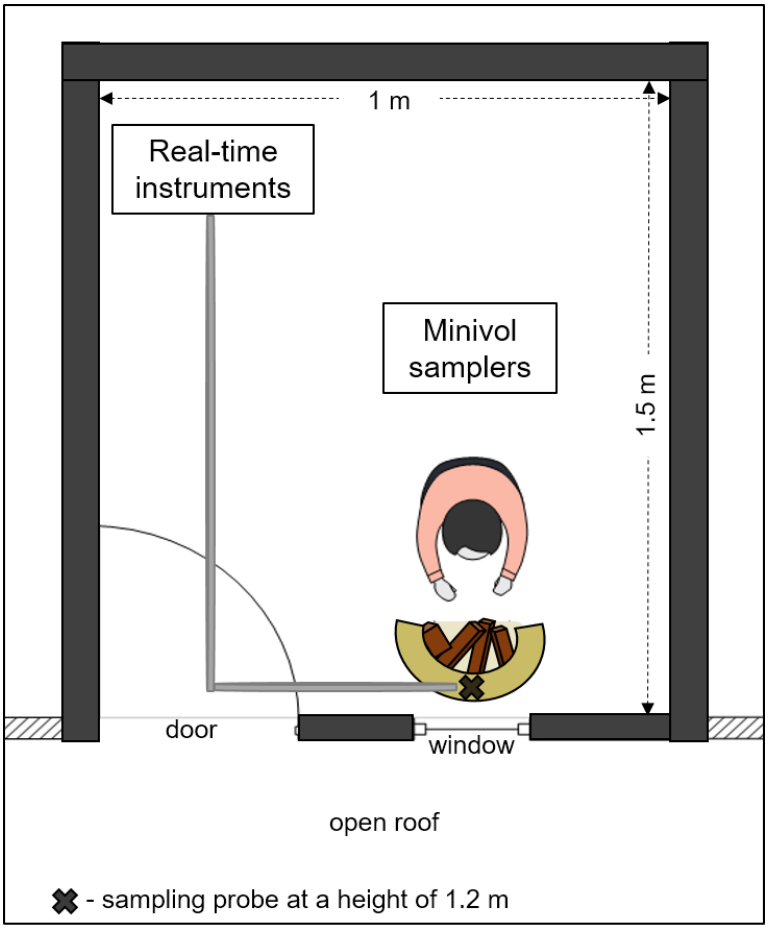

Figure 4.2: Schematic layout (top-view) of the kitchen.

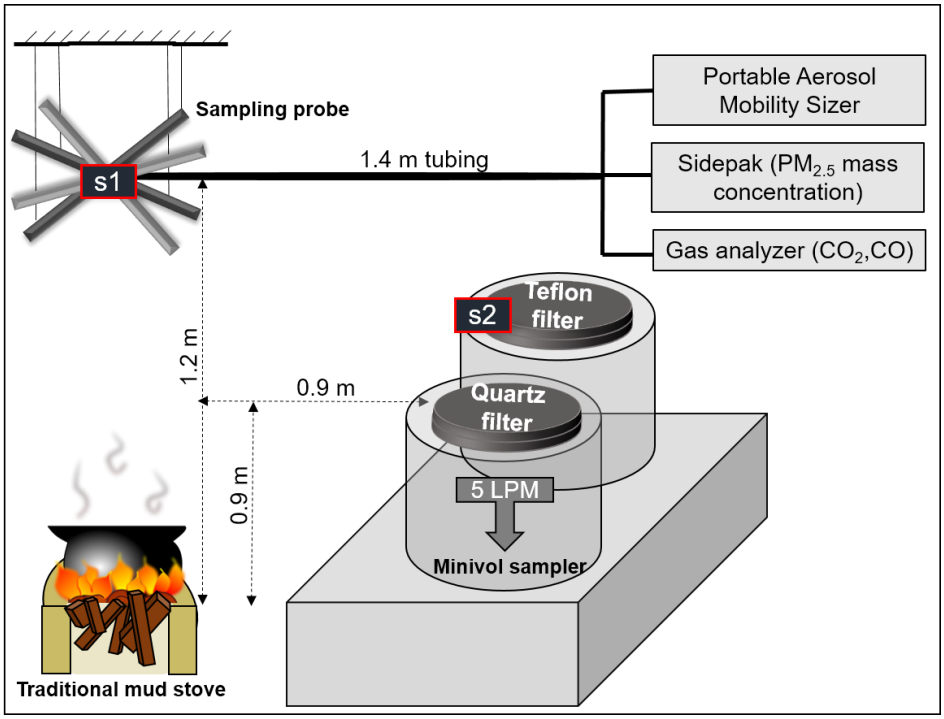

Figure 4.3: Schematic representation of the experimental setup. S1 and S2 denote the position of the wireless optical sensors.

Using the carbon mass balance technique, fuel-based EFs were calculated for each filter:

$$EF_i = CMF_{fuel} \frac{C_i}{\Delta C_{CO_2}\left(\frac{M_C}{M_{CO_2}}\right) + \Delta C_{CO}\left(\frac{M_C}{M_{CO}}\right)} \quad (4.1)$$

where EF_i is the EF of species *i* in grams emitted per gram of fuel consumed. CMF_{fuel} is the carbon mass fraction of the fuel, which ranged from 33% to 50% for the tested fuels. C_i is the concentration of emittant *i*, in this case $PM_{2.5}$, OC, or EC, in g m^{-3}, determined for each Teflon and quartz filter. ΔC_{CO2} and ΔC_{CO} are the concentrations above ambient levels of CO_2 and CO in g m^{-3}, respectively. M_C, M_{CO2}, and M_{CO} are the atomic or molecular weights of C, CO_2, and CO in g $mole^{-1}$.

Wireless optical particle sensors (details available in Patel et al. (2017)) were attached to the Minivol sampler and the sampling probe during six experiments to check for any significant differences in the particle concentrations measured at the two locations. Measurements where

either sensor was saturated were discarded, and a linear regression analysis performed on the valid data points (Figure 4.4). The saturation voltage for the sensors is close to 750 mV, discarding all values higher than 750 mV, regression analysis of the remaining points yields a slope of 0.96. However, if the saturation threshold was set at 745 mV, the slope changed to 0.89. This is probably because saturation behavior for these sensors is a soft-limit saturation, such that the input-response relationship becomes non-linear at some voltage lower than the final limiting value of 750 mV. If measurements from this non-linear region are included, the linear regression analysis would give erroneous results. Therefore, we systematically reduced the threshold values until we observed negligible change in the regression slope. Finally, we discarded the data points where either of the sensors had readings above the linearity threshold (720 mV). About 60% of all data points were used, and a slope of 0.63 (R^2=0.65) was obtained. Therefore, the concentration measured by the Minivol sampler was adjusted upwards by a factor of 1.6 (=1/0.63). Equation 1 assumes that the carbon emitted in CH_4, NMHC, and PM is negligible compared to that in CO and CO_2, it was therefore corrected to account for the small fraction of fuel carbon that gets converted to gaseous volatile organic carbon, assumed as 2.4% (Roden et al., 2006; Habib et al., 2008).

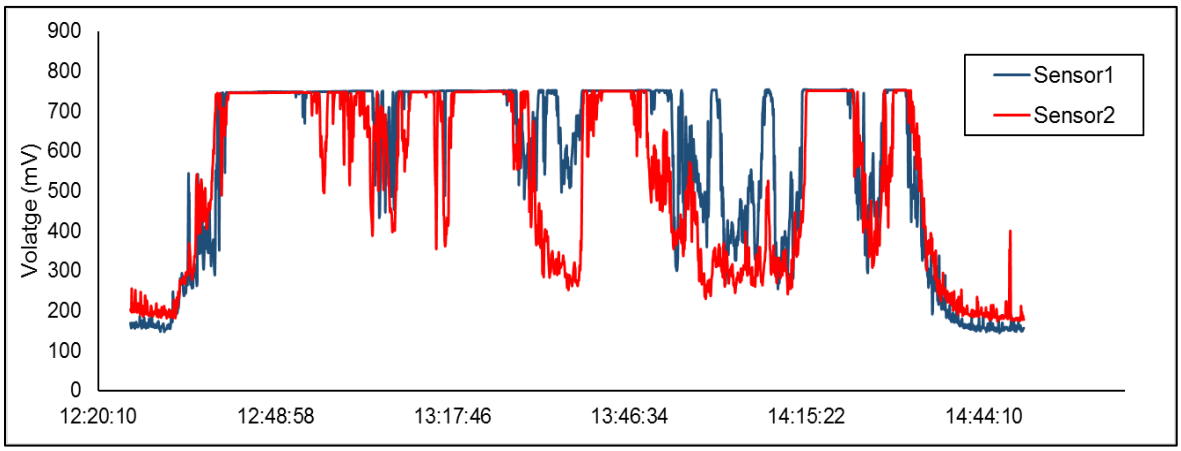

Figure 4.4: Raw signals from the PM sensors located at the sampling probe (Sensor1) and the Minivol $PM_{2.5}$ sampler (Sensor2) during one cooking test.

4.2. Emission factors by fuel and combustion phase

EFs for all the test fuels are represented as box-and-whisker plots in Figure 4.5. There were no statistically significant (unpaired, two-sided Student's *t*-test at p=0.05) EF differences for wood fuels from different regions of India. This can be interpreted as the variability in emissions for a given fuel being comparable to the differences in average emission rates for different wood fuels. Note that all fuel-wood types had low moisture contents (naturally dried for ease of use) and were chopped in roughly the same manner even though individual wood pieces varied in size. Bihar dung EFs exceeded those for U.P. dung, possibly owing to the addition of wood to sustain flaming. On average, $PM_{2.5}$ and OC emission factors for dung were higher than those for fuel-wood. EFs for dung, rice straw and *tur* stalk show a larger spread than corresponding EFs for fuel-wood. A detailed list of all emission factors (speciated by fuel and combustion stage) is provided in Appendix A2.

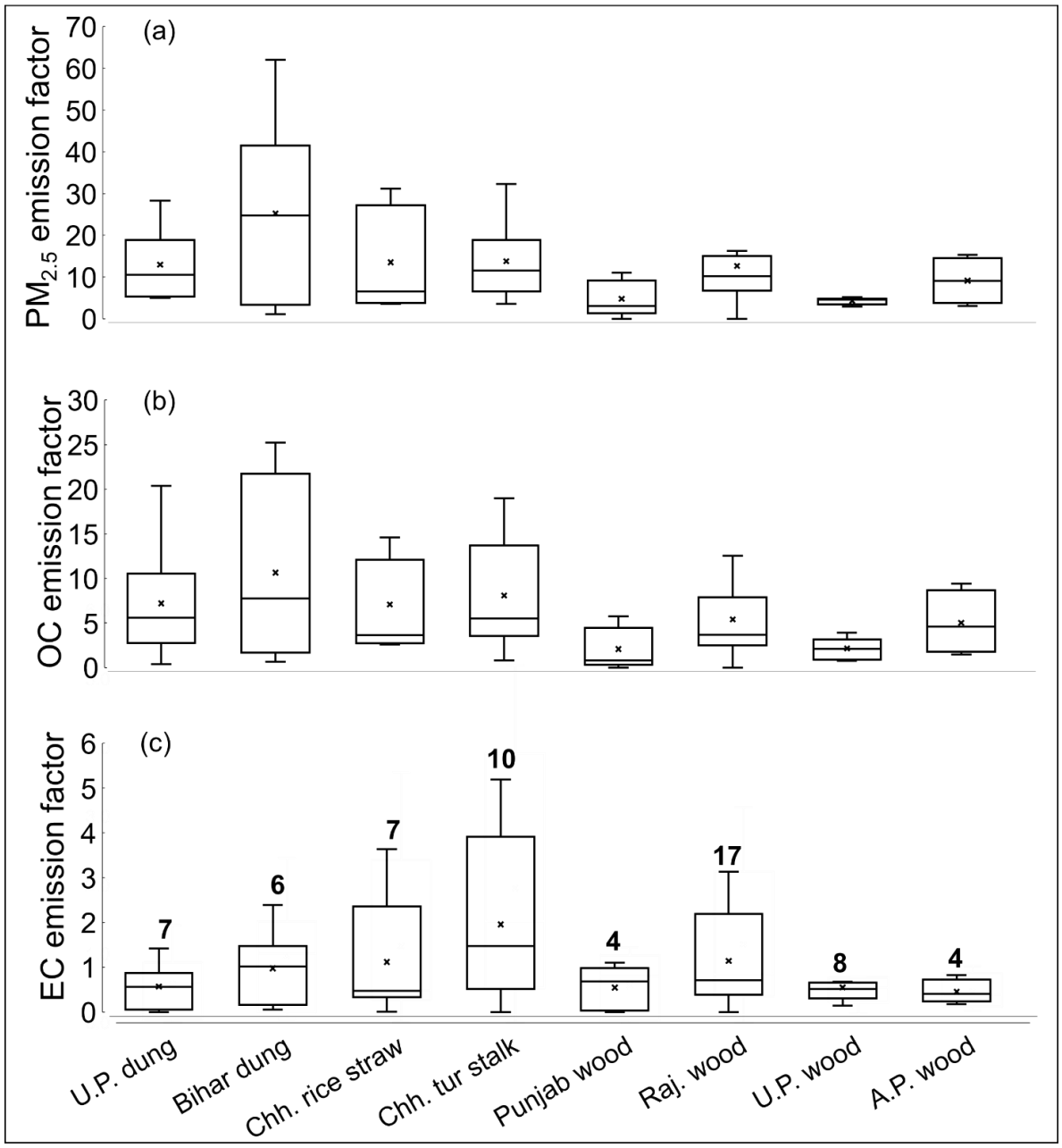

Figure 4.5: Box plots of (a) $PM_{2.5}$ emission factors, (b) OC emission factors, and (c) EC emission factors. All emission factorss are expressed in g-pollutant per kg of fuel burnt. Boxes denote lower and upper quartiles; whiskers are 1.5 times the interquartile ranges of the upper and lower quartiles. The numbers above the error bars in panel (c) indicate the number of samples for each fuel.

Figure 4.6 compares EFs for the different burning phases. $PM_{2.5}$ EFs are highest during the ignition phase for all fuels. The OC/EC ratio (Figure 4.6b) increases from ignition and flaming, to smoldering for all fuels. Similarly, emission factors of CO are shown in Figure 4.7. Expectedly, smoldering combustion is associated with the largest CO emissions. Both CO and $PM_{2.5}$ are products of incomplete combustion are their mass emission rates measured during lab cookstove tests are found to correlate (Roden et al., 2009). In this study, no correlation was observed between the estimated CO emission factors and corresponding $PM_{2.5}$ emission factors (Figure 4.8A), consistent with a similar analysis of field study results in Roden et al. (2009). Further, we plotted modified combustion efficiencies (MCE), calculated as the ratio of CO_2 concentration to $CO+CO_2$ concentration, against OC-to-EC ratios. MCE is typically treated as an identifier of combustion phase, with values greater than 0.9 associated with (Reid et al., 2005; Zhang et al., 2008). We found estimated MCE values above 0.9 for roughly 90% of all run time, even when no flaming phase was visibly observed. They showed no correlation with OC-to-EC ratios (Figure 4.8B).

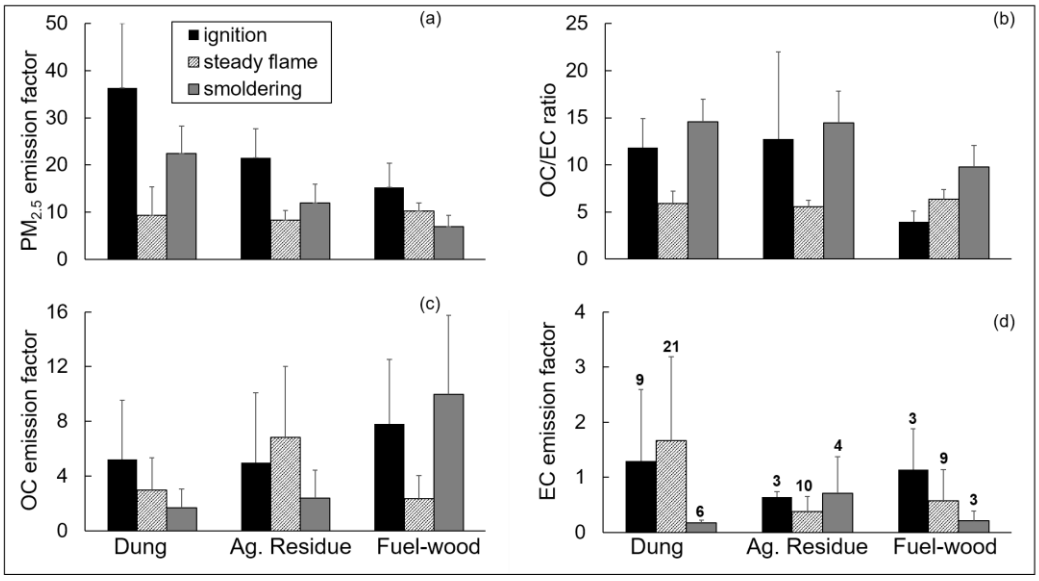

Figure 4.6: Fuel-wise average values of (a) $PM_{2.5}$ emission factors, (b) OC/EC ratios, (c) OC emission factors, and (d) EC emission factors, categorized by observed combustion phases. All emisssion factors are expressed in g-pollutant per kg of fuel burnt. One-sided error bars

are shown to denote one standard deviation from the mean. The numbers above the error bars in panel (d) indicate the number of samples for each fuel and combustion phase.

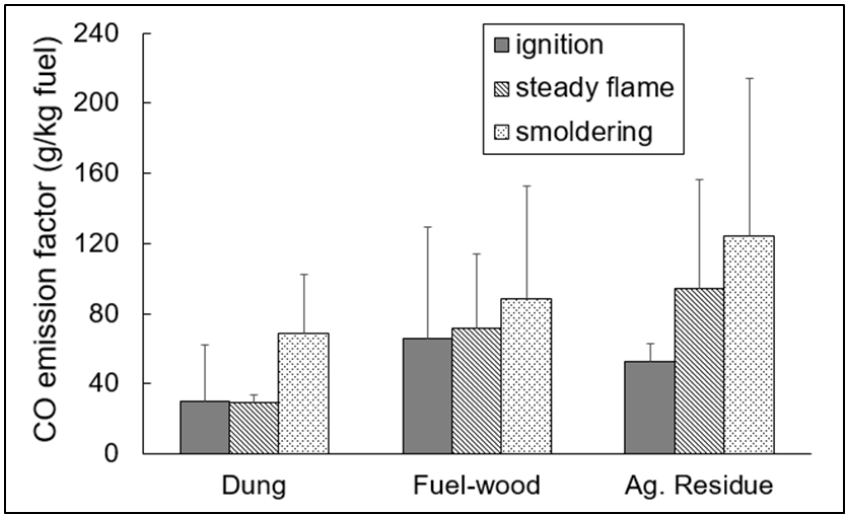

Figure 4.7: Fuel-wise average values of CO emission factors categorized by observed combustion phases. Emisssion factors are expressed in g-pollutant per kg of fuel burnt. One-sided error bars are shown to denote one standard deviation from the mean.

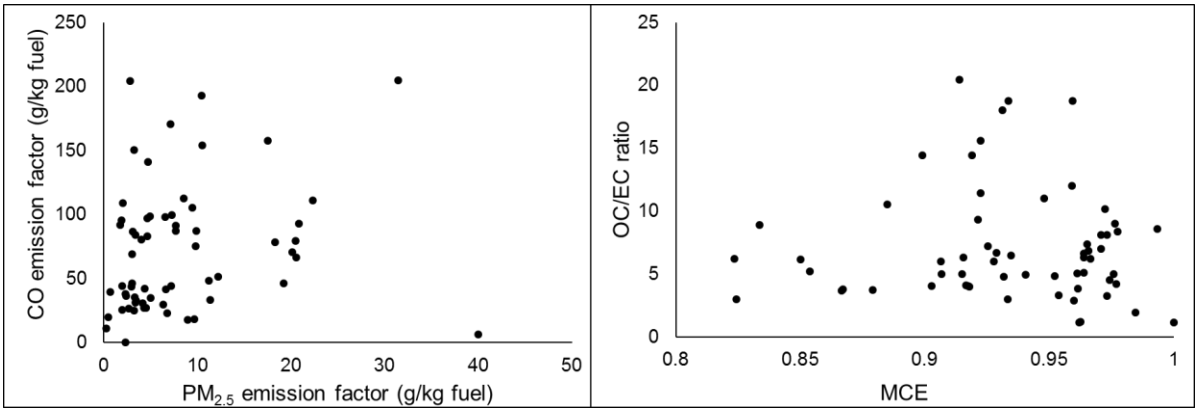

Figure 4.8: Comparisons of (a) CO vs $PM_{2.5}$, EFs and (b) OC/EC ratios vs modified combustion efficiency (MCE) values.

4.3. Average emission factors by fuel category; comparison with previous studies

Average EFs for the entire burn cycle were calculated as a time-weighted sum of EFs for each phase of combustion. Fuel-wood and agricultural residue are used predominantly in flaming conditions to carry out the bulk of cooking operations, resulting in weights of 17% ignition, 66% steady flame and 17% smoldering. For dung, the weights are 17% ignition, 17% flaming and 66% smoldering because dung was used for longer low-power operations such as heating water/milk and roasting vegetables. These EFs are compared with other reported EFs in Figure 4.9. Average fuel-wood $PM_{2.5}$ EFs and OC/EC ratios in this study are 20% larger than those reported by (Roden et al., 2006) for Honduran cookstoves, but they are 2-8 times as large as those reported for laboratory studies (Habib et al., 2008; MacCarty et al., 2008; Saud et al., 2012). For agricultural residue and dung, the average EFs and OC/EC ratios are 1.8 – 4.2 times and 1.3 – 2.2 times higher, respectively, compared to those reported by Saud et al. (2012) and Habib et al. (2008).

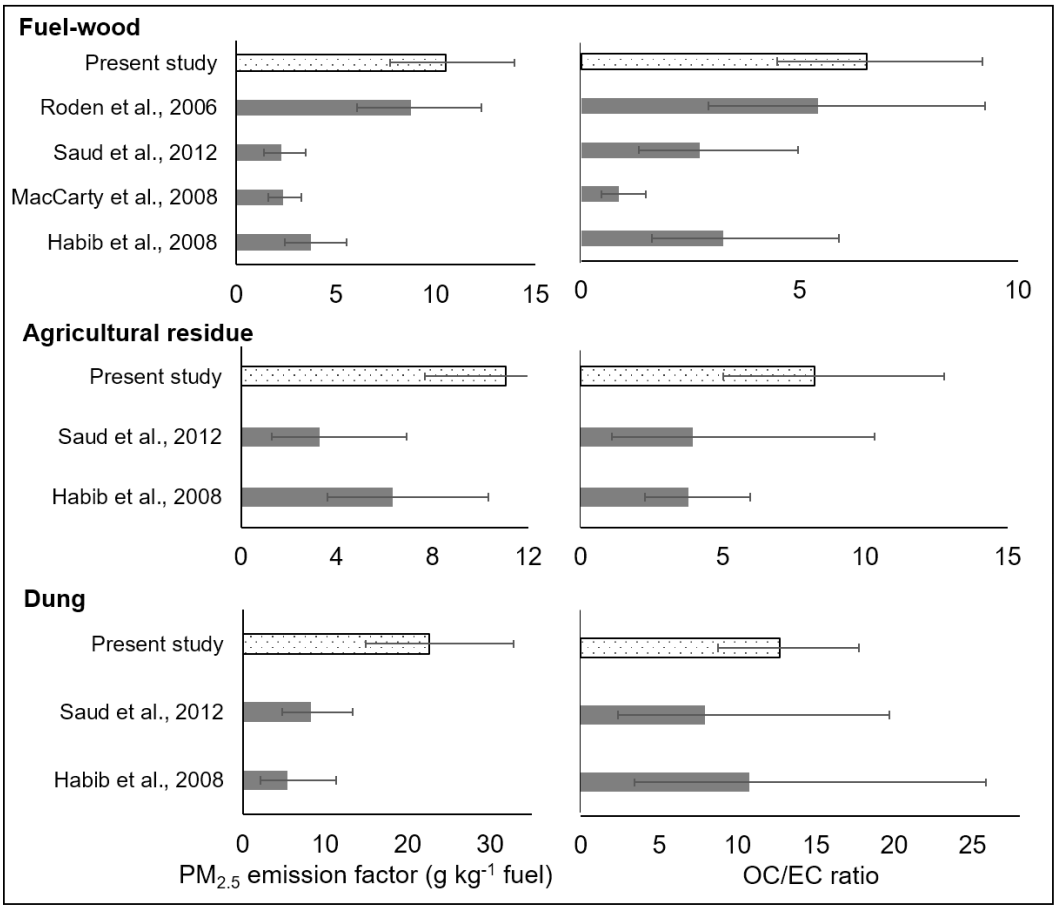

Figure 4.9: Average $PM_{2.5}$ emission factors and OC/EC ratios for the three fuel categories in this study, compared with relevant studies. Error bars for values estimated in this study denote 95% confidence intervals based on standard errors of the means. Error bars for other studies are the bounds reported within those studies.

The emission factors shown in Figure 4.9 are averages from a selection of studies that used fuels and stoves comparable to those used in our field study. A detailed list of cookstove particulate emission factors measured in laboratory and field studies, including those shown in Figure 1.9, is provided in Table 4.3. Most studies included in the following table tested South Asian stoves and fuels, with two exceptions: Roden et al. (2009) studied traditional Honduran wood burning stoves and improved cookstoves, while Johnson et al. (2008) tested Mexican *Patsari* stoves and open cooking fires. These studies are included because they provide comparisons between the field and laboratory emission behavior for the same (or similar: see Table 4.4 for details) stove and fuel-

type. Only studies that reported PM emission factors along with their EC and OC components are reported here.

Emission factors of $PM_{2.5}$, OC and EC measured during in-field cooking were all larger (unpaired, two-sided Student's *t*-test) than those from WBT based studies, at significance levels of p=0.019, 0.033 and 0.01, respectively. The corresponding effect sizes based on differences between the means, quantified by Cohen's *d*, were 0.89, 0.82 and 1, respectively. As a rule of thumb, effect sizes>0.8 are considered large. (Sawilowsky, 2009). Note that these significant differences were found even though emission factors for various fuel and stove types were combined for this analysis. On average, real-world $PM_{2.5}$, OC and EC emission factors are larger than their counterparts from simulated cooking cycles by factors of 2.1, 1.5 and 3.1, respectively. The difference between EC/OC ratios for field and WBT studies was not significant because of the effect of fuel type: emissions from dung combustion consistently have a smaller EC fraction than those from fuel-wood burning. However, we previously demonstrated lower EC/OC (larger OC/EC in Figure 4.9) from field studies than fuel-matched laboratory observations.

Table 4.3: Summary of reported mass emission factors of $PM_{2.5}$, EC and OC emissions from biomass cookstoves. All emission factors are expressed as mean (standard deviation).

Study	Test protocol	Stove	Fuel	Emission factors[a] (g kg^{-1} fuel)		
				$PM_{2.5}$	EC	OC
Habib et al. (2008)	Laboratory WBT, low burn rate	Indian traditional mud	fuel-wood	1.9 (0.8)	0.67 (0.32)	0.40 (.09)
	Laboratory WBT, high burn rate		fuel-wood	5.1 (1.4)	0.51 (0.15)	2.3 (0.3)
	Laboratory WBT		agricultural residue: woody stalks	7.5 (3.3)	0.68 (0.15)	2.9 (0.5)
			agricultural residue: rice straw	9.3 (4.1)	0.19 (0.09)	4.7 (1.1)
			dung	5.4 (2.4)	0.22 (0.10)	2.3 (0.6)
Johnson et al. (2008)	Laboratory WBT	open fire	fuel-wood	4.9 (0.8)	1.1 (0.5)	2.5 (0.4)
	Field WBT			3.7 (2.2)	1.1 (0.1)	1.8 (1.1)
	Field cooking			8.8 (3.1)	0.3 (0.1)	4.4 (1.6)
	Laboratory WBT	Mexican 'Patsari'		4.8 (1.9)	1.0 (0.5)	2.4 (0.9)
	Field WBT			2.8 (1.3)	1.0 (0.6)	2.6 (1.2)
	Field cooking			5.4 (2.3)	0.8 (0.4)	2.7 (1.1)
Roden et al. (2009)	Field cooking	Honduran traditional	fuel-wood	8.5 (1.6)	1.5 (0.3)	4 (0.9)
	Laboratory WBT	traditional three-stone		1.7 (0.1)	0.8 (0.2)	0.7 (0.1)
	Field cooking	improved, no chimney ('rocket' stove)		5.6 (0.4)	2.4 (0.5)	2.5 (0.5)
	Laboratory WBT			1.4 (0.1)	1.1 (0.2)	0.3 (0.1)
Saud et al. (2012)	Laboratory, test cycle not reported	open fire	fuel-wood	4.1 (1.2)	0.35 (0.07)	1.0 (0.3)
	Laboratory, test cycle not reported		agricultural residue	6.8 (4.1)	0.37 (0.14)	1.5 (0.7)
	Laboratory, test cycle not reported		dung	14.3 (5.3)	0.49 (0.25)	3.9 (1.1)

Pandey et al. (2017)	Field cooking	Indian traditional mud	fuel-wood	10.5 (1.4)	0.9 (0.1)	4.9 (0.8)
			agricultural residue	11.1 (2.1)	1.6 (0.5)	7 (1.6)
			dung	22.6 (5.0)	1.0 (0.5)	12.9 (4.0)
Jayarathne et al. (2018)	Laboratory WBT	Nepalese traditional mud	fuel-wood	4.9 (0.9)	0.8 (0.08)	2.5 (0.3)
	Field cooking			10.7 (1.6)	1.1 (0.1)	5.9 (0.7)
	Laboratory WBT		dung	19.7 (3.0)	0.4 (0.04)	8.5 (1.0)
	Field cooking			14.5 (2.2)	0.47 (0.06)	9.9 (1.2)
Weyant et al. (2019)	Field cooking	Indian traditional mud	fuel-wood, dung	11.9 (7.6)	0.9 (0.3)	5.6 (5.2)
		Nepalese traditional mud	fuel-wood, agricultural residue, dung	4.3 (0.8)	1.1 (0.3)	3.4 (2.1)
		Nepalese 'Terai'		6.7 (2.6)	1.7 (0.8)	2.3 (1.8)
		Nepalese improved stove, no chimney		5.8 (2.6)	0.8 (0.6)	3.3 (1.7)
		Tibetan open stove	dung	42.7 (26.0)	0.7 (0.8)	31.6 (19.8)
		Tibetan chimney stove		23.2 (12.6)	0.3 (0.1)	16.2 (10.2)
		Tibetan chimney stove	fuel-wood	12.7 (10.2)	0.9 (0.8)	8.5 (7.3)

A scatterplot of all OC and $PM_{2.5}$ emission factors from Table 4.3 is shown Figure 4.10. Over field and WBT studies, OC mass constituted approximately 60% of the total particle mass. Therefore, studies that understimate PM emission factors likely use cooking cycles characterized by more frequent strong flaming conditions (with low OC emissions) than actual cooking. This hypothesis is supported by a detailed analysis of optical measurements from field and laboratory tests (Chen

et al., 2012): lab tests predominamtly skew towards events with low SSA particles (mostly EC). On the other hand, field tests contain events dominated by low, intermediate and high SSA particles.

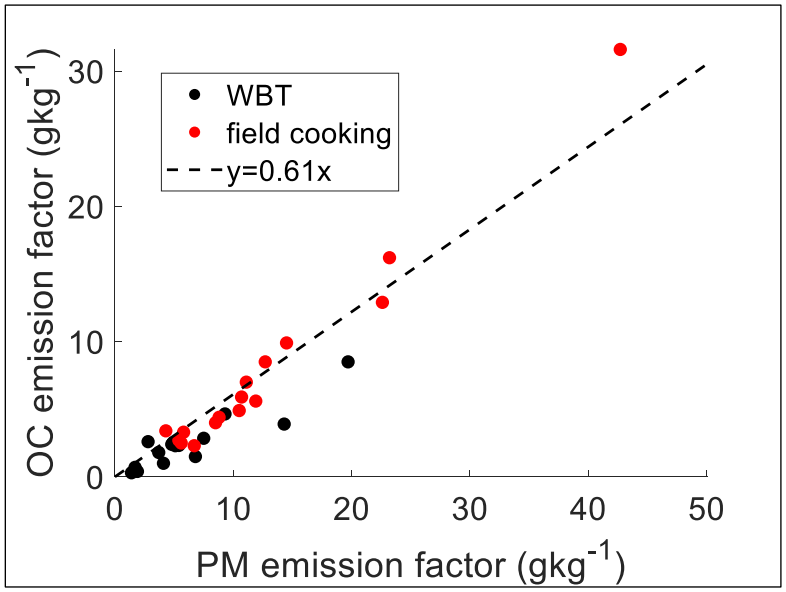

Figure 4.10: The relationship between OC and $PM_{2.5}$ emission factors from all the studies listed in Table 4.3. All WBT based measurements (lab or field) are grouped. The dashed line represents an ordinary least-squares fit (R^2=0.92)

4.4. Thermal carbon fractions from TOR analysis

Thermal fractions of total carbon constituted by the IMPROVE_A protocol are shown in Figure 4.11. OC1, OC2, OC3 and OC4 refer to carbon that evolves at temperatures of 120 ºC, 250 ºC, 450 ºC, and 550 ºC respectively, in the inert helium atmosphere. OP denotes pyrolyzed carbon, OC charring in the inert helium carrier. EC1, EC2 and EC3 fractions evolve in a 2%O_2/98%He oxidizing atmosphere at 550 ºC, 700 ºC and 800 ºC, respectively. Figure 4.11 compares fractions from this study with those reported for controlled biomass (hardwood and softwood) burning reported in Chow et al. (2007a). We also compare our results with a source profile developed for $PM_{2.5}$ emissions from wood *chulhas*, as part of source apportionment studies conducted by the

Central Pollution Control Board (CPCB) of India (CPCB (2011)). This profile was based on laboratory burns, but details of the test fuel and burn protocol are not known. OC3 was the most abundant fraction, ~50% of the total carbon mass, while the profiles in literature ranged 10%-34% in the OC3 fraction. The OC1 fraction for all fuels in this study was uniformly less than 3%, a finding comparable only to the 5% OC1 reported for softwood, but not for the other two profiles. Carbonaceous aerosol source profiles are useful for source apportionment, and they may also have implications for climate and health impact assessments. In an previous study (Pandey et al., 2016), we reported that light absorbing OC may play a larger role in light absorption by cookstove emissions than that from earlier work on biomass burning in the U.S.A. The difference in constituents of OC emissions from the two sources might contribute to the observed difference in their optical characteristics, since thermal stability is known to be inversely related to the light absorption efficiency of organic compounds (Andreae and Gelencsér, 2006; Saleh et al., 2013).

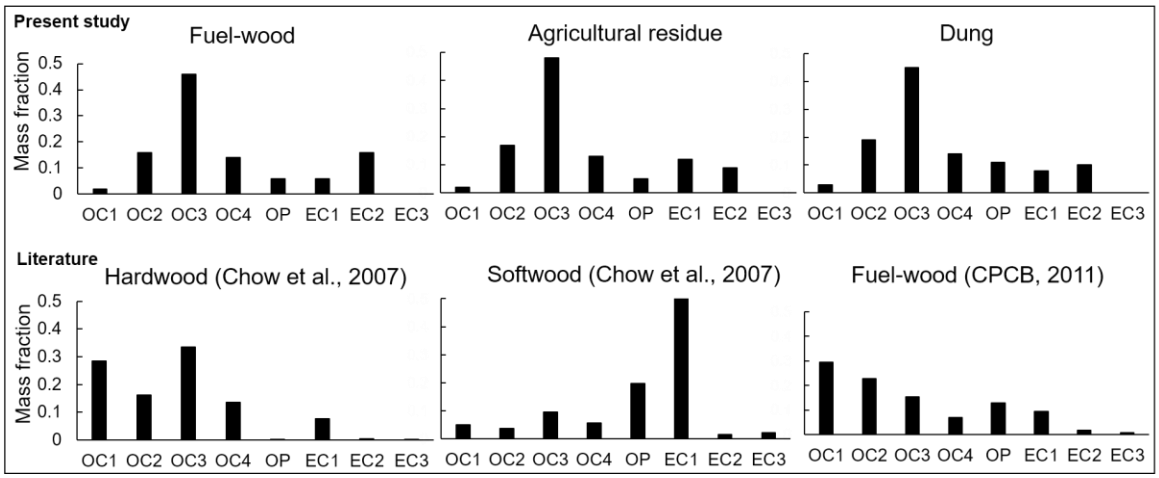

Figure 4.11: Fraction of total carbon emissions contributed by the IMPROVE_A thermal carbon fractions.

4.5. Insights from real-time measurements

A sample plot of real-time particle and gas concentration profiles from day 9 of the study is shown in Figure 4.12. It should be noted that the Sidepak instrument does not measure actual particle

mass concentration, but instead measures light scattering at 670 nm wavelength and provides an equivalent concentration of Arizona Test Dust that would produce the same magnitude of light scattering.

Over a period of two hours, Sidepak PM measurements and CO concentration (solid in panel B) fluctuated every few minutes. Sidepak was saturated at an equivalent concentration of 20 µg/m3, giving the appearance of a steady state. Re-fueling was typically followed by a sudden spike in particulate and CO emissions. Ignition with 'dirty' fuels like dung, straws and kerosene as well as re-fueling or rekindling (per the cook's convenience) are critical features of a realistic cooking cycle. Carefully maintained steady burn conditions in laboratory tests reduce the emission variability and may be the major cause of the low bias in WBT emission factors (Roden et al., 2009).

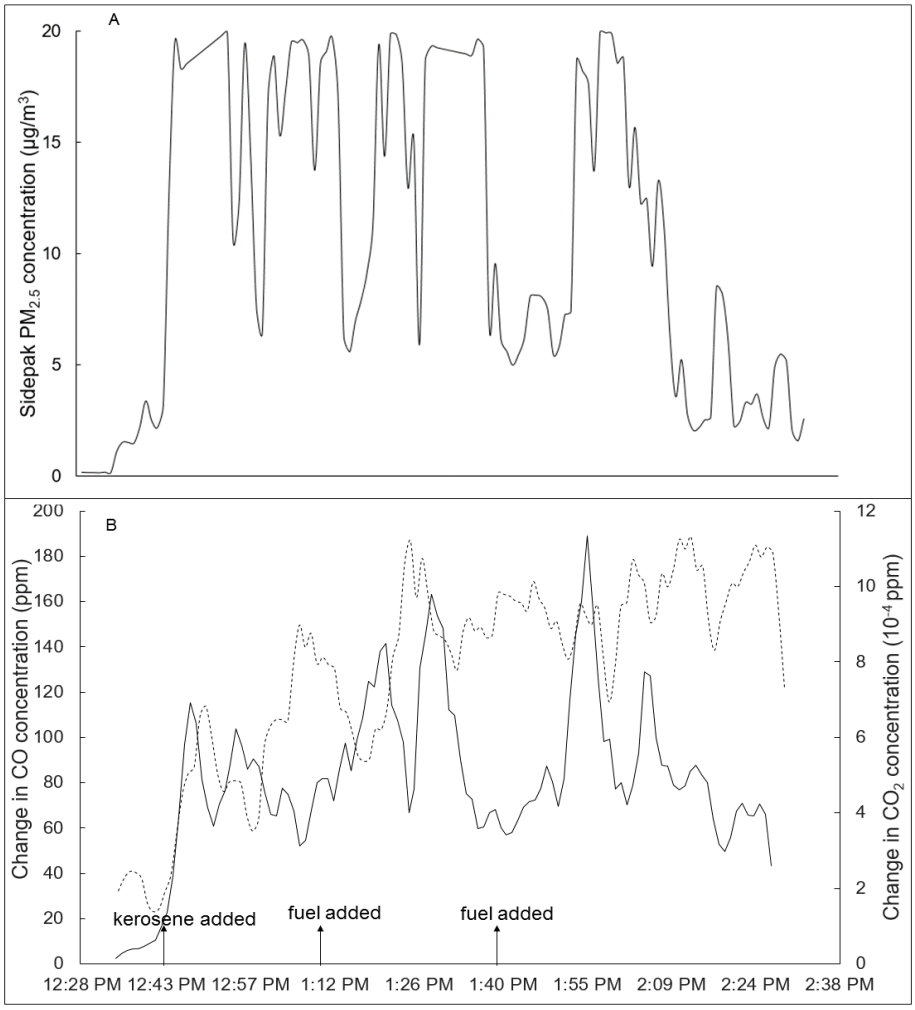

Figure 4.12: Real-time measurements of (A) Sidepak $PM_{2.5}$ mass concentrations in µg/m^3, and (B) CO concentrations (solid) in and CO_2 concentration (dashed), both in ppm.

4.6. Inventoried emissions for biomass cookstoves in India

The global harmonized emissions database EDGAR-HTAP (a globally consistent inventory that combines the Emissions Database for Global Atmospheric Research and Hemispheric Transport of Air Pollution inventories) provides model-ready emissions inputs (Janssens-Maenhout et al., 2012). Emissions for South Asia in this dataset were taken from the Regional Emission inventory in ASia (REAS), with annual estimates of $PM_{2.5}$, BC and OC emissions for the domestic sector

(base year 2008) = 2467, 371 and 1700 Tg y^{-1}, respectively (Kurokawa et al., 2013). Top-down fuel consumption estimates based on an energy balances dataset from the International Energy Agency were used in that study. A detailed, bottom-up national inventory (Speciated Multi-pOllutant Generator or SMOG) estimated residential $PM_{2.5}$, BC and OC emissions as 2803, 546 and 1035 Tg y^{-1}, respectively, for the year 2015 (Pandey et al., 2014). This includes emissions from household cooking and kerosene-based lighting, with cookstoves contributing 92%, 60% and 100%, respectively, of the total residential $PM_{2.5}$, BC and OC emissions. Ratios of fuel-wise cookstove PM emission factors from our field study to those in the SMOG inventory (an average of best available values published till date) ranged 2.2-2.5, those for OC emission factors ranged 2.5-4.2. Using our field-based emission factors with the fuel use estimates from Pandey et al., 2014, I calculated annual cookstove emitted $PM_{2.5}$, BC and OC as 5694, 442 and 3023 Tg y^{-1}, respectively.

References

Andreae, M. and Gelencsér, A.: Black carbon or brown carbon? The nature of light-absorbing carbonaceous aerosols, Atmos. Chem. Phys., 6, 3131-3148, 2006.

Bond, T. C., Doherty, S. J., Fahey, D., Forster, P., Berntsen, T., DeAngelo, B., Flanner, M., Ghan, S., Kärcher, B., and Koch, D.: Bounding the role of black carbon in the climate system: A scientific assessment, J. Geophys. Res.: Atmos., 118, 5380-5552, 2013.

Bond, T. C., Streets, D. G., Yarber, K. F., Nelson, S. M., Woo, J. H., and Klimont, Z.: A technology-based global inventory of black and organic carbon emissions from combustion, J. Geophys. Res.: Atmos., 109, 2004.

Census: Houselisting and Housing Census Data Office of The Registrar General and Census Commissioner, M. o. H. A., Goverment of India. (Ed.), New Delhi., 2011.

Chen, Y., Roden, C. A., and Bond, T. C.: Characterizing biofuel combustion with patterns of real-time emission data (PaRTED), Environ. Sci. Technol., 46, 6110-6117, 2012.

Chow, J., Watson, J., Lowenthal, D., Chen, L., Zielinska, B., Mazzoleni, L., and Magliano, K.: Evaluation of organic markers for chemical mass balance source apportionment at the Fresno Supersite, Atmospheric Chemistry and Physics, 7, 1741-1754, 2007a.

Chow, J. C., Watson, J. G., Chen, L.-W. A., Chang, M. O., Robinson, N. F., Trimble, D., and Kohl, S.: The IMPROVE_A temperature protocol for thermal/optical carbon analysis: maintaining consistency with a long-term database, Journal of the Air & Waste Management Association, 57, 1014-1023, 2007b.

Chow, J. C., Watson, J. G., Robles, J., Wang, X. L., Chen, L.-W. A., Trimble, D. L., Kohl, S. D., Tropp, R. J., and Fung, K. K.: Quality assurance and quality control for thermal/optical analysis of aerosol samples for organic and elemental carbon, Analytical and Bioanalytical Chemistry, 401, 3141-3152, 2011.

CPCB: Air quality monitoring, emission inventory and source apportionment study for Indian cities. National Summary Report, Central Pollution Control Board, 2011.

Grieshop, A. P., Marshall, J. D., and Kandlikar, M.: Health and climate benefits of cookstove replacement options, Energy Policy, 39, 7530-7542, 2011.

Guttikunda, S. K. and Calori, G.: A GIS based emissions inventory at 1 km× 1 km spatial resolution for air pollution analysis in Delhi, India, Atmospheric Environment, 67, 101-111, 2013.

Habib, G., Venkataraman, C., Bond, T. C., and Schauer, J. J.: Chemical, microphysical and optical properties of primary particles from the combustion of biomass fuels, Environ. Sci. Technol., 42, 8829-8834, 2008.

Janssens-Maenhout, G., Dentener, F., Van Aardenne, J., Monni, S., Pagliari, V., Orlandini, L., Klimont, Z., Kurokawa, J.-i., Akimoto, H., and Ohara, T.: EDGAR-HTAP: a harmonized gridded air pollution emission dataset based on national inventories, European Commission Publications Office, Ispra (Italy). JRC68434, EUR report No EUR, 25, 299-2012, 2012.

Johnson, M., Edwards, R., Frenk, C. A., and Masera, O.: In-field greenhouse gas emissions from cookstoves in rural Mexican households, Atmos. Environ., 42, 1206-1222, 2008.

Kulkarni, P., Qi, C. L., and Fukushima, N.: Development of portable aerosol mobility spectrometer for personal and mobile aerosol measurement, Aerosol Sci. Technol., 50, 1167-1179, 2016.

Kurokawa, J., Ohara, T., Morikawa, T., Hanayama, S., Janssens-Maenhout, G., Fukui, T., Kawashima, K., and Akimoto, H.: Emissions of air pollutants and greenhouse gases over Asian regions during 2000–2008: Regional Emission inventory in ASia (REAS) version 2, Atmos. Chem. Phys., 13, 11019-11058, 2013.

Leavey, A., Londeree, J., Priyadarshini, P., Puppala, J., Schechtman, K. B., Yadama, G., and Biswas, P.: Real-time particulate and CO concentrations from cookstoves in rural households in Udaipur, India, Environmental science & technology, 49, 7423-7431, 2015.

MacCarty, N., Ogle, D., Still, D., Bond, T., and Roden, C.: A laboratory comparison of the global warming impact of five major types of biomass cooking stoves, Energy for sustainable development, 12, 56-65, 2008.

MHFW, N. D.: Report of the Steering Committee on Air Pollution and Health-Related Issues., Ministry of Health and Family Welfare, Government of India, New Delhi, 2015.

O'Shaughnessy, P. T. and Slagley, J. M.: Photometer response determination based on aerosol physical characteristics, AIHA Journal, 63, 578-585, 2002.

Pandey, A., Patel, S., Pervez, S., Tiwari, S., Yadama, G., Chow, J. C., Watson, J. G., Biswas, P., and Chakrabarty, R. K.: Aerosol emissions factors from traditional biomass cookstoves in India: insights from field measurements, Atmos. Chem. Phys., 17, 13721-13729, 2017.

Pandey, A., Pervez, S., and Chakrabarty, R. K.: Filter-based measurements of UV–vis mass absorption cross sections of organic carbon aerosol from residential biomass combustion: Preliminary findings and sources of uncertainty, J. Quant. Spectrosc. Radiat. Transfer, 182, 296-304, 2016.

Pandey, A., Sadavarte, P., Rao, A. B., and Venkataraman, C.: Trends in multi-pollutant emissions from a technology-linked inventory for India: II. Residential, agricultural and informal industry sectors, Atmos. Environ., 99, 341-352, 2014.

Patel, S., Li, J., Pandey, A., Pervez, S., Chakrabarty, R. K., and Biswas, P.: Spatio-temporal measurement of indoor particulate matter concentrations using a wireless network of low-cost sensors in households using solid fuels, Environ. Res., 152, 59-65, 2017.

Reid, J., Koppmann, R., Eck, T., and Eleuterio, D.: A review of biomass burning emissions part II: intensive physical properties of biomass burning particles, Atmospheric Chemistry and Physics, 5, 799-825, 2005.

Roden, C. A., Bond, T. C., Conway, S., and Pinel, A. B. O.: Emission factors and real-time optical properties of particles emitted from traditional wood burning cookstoves, Environ. Sci. Technol., 40, 6750-6757, 2006.

Roden, C. A., Bond, T. C., Conway, S., Pinel, A. B. O., MacCarty, N., and Still, D.: Laboratory and field investigations of particulate and carbon monoxide emissions from traditional and improved cookstoves, Atmos. Environ., 43, 1170-1181, 2009.

Sadavarte, P., Venkataraman, C., Cherian, R., Patil, N., Madhavan, B., Gupta, T., Kulkarni, S., Carmichael, G., and Adhikary, B.: Seasonal differences in aerosol abundance and radiative forcing in months of contrasting emissions and rainfall over northern South Asia, Atmospheric Environment, 125, 512-523, 2016.

Sagar, A., Balakrishnan, K., Guttikunda, S., Roychowdhury, A., and Smith, K. R.: India leads the way: a health-centered strategy for air pollution, Environ. Health Perspect., 124, A116, 2016.

Sahu, M., Peipert, J., Singhal, V., Yadama, G. N., and Biswas, P.: Evaluation of mass and surface area concentration of particle emissions and development of emissions indices for cookstoves in rural India, Environmental science & technology, 45, 2428-2434, 2011.

Saleh, R., Hennigan, C., McMeeking, G., Chuang, W., Robinson, E., Coe, H., Donahue, N., and Robinson, A.: Absorptivity of brown carbon in fresh and photo-chemically aged biomass-burning emissions, Atmos. Chem. Phys., 13, 7683-7693, 2013.

Saud, T., Gautam, R., Mandal, T., Gadi, R., Singh, D., Sharma, S., Dahiya, M., and Saxena, M.: Emission estimates of organic and elemental carbon from household biomass fuel used over the Indo-Gangetic Plain (IGP), India, Atmos. Environ., 61, 212-220, 2012.

Sawilowsky, S. S.: New effect size rules of thumb, 2009. 2009.

Schulz, M., Textor, C., Kinne, S., Balkanski, Y., Bauer, S., Berntsen, T., Berglen, T., Boucher, O., Dentener, F., and Guibert, S.: Radiative forcing by aerosols as derived from the AeroCom present-day and pre-industrial simulations, Atmospheric Chemistry and Physics, 6, 5225-5246, 2006.

Shindell, D., Kuylenstierna, J. C., Vignati, E., van Dingenen, R., Amann, M., Klimont, Z., Anenberg, S. C., Muller, N., Janssens-Maenhout, G., and Raes, F.: Simultaneously mitigating near-term climate change and improving human health and food security, Science, 335, 183-189, 2012.

Smith, K.: You don't get what you expect; you get what you inspect, Energy for Sustainable Development, 11, 3-4, 2007.

Smith, K. R., Uma, R., Kishore, V., Lata, K., Joshi, V., Zhang, J., Rasmussen, R., Khalil, M., and Thorneloe, S.: Greenhouse gases from small-scale combustion devices in developing countries, Phase IIa: Household Stoves in India, US Environmental Protection Agency, Research Triangle Park, NC, 2000. 98, 2000.

Solomon, P. A., Crumpler, D., Flanagan, J. B., Jayanty, R., Rickman, E. E., and McDade, C. E.: US National PM2. 5 chemical speciation monitoring networks—CSN and IMPROVE: description of networks, Journal of the Air & Waste Management Association, 64, 1410-1438, 2014.

Venkataraman, C., Sagar, A., Habib, G., Lam, N., and Smith, K.: The Indian national initiative for advanced biomass cookstoves: the benefits of clean combustion, Energy for Sustainable Development, 14, 63-72, 2010.

Wang, X. L., Watson, J. G., Chow, J. C., Gronstal, S., and Kohl, S. D.: An efficient multipollutant system for measuring real-world emissions from stationary and mobile sources, Aerosol Air Qual. Res., 12, 145-160, 2012.

Zhang, H., Ye, X., Cheng, T., Chen, J., Yang, X., Wang, L., and Zhang, R.: A laboratory study of agricultural crop residue combustion in China: emission factors and emission inventory, Atmospheric Environment, 42, 8432-8441, 2008.

Zhu, K., Zhang, J. F., and Lioy, P. J.: Evaluation and comparison of continuous fine particulate matter monitors for measurement of ambient aerosols, J. Air Waste Manage. Assoc., 57, 1499-1506, 2007.

Chapter 5: Estimating aerosol-phase light absorption from filter-based optics

Common filter-based optical instruments like the Particle Soot Absorption Photometer (PSAP), the aethalometer or the Tricolor Absorption Photometer (TAP) estimate particle light absorption based on semi-continuous transmission measurements through a sample spot on the filter medium. The measured optical coefficient (σ_{meas}) is given by:

$$\sigma_{meas} = \frac{A}{Q\Delta t} \times ATN_t = \frac{A}{Q\Delta t} \ln\left(\frac{T_{t-\Delta t}}{T_t}\right) \quad (5.1)$$

where A is the area of the sample spot, Q is the sample flow-rate through the filter during a time interval Δt, ATN_t is the Beer-Lambert attenuation through the filter and $T_{t-\Delta t}$ and T_t are the transmission ratios measured at the start and the end of the interval, respectively. Transmission ratios are measured by comparing transmitted intensity ($I(t)$) through the sample spot to that through a reference sport ($I_0(t)$), normalized to the same ratio calculated for an unloaded filter:

$$T_t = \frac{I(t)/I_0(t)}{I(0)/I_0(0)} \quad \backslash (5.2)$$

If the transmitted intensity depended only on particle light absorption and attenuation could be calculated using the Beer-Lambert law (as shown in equation 5.1), then σ_{meas} would be equal to the particle absorption coefficient (σ_{ap}). In general, optical depth measures for a filter sample are correlated to particulate phase absorption optical depth $\tau_{a,p}$ of the sampled particles, but not equal to it. This absorption optical depth is related to σ_{ap} as attenuation is related to the attenuation coefficient:

$$\tau_{a,p} = \sigma_{ap} \times \frac{Q\Delta t}{A} \neq ATN \quad (5.3)$$

The inequality arises because filter media are multiple-scattering, leading to a larger optical path length than when particles are in their suspended, single-scattering state. This causes the appearance of enhanced light absorption (Clarke, 1982; Bond et al., 1999; Gorbunov et al., 2002), and is referred to the as the multiple scattering artifact. While the multiple-scattering effect is typically treated as a function of only the filter medium, loading of absorbing aerosols can diminish its effect, inducing an aerosol dependent loading artifact (Weingartner et al., 2003; Arnott et al., 2005; Virkkula et al., 2005; Virkkula, 2010). Aerosol light scattering could enhance multiple scattering which leads to an overestimation of absorption (Weingartner et al., 2003; Lack et al., 2008), implying that filter-based measurements are also sensitive to the particle absorption coefficient (σ_{sp}). Further, the particle size distribution can affect the penetration of aerosols into the filter medium and their backscattering and therefore, the measured transmittance. Therefore, any filter optical measure is a function of the aerosol phase absorption ($\tau_{a,p}$) and scattering ($\tau_{s,p} = \sigma_{sp} \times \frac{Q\Delta t}{A}$) optical depths and particle size distribution. A theoretical treatment of these artifacts using the two-stream approximation provides insight about the interaction of filter and particle optical characteristics, but several parameters required by the model are difficult to measure. Typically, filter artifacts have been evaluated for commonly used instruments, by comparing their measurements with contact-free aerosol light absorption measurements or using reference materials with known optical properties.

5.1. Filter artifact correction literature

Bond et al. (1999) formulated measured PSAP extinction coefficients as a combination of particle-phase absorption (σ_{ap}) and scattering (σ_{sp}) coefficients:

$$\sigma_{PSAP} = K_1\sigma_{sp} + K_2\sigma_{ap} \quad (5.4)$$

where σ_{PSAP} is the value reported by the instrument after applying an empirical correction (for loading-artifacts) determined by the manufacturer, further corrected by Bond et al. (1999) for flow-rate and spot size:

$$\sigma_{PSAP} = \sigma_{meas} \times \frac{1}{1.2369 \times T_t + 0.8135} \quad (5.5)$$

This study investigated the validity of the manufacturer's correction by directly measuring σ_{PSAP} and σ_{sp} (via a nephelometer) and inferring σ_{ap} as the difference of *in-situ* extinction (via an optical extinction cell) and scattering for pure nigrosine and ammonium sulphate aerosols, as well as mixtures of the two aerosol types in varying proportions. Coefficients K_1 and K_2 were then estimated as 0.02 and 1.22, respectively, yielding:

$$\sigma_{ap} = \frac{\sigma_{PSAP} - 0.02\sigma_{sp}}{1.22} \quad (5.6)$$

Virkkula (2010) and Virkkula et al. (2005) performed a similar empirical calibration for the PSAP, with the addition of a photoacoustic spectrometer to measure particle-phase light absorption, for diesel soot, kerosene soot, graphite, ammonium sulphate and polystyrene latex aerosols. The authors used the form of the correction equation proposed by (Bond et al., 1999):

$$\sigma_{ap} = \frac{\sigma_{meas} \times g(T_t) - K_1\sigma_{sp}}{K_2} = \sigma_{meas} \times f(T_t) - s\sigma_{sp} \quad (5.7)$$

For the aerosol types investigated in this study, a good fit for f was found to be a logarithmic function of the loading T_t, with an additional dependence on the particle-phase SSA (ω_p):

$$f(T_t, \omega_p) = k_0 + k_1(h_0 + h_1\omega_p)\ln(T_t) \quad (5.8)$$

The constants k_0, k_1, h_0, h_1 and s were determined for three wavelengths.

Arnott et al. (2005) used the two-layer, two-stream radiative model of filter optics discussed above to derive an approximate function form of a loading correction function for the aethalometer:

$$\sigma_{ap}(t+\Delta t) = \frac{\sigma_{meas} - \alpha\sigma_{sp}}{M}\sqrt{1 + \frac{\frac{Q\Delta t}{A}\sigma_{ap}(t)}{\chi\tau_{a,f}}} \quad (5.9)$$

where Δt is the measurement interval. The quantities α, M and $\chi\tau_{a,f}$ were empirically determined using simultaneous aethalometer, photoacoustic spectrometer and nephelometer measurements on kerosene soot and ammonium sulphate aerosols. Equation 5.9 captures the incremental change in loading from measurement to measurement following each filter change (at the time of filter change, t=0).

Müller et al. (2014) used previous empirical corrections for the PSAP (equations 5.6-5.8) to initialize a two-stream filter radiative model (detailed model description in Chapter 5.2 and Appendix A1) to develop an experimentally constrained description of filter optical behavior (henceforth, the CTS method). Instead of the flow-rate and sampling time dependent optical coefficients, they employ 'relative optical depths' or attenuation (*ATN*) optical depth measurements:

$$ATN^{meas} = \ln\left(\frac{T_{t-\Delta t}}{T_t}\right) \quad (5.10)$$

Attenuation optical depths were also derived from the model (τ^{mod}) (see equations 5.14A and 5.14B in Chapter 5.2). With reasonable assumptions for parameters that cannot be directly observed for each sample, τ^{mod} can be computed for any input values of $\tau_{a,p}$, $\tau_{s,p}$ and g_p.

Sensitivity of the relative optical depths to pure black and white particles were defined as:

$$F_a^{meas/mod}(\tau_{a,p}) = \frac{ATN^{meas/mod}(\tau_{a,p},\tau_{s,p}=0)}{\tau_{a,p}} \quad (5.11A)$$

$$F_s^{meas/mod}(\tau_{s,p}) = \frac{ATN^{meas/mod}(\tau_{a,p}=0,\tau_{s,p})}{\tau_{s,p}} \quad (5.11B)$$

These sensitivities can be readily calculated from the model, but they need to be constrained by experimental observations. F_a^{meas} was calculated by reformulating the correction equations (expressing them in terms of $\tau_{a,p}$ and τ^{meas}) reported by Virkkula (2010) and Bond et al. (1999) for black soot particles. F_s^{meas} was derived by measuring the response of the PSAP to white NaCl particles generated in the laboratory and fitting a curve to the observed relationship. Then the attenuation optical depth was constrained by matching measured and modeled depths for black and white particles:

$$ATN^{meas}(\tau_{a,p}, \tau_{s,p}, g_p) = \frac{F_a^{meas}\tau_{a,p} + F_s^{meas}\tau_{s,p}}{F_a^{mod}\tau_{a,p} + F_s^{mod}\tau_{s,p}} \times ATN^{mod}(\tau_{a,p}, \tau_{s,p}, g_p) \quad (5.12)$$

Equation 5.10 can be iteratively solved to find a value of $\tau_{a,p}$ that minimizes the difference between the measured relative optical depth and the right hand side of the equation.

The studies discussed here relied on empirical scattering response functions determined from measurements on inorganic white aerosols. The validity of these schemes for organic aerosols (pure scattering as well as light absorbing) has not been evaluated. Scanning electron microscopy images of filters loaded with particles emitted smoldering biomass have shown that liquid-like organic aerosols can coat filter fibers (Subramanian et al., 2007). This creates biases in filter measurements that are not accounted for by existing correction schemes (Weingartner et al., 2003; Cappa et al., 2008; Lack et al., 2008). These biases were proportional to organic mass loading for laboratory-generated (Cappa et al., 2008) and ambient urban aerosols (Lack et al., 2008); in both cases, the organic aerosols were non light absorbing. Davies et al. (2019) evaluated the ratio of TAP absorption coefficients to *in-situ* photoacoustic spectrometer (PAS) absorption coefficients for different ambient aerosol. TAP measurements corrected using the Bond et al. (1999) scheme

showed large deviations from the PAS data for all aerosol types (urban, fresh biomass burning and aged biomass burning) examined. The application of the CTS correction technique (Müller et al., 2014) lowered the bias in TAP measurements on urban and fresh biomass burning aerosols but resulted in increased variability in the measurements on aged biomass burning aerosols. This analysis underscored that filter-based absorption estimates are strongly influenced by aerosol type. Given that (1) organic aerosols exhibit diverse physical and optical properties and (2) these properties are correlated with combustion phase (Subramanian et al., 2007; Chakrabarty et al., 2010; Chen and Bond, 2010; Saleh et al., 2013; Saleh et al., 2014), experimental evaluations of systematic errors in filter-based absorption estimation are needed for aerosols generated from a representative range of combustion conditions.

5.2. Significance of Teflon filter samples

The instruments discussed above measure transmittance semi-continuously through a filter sample. Standalone ultraviolet-visible (UV-vis) spectrophotometers allow both transmittance and reflectance measurements as post sampling analysis of filters. These measurements can be taken with the front (sample side) or the back (clean side) of the filter facing the incident radiation. Measures of filter optical depth can then be defined using these discrete measurements.

In many field settings, aerosol samples are collected on polytetrafluoroethylene (PTFE) membrane filters (commonly known as Teflon filters) for inferring ambient or near-source particulate mass concentrations using gravimetric analysis (Koistinen et al., 1999). Major aerosol monitoring networks, such as the Interagency Monitoring of PROtected Visual Environments (IMPROVE) network (Chow et al., 2010; Solomon et al., 2014), the Chemical Speciation Network (CSN) (Solomon et al., 2014) and the Surface PARTiculate mAtter Network (SPARTAN) (Snider et al.,

2015), collect particle samples on Teflon filters for gravimetric and elemental measurements. PTFE filters are chemically inert and unlike quartz fiber filters, present a very low surface area for organic vapor adsorption (Kirchstetter et al., 2001; Vecchi et al., 2014). Correction schemes developed for instruments that use fiber filters (like the PSAP and aethalometer) cannot be applied to transmittance and/or reflectance measurements on PTFE filters. A previous study on the artifacts associated with this filter type used a reference material and provided a constant multiple scattering correction factor for optical loadings smaller than a certain threshold (Zhong and Jang, 2011). Another recent study (White et al., 2016) proposed a theory-based model to calibrate attenuation measurements for Teflon filter samples and applied this new model to a historical dataset from IMPROVE network. They found that the reevaluated absorption values for the PTFE samples were well-correlated with thermo-optical elemental carbon (EC) measurements for co-located quartz fiber filters.

In this work, we generated carbonaceous aerosols with varying physicochemical properties from the combustion of biomass fuels and kerosene. Kerosene combustion was used as a surrogate for fossil fuel burning, which is linked with soot or EC emissions (Andreae and Gelencsér, 2006; Bond et al., 2013). The combustion of wildland- and fuel-biomass is implicated in emissions of EC as well as light absorbing organic carbon (LAOC) (Andreae and Gelencsér, 2006; Chakrabarty et al., 2010; Chen and Bond, 2010). EC is known to absorb light throughout the visible and ultraviolet (UV) wavelengths, while LAOC absorbs preferentially in the near-UV and UV regions (Kirchstetter et al., 2004; Andreae and Gelencsér, 2006; Bond and Bergstrom, 2006; Sun et al., 2007). Therefore, we measured *in-situ* and contact-free aerosol light absorption and scattering coefficients using integrated photoacoustic-nephelometer (IPN) spectrometers operated at three wavelengths - 375, 405 and 532 nm. Co-located with these measurements was a sampling system

to collect particles onto Teflon membrane filters. Subsequent filter optical measurements, using a Lambda-35 UV-vis spectrophotometer, were performed. Observed empirical relationships between particle light absorption and filter optical depth measures were established in conjunction with predictions from a one-dimensional (1-D) two-stream radiation transfer model.

5.3. Two-stream radiative transfer model of a filter-particle system

A 1-D two-stream radiative transfer framework for multiple scattering in absorbing media was developed in Bohren (1987)–widely known as the Kubelka-Munk theory (Kubelka, 1948)–and subsequently discussed in relation to aerosol-filter systems in several studies (Clarke, 1982; Gorbunov et al., 2002; Petzold and Schönlinner, 2004; Arnott et al., 2005).

Consider the layer of filter in which sampled particles are embedded to be a one-dimensional uniform medium with an optical thickness τ_0, a single scattering albedo $\omega<1$ and a scattering asymmetry parameter g (Figure 5.1). Now, consider a 'forward' direction: at any point in the medium the energy intensity propagating in this direction is given by I_f. Conversely, the backward propagation intensity is I_b.

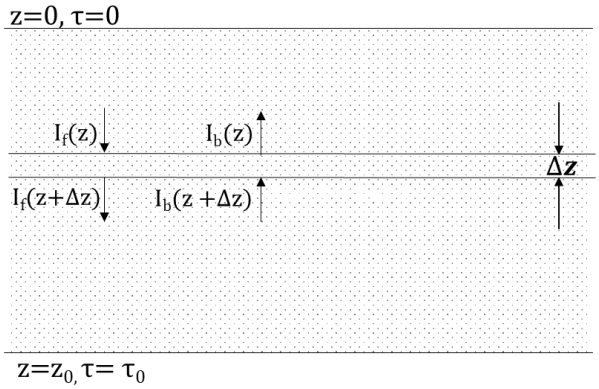

Figure 5.1: Transmission and reflection of radiation through a one-dimensional, uniformly multiple-scattering medium.

Energy conservation in the medium can be written as (Bohren, 1987):

$$\frac{d(I_f - I_b)}{d\tau} = -(1-\omega_0)(I_f + I_b) \quad (5.13A)$$

$$\frac{d(I_f + I_b)}{d\tau} = -(1-\omega_0 g))(I_f - I_b) \quad (5.13B)$$

The solution of these radiation balance equations for an aerosol-laden filter medium yields the following expressions for transmittance (T_l) and reflectance (R_l), respectively (see Appendix A1 for details):

$$T_l = \frac{2}{[2K - \omega_l(1-g_l)\,sinh(K\tau_{e,l}) + 2\,K\,cosh(K\tau_{e,l})]} \quad (5.14A)$$

$$R_l = \frac{\omega_l(1-g_l)\,sinh(K\tau_{e,l})}{[2K - \omega_l(1-g_l)\,sinh(K\tau_{e,l}) + 2\,K\,cosh(K\tau_{e,l})]} \quad (5.15B)$$

Here, ω_l, g_l and $\tau_{e,l}$ denote the SSA, asymmetry parameter and extinction optical depth, respectively, of the composite layer. A schematic representation of the two-layer system–the aerosol laden layer with properties T_l and R_l and a clean filter layer with properties T_f and R_f–is shown in Figure 5.2. The parameter K is defined as:

$$K = \sqrt{(1-\omega_l)(1-g_l\omega_l)} \quad (5.16)$$

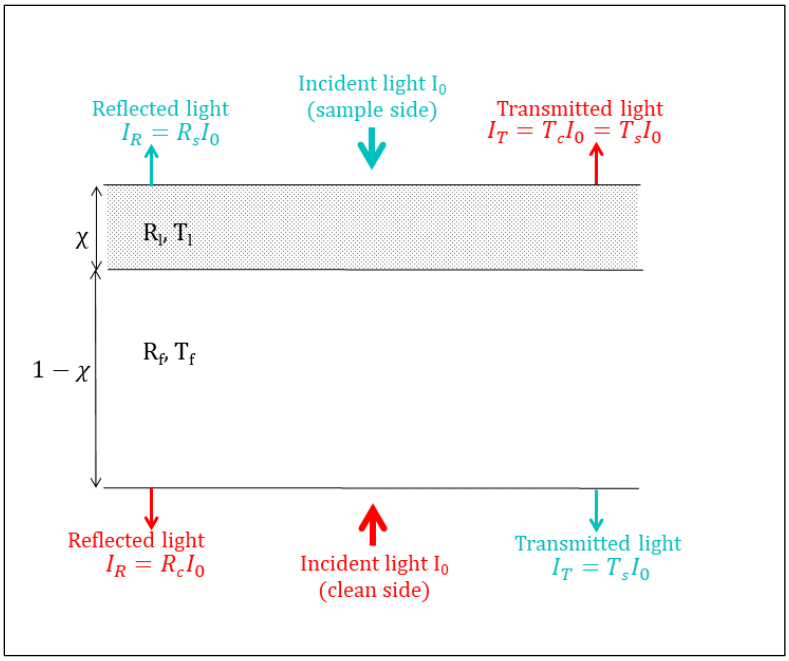

Figure 5.2: Two-layer model of a filter sample consisting of an aerosol laden layer 'l' and a clean layer 'f'.

Arnott et al. (2005) used the above model to derive the form for an approximate correction factor for the aethalometer. The aethalometer uses optically-thick quartz fiber filters, which are strongly multiple scattering, transmitting only ~10% of light in the visible wavelengths. A mathematical consequence of strong multiple scattering is that the term $K\tau_{e,l}$ is much greater than unity and equations 5.14A and 5.14B can be replaced by simplified approximations. In contrast, the Teflon filters used in this study are optically thin and constitute a weak multiple scattering medium: they transmit 70-80% of incident visible light. Therefore, the full equations for T_l and R_l were solved for the filter-particle system, using a range of plausible values of dimensionless aerosol optical properties: absorption optical depth ($\tau_{a,s}$) and SSA. Two other required inputs could not be measured: the penetration depth of aerosols into the filter was assumed to be 10% of the total filter thickness, and the asymmetry parameter of the aerosols was fixed at 0.6, based on the typical values reported for biomass burning emissions (Martins et al., 1998; Reid et al., 2005).

Transmittance and reflectance (T_s and R_s, respectively) through the filter, when light is first incident on the aerosol-laden layer(or 'sample-side') is given by (Gorbunov et al., 2002):

$$T_s = \frac{T_l T_f}{1 - R_l R_f} \tag{5.17A}$$

$$R_s = R_l + \frac{T_l^2 R_f}{1 - R_l R_f} \tag{5.17B}$$

If the light first passes through the clean filter layer, the model predicts that transmittance, T_c, is still given by equation 5.17A. However, filter substrates are not uniform over their depths and have visually distinguishable front and back surfaces. Therefore, measurements of T_s and T_c are expected to differ. For the model substrate, reflectance R_c is given by:

$$R_c = R_f + \frac{T_f^2 R_l}{1 - R_l R_f} \tag{5.18}$$

Attenuation (*ATN*) due to the aerosol deposit is calculated by applying Beer-Lambert's law relating to the reduction in transmittance of an exposed filter (T_s) relative to a blank (T_b) (Campbell et al., 1995; Bond et al., 1999). For a non-absorbing filter substrate, all attenuation of incident light must be caused by aerosol light absorption. Therefore, *ATN* is a measure of $\tau_{a,s}$.

$$ATN = \ln\left(\frac{T_b}{T_s}\right) = \ln\left(\frac{1 - R_b}{T_s}\right) \tag{5.19}$$

Here, R_b is the reflectance of the blank. An alternate measure of filter-aerosol optical depth utilizes transmittance and reflectance of the clean face of the filter (Campbell et al., 1995; White et al., 2016). This reflectance measurement R_c can be assumed to be approximately equal to R_b. PTFE blanks are non-absorbing, therefore the numerator in equation 5.19 can be replaced by $T_b = 1 - R_b \approx 1 - R_c$. It should be noted that for translucent Teflon filters, R_b and R_c cannot be assumed to be exactly equal (Clarke, 1982; Campbell et al., 1995). Therefore, we represent this measure of

optical depth by a separate variable, OD_c, where the subscript denotes that the transmittance and reflectance values used corresponds to the clean side of the filter:

$$OD_c = \ln(\frac{1-R_c}{Tc}) \quad (5.20)$$

Finally, we define an optical depth measure using sample-side transmittance and reflectance, which can be interpreted as a measure of transmission of the fraction of incident radiation that is not backscattered by the filter-aerosol system:

$$OD_s = \ln(\frac{1-R_s}{T_s}) \quad (5.21)$$

Values of *ATN*, OD_c and OD_s for a range of $\tau_{a,s}$ values (0-1) are shown in Figure 5.3 for two cases: (1) highly absorbing aerosols (SSA=0.3) and (2) highly scattering aerosols (SSA=0.95). We illustrate that OD_c is nearly equal to *ATN* for the absorbing aerosol case, but there are significant differences between the two optical measures when the filter is loaded with highly scattering aerosols. This is because a translucent substrate with a reflective coating on its back behaves like a mirror: reflectance of the substrate increases when such a coating is applied. We also find that *ATN* shows the largest variation with SSA for a given value of $\tau_{a,s}$ while OD_s exhibits the smallest variation. This can be attributed to the changing relationships between R_s and filter loading for different SSA values. Figure 5.4 shows the change in R_s with respect to R_b plotted against the associated change in T_s, with increasing filter loading, for two discrete SSA values. For large SSA, $R_s > R_b$ and therefore, from equations 5.19 and 5.20, $OD_s < ATN$. The converse is true for small SSA values. It should be noted that fixed blank optics–based on the mean of transmittance and reflectance measurements (measurement techniques are described in the following section) on 20 blank filters–were used to model *ATN*, OD_c and OD_s. The purpose of this exercise was to illustrate the sensitivity of the above optical depth measures to SSA values of aerosols deposited on identical

media. A sensitivity analysis (Figure 5.5) showed that these findings hold for a large range (1-30%) values of the fractional penetration depth (χ).

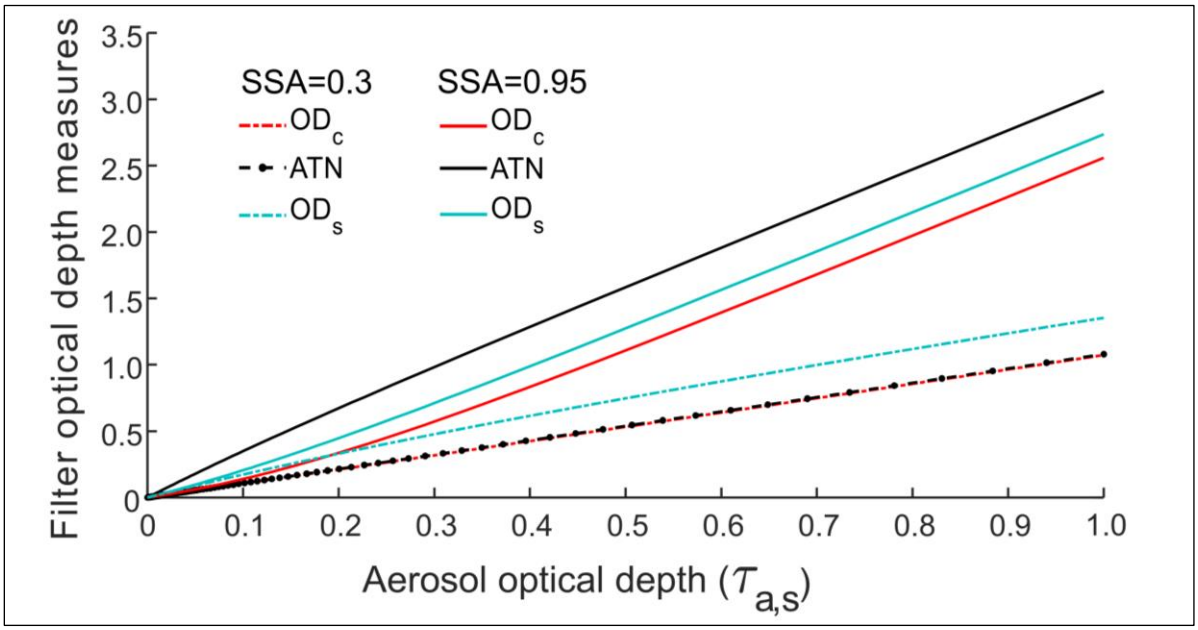

Figure 5.3: Modeled values of filter optical depth measures (OD_c, ATN and OD_s) with increasing aerosol optical depth ($\tau_{a,s}$) of deposited highly absorbing (SSA=0.3) or highly scattering (SSA=0.95) aerosols. Fixed blank optics were assumed.

The variation in filter optical measures with SSA was quantified by calculating the means and standard deviations of ATN, OD_c and OD_s, over SSA values ranging 0.2-0.99 for each input value of $\tau_{a,s}$. A total of 500 linearly spaced points along the SSA range were used. Blank filter properties were also varied within the model in accordance with the range observed over the 20 lab blanks. For every model sample, defined by a given SSA and $\tau_{a,s}$ combination, a model blank was generated assuming a normal distribution of blank transmittance values (mean=0.7, standard deviation = 0.02). Figure 5.4 shows the ratio of standard deviation to the corresponding average values of each filter optical depth measure. The relatively low standard deviation in OD_s (for most loading values) implies that this variable is a good candidate for estimating aerosol light absorption from filter optical measurements, for a wide range of aerosol types. The increase in standard

deviation with increasing loading is mainly contributed by very high SSA points which are typically associated with lower absorption per unit mass: therefore very high mass loadings of such aerosols would be required to yield the upper range of the $\tau_{a,s}$. For SSA<0.9, modeled attenuation values show little spread (<15% variability around the mean) with changing SSA. A surface plot of OD_s for all model data points (0.2<SSA<0.99 and $0<\tau_{a,s}<1$) is shown in Appendix A1.

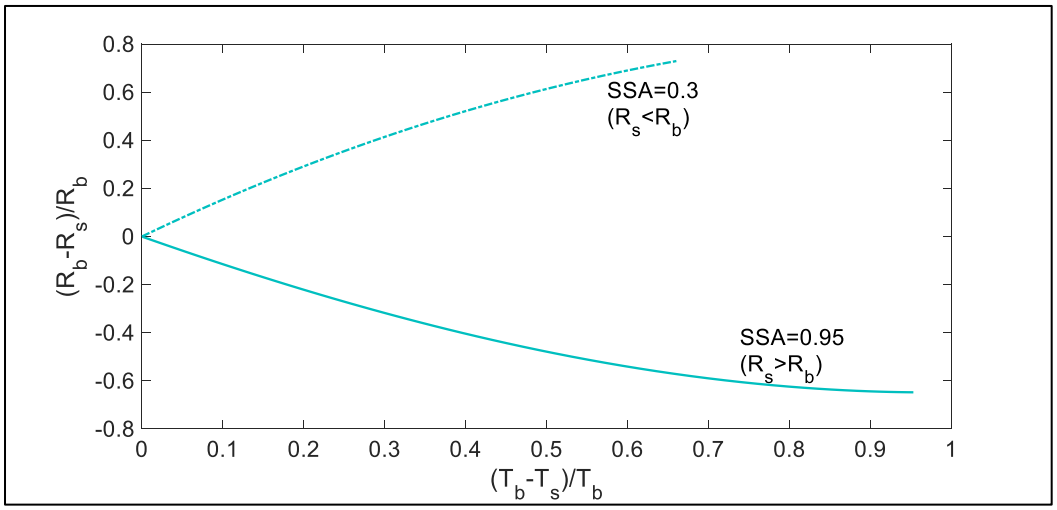

Figure 5.4: Change in sample-side reflectance as a function of the corresponding change in transmittance for predominantly absorbing (SSA=0.3) and scattering (SSA=0.95) aerosol types when blank optics are fixed.

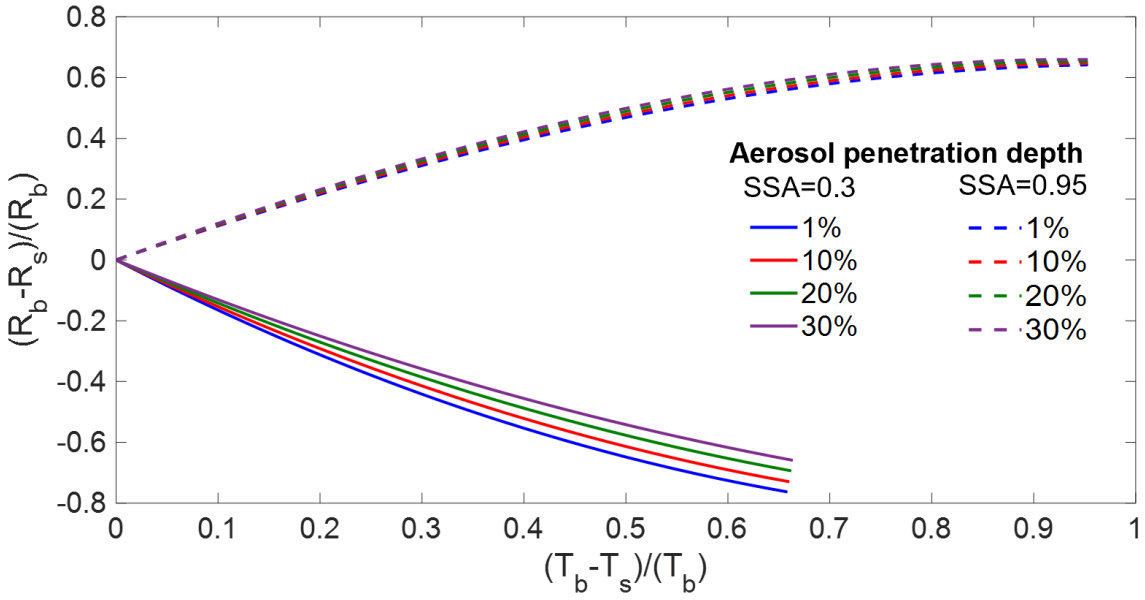

Figure 5.5: Same as Figure 5.4 but for different assumed values of aerosol fractional penetration depth χ.

5.4. Experimental methods

Diverse biomass fuels including wood and needles from pine, fir and sage trees, grass, peat and cattle dung were burned in a 21 m^3 stainless steel combustion chamber located at Washington University (Sumlin et al. (2017); Sumlin et al. (2018)). Flaming, smoldering and mixed combustion phases were employed to generate a range of intrinsic aerosol properties: SSA values at 375, 405 and 532 nm ranged 0.4-0.99 and Absorption Ångström Exponents (AÅE) for 375-532 nm ranged 1.2-6.8. A kerosene lamp was used to generate soot particles, with an SSA of ~0.3 and AAE within 0.70-1.1. A schematic of the experimental setup is shown in Figure 5.6. Experimental conditions and intrinsic aerosol optical properties for each fuel-combustion phase combination are listed in Table 5.1. Burn protocols for the three combustion phases were as follows:

1. Peat was smoldered using a heating plate at a temperature of 200º C. Other biomass types were smoldered by first establishing flaming (for 1-2 min) by igniting the fuel with a lighter and then starving the flame by covering the fuel container. While the biomass was flaming, the chamber exhaust was left open; the exhaust was closed once the flames were extinguished. The sample line between the chamber and mixing volume was connected 5 min after closing the exhaust.
2. To isolate the flaming phase, the biomass was ignited with a lighter and the chamber exhaust was closed. We monitored the flame visually from outside the combustion chamber, closing off the sample line between the chamber and the mixing volume once the flames were out.

3. For mixed phase sampling, flaming was established following the procedure above and emissions were continuously pulled into the mixing volume even after the flames were extinguished.
4. Some biomass types like Ponderosa pine and Douglas fir did not sustain smoldering combustion and were only sampled in flaming and mixed conditions. Other types like dung and Lodgepole pine were found to not sustain a flame. Kerosene was burned using a wick lamp. Intrinsic optical properties from the combustion of certain biomass types varied from burn to burn for the same combustion protocol. For such cases, the ranges of observed properties are given in the table below. During each burn, a steady state (10-40 min long) was established within which the absorption and scattering coefficients were nearly constant.

Approximately 10-50 g of a given type of woody biomass/grass/dung was placed in a stainless-steel pan and ignited using a flame. It was either allowed to continue flaming or brought to a smoldering phase by starving the flame with a lid. In the same type of pan, 5-15 g of peat was smoldered by using a ring heater to raise its temperature to 200 ºC. In one set of experiments, smoke from the chamber was directly sampled, while in another set, a hood placed over the pan was used for sampling the aerosols. The chamber exhaust was closed during the burns. The outlet from the hood or chamber was passed through a diffusion dryer and a semi-volatile organic compound (SVOC) denuder into a mixing volume, from which aerosols were continuously sampled by the four IPNs.

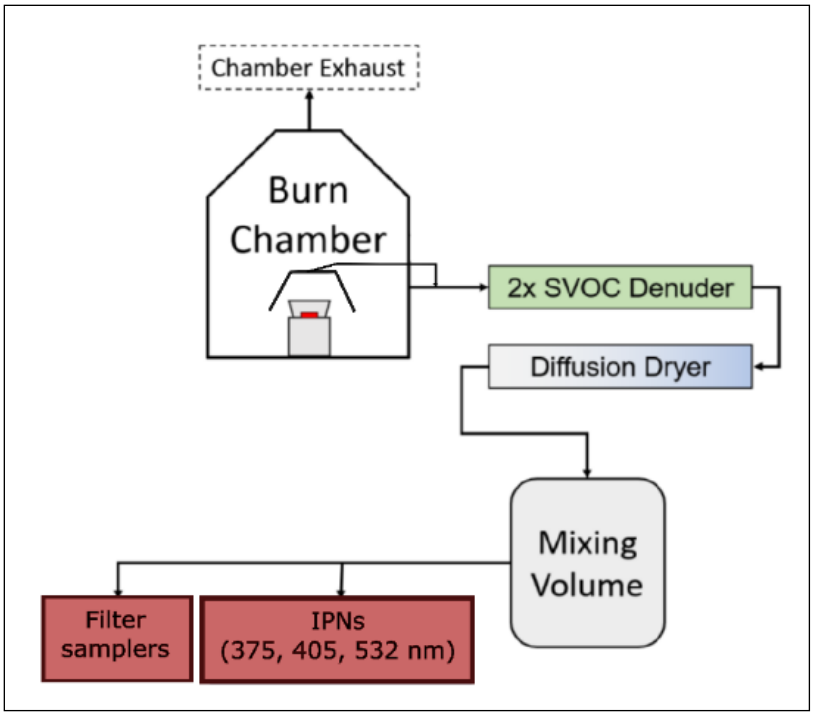

Figure 5.6: Schematic representation of the experimental setup. Inlet to the semi-volatile organic compound denuder was taken from either the chamber sampling port or the hood. IPN stands for integrated photoacoustic-nephelometer spectrometers.

Table 5.1: Number of burns conducted, and filter samples collected for each fuel type and combustion phase in this study. Intrinsic optical properties of emissions from each study condition are also given.

Fuel	Combustion phase	SSA			AAE	# of burns	# of filter samples
		375 nm	405 nm	532 nm	375-532 nm		
Dung	smoldering	0.86	0.95	0.98	6.1-6.6	6	7
Peat	smoldering	0.92	0.97	0.99	4.8-6.8	2	3
Sage	smoldering	0.75-0.87	0.86-0.93	0.93-0.97	2.8-5.3	4	14
	mixed	0.56-0.77	0.69-0.84	0.71-0.87	1.5-2.3	3	7
	flaming	0.43-0.65	0.62-0.69	0.69-0.77	0.9-1.4	2	5
Grass	smoldering	0.74	0.87	0.94	3.2-4.7	3	7
	flaming	0.76	0.81	0.85	1.7	1	3
Lodgepole pine	smoldering	0.84	0.93	0.97	4.2	2	3
Ponderosa pine	mixed	0.61-0.84	0.74-0.91	0.76-0.95	1.2-3.0	4	9
	flaming	0.56	0.65	0.65	0.7	1	2
Douglas fir	mixed	0.82	0.89	0.93	2.7	1	2
	flaming	0.60	0.70	0.71	0.9	1	3
Hardwood pellets	mixed	0.80-0.87	0.92-0.95	0.95-0.98	4.1-6.1	1	3
Kerosene	flaming	0.27	0.30	0.31	0.7-1.1	3	7

During each burn, optical (absorption and scattering coefficients) signals were monitored using IPNs until a steady state was reached. During the steady state, particle samples were collected on 47 mm PTFE membrane (Pall) filters. The filter sampling flow rate was set to 5 liters per minute and the sampling durations were between 2 and 20 minutes. For each filter sample, $\tau_{a,s}$ of the deposited aerosols was calculated from the absorption coefficients measured using the IPNs:

$$\tau_{a,s} = \frac{b_{abs,av} \times Q \times t_s}{10^9 A_s} \quad (5.22)$$

where $b_{abs,av}$ is the average absorption coefficient (in Mm^{-1}) during the sampling duration t_s (in min), Q is the flow rate (in liters per minute or lpm) through the filter and A_s is the filter sample area (in m^2). Optical depth $\tau_{a,s}$ for the samples in this study ranged between 0.01 and 0.68. The uncertainty in these estimates was predominantly from the standard deviation in $b_{abs,av}$ over the averaging interval, and was within 10% for all samples. Values of $b_{abs,av}$ at 532 nm ranged from ~300 Mm^{-1} for smoldering samples to ~20000 Mm^{-1} for flaming phase samples; the corresponding range at 375 nm was ~3000-30000 Mm^{-1}.

Sample-side transmittance (T_s) and reflectance (R_s) for the filter samples were measured using a Perkin-Elmer LAMBDA 35 UV-vis spectrophotometer (described in Zhong and Jang (2011)). This instrument contains an integrating sphere and two sample holders. Transmittance was measured by placing the sample in the first holder ahead of the sphere, in the direction of the sample beam, while a white standard was placed in the second holder (behind the sphere). Reflectance was measured by keeping the first holder empty and placing the sample in the second holder. Both measurements were performed on the sample face of the filter: light was incident on the side that was exposed to the sample air. Each measurement was normalized to the baseline transmittance/reflectance value of the measurement system: between every 10 sample scans, transmittance/reflectance were measured with no sample placed in the first holder and a white standard was placed in the second holder. Sample transmittance/reflectance values were then divided by the corresponding baseline. Only T_s and R_s were measured for all samples in this study as model results indicated that OD_s is better suited than OD_c for estimating $\tau_{a,s}$. To test the validity of this assumption, transmittance and reflectance were also measured on the clean side of the filter (T_c and R_c, respectively) for a subset of the samples (n=54). This subset corresponded to samples

collected during 17 biomass burning experiments which yielded aerosols with SSA (375, 405 and 532 nm) ranging 0.54-0.99. For all samples, we found $T_s > T_c$.

From normalized T_s and R_s measurements, OD_s was calculated using equations 5.21. When this equation is applied to blank filters, it results in OD_s values between 0.01-0.03. A wavelength dependent "blank optical depth" was subtracted from the sample data. Triplicate transmission and reflection measurements were used to estimate measurement uncertainty, which is attributable to random fluctuations in the measurements. Means and standard deviations of the OD_s values calculated from the replicate measurements yielded an uncertainty (ratio of standard deviation to mean) of 5% in OD_s. Similarly, OD_c was calculated for the 54-sample subset.

A correction factor (C) that captures the net effect of multiple scattering and aerosol loading can be defined as:

$$\tau_{a,s} = C \times OD_s \implies C = \frac{\tau_{a,s}}{OD_s} \tag{5.23}$$

A list of relevant parameters (measured or assumed from previous studies) described in Chapters 5.3 and 5.4 is shown in Table 5.2.

Table 5.2: Particle and filter properties for artifact correction.

Filter	absorption and scattering optical depths	derived from transmittance and reflectance measurements on pristine filters (T_b, R_b)
Aerosol	absorption and scattering optical depths ($\tau_{a,p}$, $\tau_{s,p}$)	calculated from *in-situ* absorption and scattering coefficient measurements
	asymmetry parameter (g_p)	fixed value assumed in the model (0.6)
Filter-aerosol system	relative particle penetration depth (χ)	fixed value assumed in the model (10%)
	transmittance and reflectance of the particle laden layer (T_1, R_1)	modeled as a function of $\tau_{a,f}$, $\tau_{s,f}$, g_f, $\tau_{a,p}$, $\tau_{s,p}$, g_p, χ
	transmittance and reflectance of the two-layer system (T_s, R_s, R_c)	modeled as a function of $\tau_{a,f}$, $\tau_{s,f}$, g_f, $\tau_{a,p}$, $\tau_{s,p}$, g_p, χ measured through spectrophotometry

5.5. Empirical correction scheme for filter artifacts

The model described in Chapter 5.3 was used to calculate filter optical depths for each experimental sample (using measured $\tau_{a,s}$ and SSA values as inputs). Modeled and experimental values of OD_s for the samples are shown in Figure 5.7. The two datasets are highly correlated (Pearson R= 0.92), but the model predicted larger values of OD_s than those experimentally determined. This disagreement may partially be due to differences between assumed parameters in our model and their real-world values. It is also likely that assuming an average propagation direction of diffuse radiation within the two-stream approximation (Sagan and Pollack, 1967; Arnott et al., 2005) causes this systematic difference.

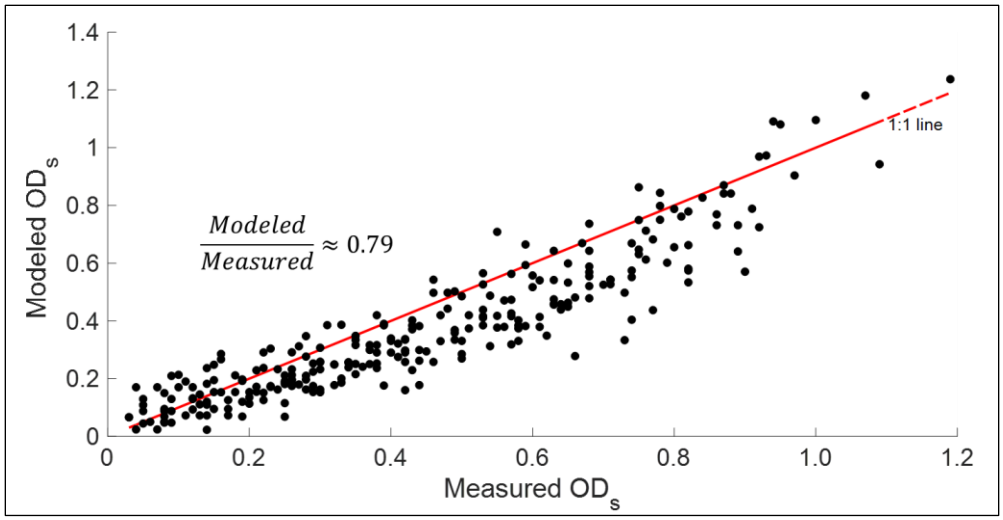

Figure 5.7: Modeled filter optical depth (OD_s) for absorption optical depth and single scattering albedo values of the aerosols sampled in this study compared with the corresponding filter measurements. A 1:1 line is shown in red. The average ratio of modeled to measured OD_s is 0.79.

In Figure 5.8, we combined all experimental ($\tau_{a,s}$ versus OD_s) data corresponding to the three wavelengths since our measurements showed no clear stratification with varying wavelength. The relationships between $\tau_{a,s}$ and modeled values of OD_s, OD_c and ATN are presented in Figure 5.9; modeling predicts the lowest scatter in the $\tau_{a,s}$-OD_s curve. Further, Figure 5.10 shows $\tau_{a,s}$ plotted against measured OD_s and OD_c (at all three wavelengths) for the aforementioned 54 filter sample subset, demonstrating that $\tau_{a,s}$ is better correlated with OD_s than with OD_c. Ordinary least-squares regression was applied to obtain power-law fits included in the plot legend. The corresponding relationship for all points in Figure 5.8 is given by ($R^2 = 0.87$):

$$\tau_{a,s} = 0.48\ (OD_s)^{1.32} \tag{5.24}$$

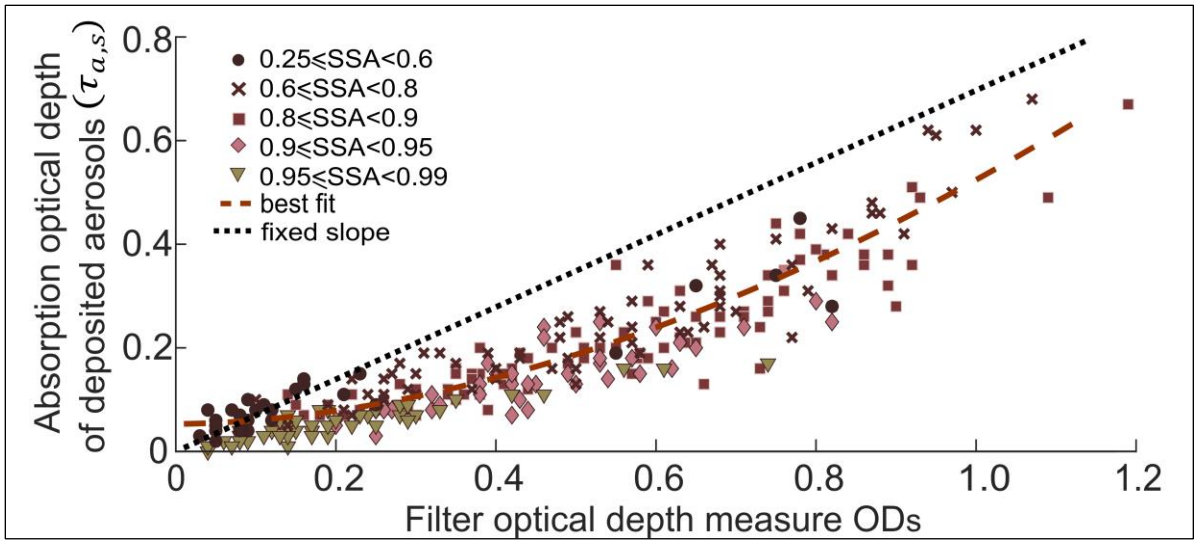

Figure 5.8: Relationship between *in-situ* aerosol optical depth ($\tau_{a,s}$) and filter optical depth OD_s for all (n=75) samples, measured at 375, 405 and 532 nm (N=225 data points). The best fit curve is given by equation 5.24, with $R^2 = 0.87$. The black perforated line has a fixed slope of 0.67 per Zhong and Jang (2011)). Uncertainties (1 standard deviation) in OD_s ranged 2-5%, while those in $\tau_{a,s}$ were 5-10%.

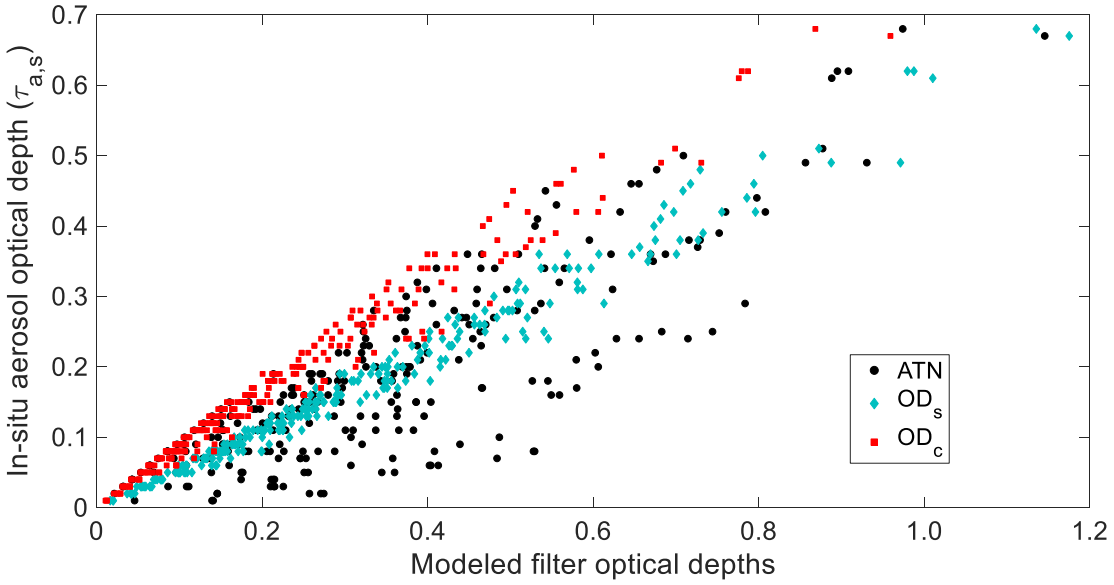

Figure 5.9: The relationship between experimentally measured *in-situ* aerosol optical depth ($\tau_{a,s}$) and modeled values of filter optical depth measures (OD_c, *ATN* and OD_s). Blank optics were randomly generated for each sample point from a normal distribution with mean=0.7 and standard deviation=0.02.

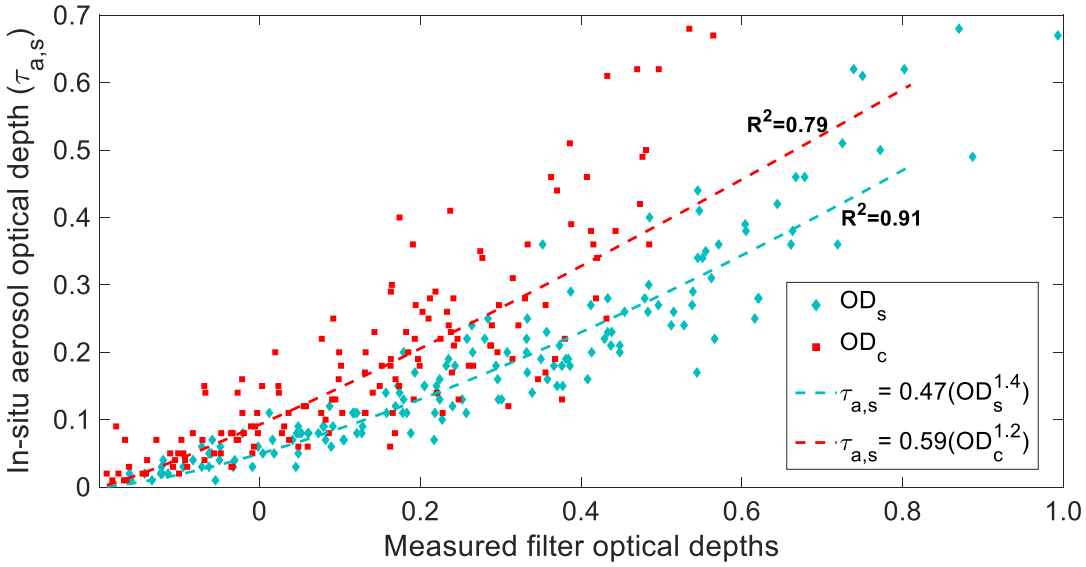

Figure 5.10: Relationship between *in-situ* aerosol optical depth ($\tau_{a,s}$) and measured values of filter optical depth measures OD_c and OD_s for a subset of 54 filter samples, measured at 375, 405 and 532 nm (N=162 data points). Uncertainties were as in Figure 5.8.

Also shown in Figure 5.8 are estimated values estimated using a constant correction factor C of 0.67 proposed by Zhong and Jang (2011) (black perforated line); this correction factor clearly overestimates $\tau_{a,s}$ for most OD_s values investigated in this study. We find our data to be better represented by an approximate C = 0.46 based on a linear least-squares fit (R^2 = 0.79). However, any constant C value does not capture the non-linearity of the interaction between aerosol properties and the multiple-scattering within the filter medium. It should be noted that C in equation 5.23 represents the net effects of all filter artifacts. There are measurement errors associated with both OD_s and $\tau_{a,s}$, and therefore, C contains propagation of uncertainties from both parameters. No correlation was observed between C and OD_s. We observed an inverse relationship between C and SSA (Figure 5.11), consistent with results the from the two-stream radiative transfer model. For a given value of $\tau_{a,s}$, OD_s will always be higher for aerosols with higher SSA

values. Consequently, we should expect *C* to decrease with increasing SSA; this decreasing relationship in our data is given by:

$$C = -0.76 * SSA + 1.02 \quad (5.25)$$

Values of *C* and SSA for individual samples were aggregated into five SSA bins to demonstrate the inapplicability of an empirical correction factor formulation to low SSA data points in this study. The large spread in *C* values for low SSA is likely due to noise amplification from dividing two small ($\tau_{a,s}$ and OD_s < 0.2) numbers. For SSA>0.6, the above linear fit holds.

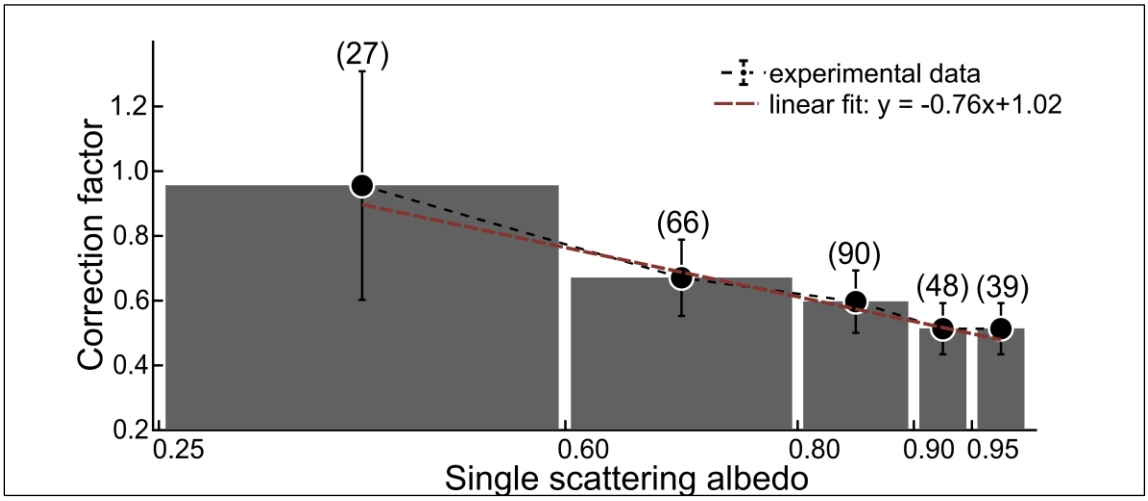

Figure 5.11: Correction factor C for filter artifacts as a function of single scattering albedo of the deposited aerosols. Error bars show one standard deviation around the mean. The numbers in parentheses denote the number of data points in each bin.

In summary, the relationship between *in-situ* aerosol light absorption and attenuation of aerosol deposits on Teflon filters was evaluated for combustion aerosols (encompassing 0.25 ≤ SSA ≤ 0.99), at 375, 405 and 532 nm wavelengths. An empirical non-linear relationship was found between the absorption optical depth of sampled aerosols and attenuation through filter samples; the nature of this function was consistent with predictions from a two-stream radiative transfer

model of the filter-aerosol system. Following equation 5.24, we propose the estimation of aerosol MAC (m^2g^{-1}) values from filter OD_s measurements using:

$$MAC = [0.48\ (OD_s)^{1.32}]\frac{A_s}{m} \quad (5.26)$$

where A_s is the filter sample area (in m^2) and m is the mass on deposited particles (in g). Additionally, aerosol absorption coefficients (b_{abs}; in Mm^{-1}) can also be calculated using:

$$b_{abs} = [0.48\ (OD_s)^{1.32}]\frac{10^9 A_s}{Q \times t_s} \quad (5.27)$$

The quantities Q and t_s are as used in equation 5.22. Caution must be taken, as suggested by the two-stream model results, on the limits of applicability of the empirical relationships–significant errors could result from application of the relationships if the aerosol SSA>0.9 and OD_s values are beyond the range of this work.

Teflon filters are routinely used for gravimetric and elemental analysis across monitoring networks (Chow et al., 2010; Solomon et al., 2014; Snider et al., 2015), as well as field and laboratory source characterization studies. In many measurement systems, such as the Hybrid Integrating Plate and Sphere (HIPS) method (Bond et al., 1999) used by the IMPROVE network, transmittance and reflectance are measured on the clean side of the filter and the optical depth OD_c is calculated (Campbell et al., 1995; White et al., 2016). The relationship between aerosol optical depth, $\tau_{a,s}$, and OD_c showed a larger variability across varying SSA than that between $\tau_{a,s}$ and OD_s. Therefore, we suggest further evaluation of OD_s as an optical depth measure that can be empirically connected to particulate phase light absorption for a range of aerosol types.

References

Andreae, M. and Gelencsér, A.: Black carbon or brown carbon? The nature of light-absorbing carbonaceous aerosols, Atmos. Chem. Phys., 6, 3131-3148, 2006.

Arnott, W. P., Hamasha, K., Moosmüller, H., Sheridan, P. J., and Ogren, J. A.: Towards aerosol light-absorption measurements with a 7-wavelength aethalometer: Evaluation with a photoacoustic instrument and 3-wavelength nephelometer, Aerosol Sci. Technol., 39, 17-29, 2005.

Bohren, C. F.: Multiple scattering of light and some of its observable consequences, Am. J. Phys, 55, 524-533, 1987.

Bond, T. C., Anderson, T. L., and Campbell, D.: Calibration and intercomparison of filter-based measurements of visible light absorption by aerosols, Aerosol Sci. Technol., 30, 582-600, 1999.

Bond, T. C. and Bergstrom, R. W.: Light absorption by carbonaceous particles: An investigative review, Aerosol Sci. Technol., 40, 27-67, 2006.

Bond, T. C., Doherty, S. J., Fahey, D., Forster, P., Berntsen, T., DeAngelo, B., Flanner, M., Ghan, S., Kärcher, B., and Koch, D.: Bounding the role of black carbon in the climate system: A scientific assessment, J. Geophys. Res.: Atmos., 118, 5380-5552, 2013.

Campbell, D., Copeland, S., and Cahill, T.: Measurement of aerosol absorption coefficient from Teflon filters using integrating plate and integrating sphere techniques, Aerosol Sci. Technol., 22, 287-292, 1995.

Cappa, C. D., Lack, D. A., Burkholder, J. B., and Ravishankara, A.: Bias in filter-based aerosol light absorption measurements due to organic aerosol loading: Evidence from laboratory measurements, Aerosol Sci. Technol., 42, 1022-1032, 2008.

Chakrabarty, R., Moosmüller, H., Chen, L.-W., Lewis, K., Arnott, W., Mazzoleni, C., Dubey, M., Wold, C., Hao, W., and Kreidenweis, S.: Brown carbon in tar balls from smoldering biomass combustion, Atmos. Chem. Phys., 10, 6363-6370, 2010.

Chen, Y. and Bond, T.: Light absorption by organic carbon from wood combustion, Atmos. Chem. Phys., 10, 1773-1787, 2010.

Chow, J. C., Watson, J. G., Green, M. C., and Frank, N. H.: Filter light attenuation as a surrogate for elemental carbon, J. Air Waste Manage. Assoc., 60, 1365-1375, 2010.

Clarke, A. D.: Effects of filter internal reflection coefficient on light absorption measurements made using the integrating plate method, Appl. Opt., 21, 3021-3031, 1982.

Davies, N. W., Fox, C., Szpek, K., Cotterell, M. I., Taylor, J. W., Allan, J. D., Williams, P. I., Trembath, J., Haywood, J. M., and Langridge, J. M.: Evaluating biases in filter-based aerosol absorption measurements using photoacoustic spectroscopy, Atmos. Meas. Tech. Discuss., 2019, 1-38, 2019.

Gorbunov, B., Hamilton, R., and Hitzenberger, R.: Modeling radiative transfer by aerosol particles on a filter, Aerosol Sci. Technol., 36, 123-135, 2002.

Kirchstetter, T. W., Corrigan, C. E., and Novakov, T.: Laboratory and field investigation of the adsorption of gaseous organic compounds onto quartz filters, Atmos. Environ., 35, 1663-1671, 2001.

Kirchstetter, T. W., Novakov, T., and Hobbs, P. V.: Evidence that the spectral dependence of light absorption by aerosols is affected by organic carbon, J. Geophys. Res.: Atmos., 109, 2004.

Koistinen, K. J., Kousa, A., Tenhola, V., Hänninen, O., Jantunen, M. J., Oglesby, L., Kuenzli, N., and Georgoulis, L.: Fine particle (PM25) measurement methodology, quality assurance

procedures, and pilot results of the EXPOLIS study, J. Air Waste Manage. Assoc., 49, 1212-1220, 1999.
Kubelka, P.: New contributions to the optics of intensely light-scattering materials. Part I, Josa, 38, 448-457, 1948.
Lack, D. A., Cappa, C. D., Covert, D. S., Baynard, T., Massoli, P., Sierau, B., Bates, T. S., Quinn, P. K., Lovejoy, E. R., and Ravishankara, A.: Bias in filter-based aerosol light absorption measurements due to organic aerosol loading: Evidence from ambient measurements, Aerosol Sci. Technol., 42, 1033-1041, 2008.
Martins, J. V., Artaxo, P., Liousse, C., Reid, J. S., Hobbs, P. V., and Kaufman, Y. J.: Effects of black carbon content, particle size, and mixing on light absorption by aerosols from biomass burning in Brazil, J. Geophys. Res.: Atmos., 103, 32041-32050, 1998.
Müller, T., Virkkula, A., and Ogren, J.: Constrained two-stream algorithm for calculating aerosol light absorption coefficient from the Particle Soot Absorption Photometer, Atmos. Meas. Tech., 7, 4049-4070, 2014.
Petzold, A. and Schönlinner, M.: Multi-angle absorption photometry—a new method for the measurement of aerosol light absorption and atmospheric black carbon, J. Aerosol Sci, 35, 421-441, 2004.
Reid, J. S., Eck, T. F., Christopher, S. A., Koppmann, R., Dubovik, O., Eleuterio, D., Holben, B. N., Reid, E. A., and Zhang, J.: A review of biomass burning emissions part III: intensive optical properties of biomass burning particles, Atmos. Chem. Phys., 5, 827-849, 2005.
Sagan, C. and Pollack, J. B.: Anisotropic nonconservative scattering and the clouds of Venus, J. Geophys. Res., 72, 469-477, 1967.
Saleh, R., Hennigan, C., McMeeking, G., Chuang, W., Robinson, E., Coe, H., Donahue, N., and Robinson, A.: Absorptivity of brown carbon in fresh and photo-chemically aged biomass-burning emissions, Atmos. Chem. Phys., 13, 7683-7693, 2013.
Saleh, R., Robinson, E. S., Tkacik, D. S., Ahern, A. T., Liu, S., Aiken, A. C., Sullivan, R. C., Presto, A. A., Dubey, M. K., and Yokelson, R. J.: Brownness of organics in aerosols from biomass burning linked to their black carbon content, Nature geoscience, 7, 647-650, 2014.
Snider, G., Weagle, C., Martin, R., Van Donkelaar, A., Conrad, K., Cunningham, D., Gordon, C., Zwicker, M., Akoshile, C., and Artaxo, P.: SPARTAN: a global network to evaluate and enhance satellite-based estimates of ground-level particulate matter for global health applications, Atmos. Meas. Tech., 8, 505, 2015.
Solomon, P. A., Crumpler, D., Flanagan, J. B., Jayanty, R., Rickman, E. E., and McDade, C. E.: US National PM2. 5 chemical speciation monitoring networks—CSN and IMPROVE: description of networks, J. Air Waste Manage. Assoc., 64, 1410-1438, 2014.
Subramanian, R., Roden, C. A., Boparai, P., and Bond, T. C.: Yellow beads and missing particles: Trouble ahead for filter-based absorption measurements, Aerosol Sci. Technol., 41, 630-637, 2007.
Sumlin, B. J., Heinson, Y. W., Shetty, N., Pandey, A., Pattison, R. S., Baker, S., Hao, W. M., and Chakrabarty, R. K.: UV–Vis–IR spectral complex refractive indices and optical properties of brown carbon aerosol from biomass burning, J. Quant. Spectrosc. Radiat. Transfer, 206, 392-398, 2018.
Sumlin, B. J., Pandey, A., Walker, M. J., Pattison, R. S., Williams, B. J., and Chakrabarty, R. K.: Atmospheric Photooxidation Diminishes Light Absorption by Primary Brown Carbon Aerosol from Biomass Burning, Environ Sci Technol Lett, 4, 540-545, 2017.

Sun, H., Biedermann, L., and Bond, T. C.: Color of brown carbon: A model for ultraviolet and visible light absorption by organic carbon aerosol, Geophys. Res. Lett., 34, 2007.
Vecchi, R., Bernardoni, V., Paganelli, C., and Valli, G.: A filter-based light-absorption measurement with polar photometer: Effects of sampling artefacts from organic carbon, J. Aerosol Sci., 70, 15-25, 2014.
Virkkula, A.: Correction of the calibration of the 3-wavelength Particle Soot Absorption Photometer (3λ PSAP), Aerosol Sci. Technol., 44, 706-712, 2010.
Virkkula, A., Ahlquist, N. C., Covert, D. S., Arnott, W. P., Sheridan, P. J., Quinn, P. K., and Coffman, D. J.: Modification, calibration and a field test of an instrument for measuring light absorption by particles, Aerosol Sci. Technol., 39, 68-83, 2005.
Weingartner, E., Saathoff, H., Schnaiter, M., Streit, N., Bitnar, B., and Baltensperger, U.: Absorption of light by soot particles: determination of the absorption coefficient by means of aethalometers, J. Aerosol Sci, 34, 1445-1463, 2003.
White, W. H., Trzepla, K., Hyslop, N. P., and Schichtel, B. A.: A critical review of filter transmittance measurements for aerosol light absorption, and de novo calibration for a decade of monitoring on PTFE membranes, Aerosol Sci. Technol., 50, 984-1002, 2016.
Zhong, M. and Jang, M.: Light absorption coefficient measurement of SOA using a UV–Visible spectrometer connected with an integrating sphere, Atmos. Environ., 45, 4263-4271, 2011.

Chapter 6: Constraining OC contribution to light absorption by cookstove emissions

As discussed in Chapter 4.2, cookstove emissions performance has been characterized by mass emission factors of aerosol (and gaseous) pollutants through laboratory WBT studies and more recently, field measurements on in-use cookstoves. A few of the studies (Roden et al., 2006; Habib et al., 2008; Stockwell et al., 2016; Weyant et al., 2019) summarized in Table 4.4 also reported the light absorption properties of cookstove aerosol emissions. Roden et al. (2006) reported MAC and MSC values determined from real-time PSAP and nephelometer measurements, respectively, made during their Honduran field study. Habib et al. (2008) calculated MAC and AAE from transmittance measurements on Nucleopore filters (sampled in their detailed laboratory study of Indian biomass fuels) made using an integrating plate nephelometer. In Weyant et al. (2019), PSAP and narrow-angle red-wavelength light sensor measurements were used to estimate MAC and MSC, respectively, for Indian, Nepalese and Tibetan stoves. All of these studies applied the Bond et al. (1999) correction scheme to their multi-wavelength filter-based absorption measurements, which might lead to a ~20-45% overestimation of the MAC values (Davies et al., 2019). Stockwell et al. (2016) used photoacoustic spectroscopy to measure in-situ absorption, at 405 and 870 nm, for Nepalese biomass cookstoves. The more recent studies (Stockwell et al., 2016; Weyant et al., 2019) provide an estimate of light absorption attributable to OC emissions but neither reported spectral MAC values for cookstove OC emissions. This poses a challenge in expanding the conventional discussion of aerosol climate impact which considers BC emitted as the only significant form of light-absorbing carbonaceous aerosol (Ramanathan et al., 2001; Venkataraman et al., 2005; Ramanathan and Carmichael, 2008; Carmichael et al., 2009; Bond et al., 2013). In

this section, I first discuss the difficulties in apportioning light absorption to BC and OC and the sources of uncertainties in such an analysis. Initial estimates of OC absorption properties based on a preliminary round of sampling cookstove emissions in India are presented in Chapter 6.2. This study had a small sample size and was conducted following approaches and assumptions typically used in literature. A larger number of aerosol samples, from the field study described in Chapter 4, were later analyzed with crucial improvements made to filter optical analysis (Chapter 6.3). These updated findings are compared with the studies discussed above in Chapter 6.4.

6.1. Attributing aerosol light absorption to OC and EC

Conventionally, all light absorption by combustion generated aerosols was attributed to BC particles but newer generations of climate models include brown carbon as a light-absorbing form of OC in addition to the strongly absorbing BC (Chung et al., 2012; Feng et al., 2013; Wang et al., 2014). The light-absorbing efficiency of OC aerosols is connected with their physical and chemical properties, a function of fuel properties and combustion conditions (Chen and Bond, 2010). Optical properties and refractiveness of OC particles lie on interlinked continua: absorption efficiency and thermal-stability are linked with high molecular weight organic compounds formed under flaming conditions (Andreae and Gelencsér, 2006; Sun et al., 2007; Saleh et al., 2014; Laskin et al., 2015; Saleh et al., 2018). Higher relative abundances of BC are correlated with higher light absorbing efficiency of the co-emitted OC (Saleh et al., 2014). Cookstove emissions in this study are characterized by fuel-wise average BC/OC ratios of 0.08-0.15, which is on the lower end of the range (0.04-1.67) from laboratory cookstove tests of similar fuel types (Habib et al., 2008) but larger than field measurement of BC/OC ratios (0.02-0.08) for open biomass burning (Aurell et al., 2015; Strand et al., 2016; Holder et al., 2017). Thermal carbon profiles of the emissions in this study show that thermally stable OC, that evolves at 450 ºC in an inert atmosphere, is the largest

particulate fraction (~50% of total carbon mass , on average) (Pandey et al., 2017). Therefore, OC is expected to be important contributor to light absorption by cookstove emissions. However, there are fundamental challenges in separately measuring the properties of co-emitted BC and OC in addition to specific limitations pertaining to cookstove studies.

In a real-time measurement system, a thermodenuder can be used to vaporize organic aerosols and absorption measurements taken before and after denuding (Cappa et al., 2012; Lack et al., 2012; Lack and Langridge, 2013; Saleh et al., 2013; Saleh et al., 2014). The optical measurements are typically supplemented with size or mass observations of the total aerosol and its BC/OC components in order to perform optical closure, yielding absorption cross-section or refractive index of OC. There are two sources of bias in such an analysis: (1) thermodenuding does not remove non-refractory OC which likely contributes to light absorption (Cappa et al., 2013) and (2) BC particles coated with non-absorbing organics show an absorption enhancement (Cappa et al., 2008; Lack et al., 2008; Lack et al., 2012; Saleh et al., 2013), referred to as the "lensing effect", which needs to be treated separately from absorption due to externally-mixed OC. Further, thermodenuder measurements are performed sequentially which can lead to confounding observations (like enhanced absorption *after* denuding) about the optical behavior of emissions that fluctuate over time (Cappa et al., 2013). Finally, the power requirement for a thermodenuder, and associated pumps, may be prohibitive for field studies of cookstoves in rural areas of the developing world.

A prevalent method for estimating OC light absorption is the extraction of organic material into a suitable organic solvent or water from a filter sample of emissions (Chen and Bond, 2010; Liu et al., 2013) followed by optical analysis with a UV-vis spectrometer. This approach allows for physical isolation of OC aerosols but studies report that 2-15% of all OC mass is not soluble in

even non-polar solvents (Chen and Bond, 2010; Cheng et al., 2016; Xie et al., 2017). The magnitude of this insoluble fraction and its (unmeasured) absorption efficiency depends on OC composition which is known to widely vary with fuel and combustion characteristics (Andreae and Gelencsér, 2006; Laskin et al., 2015). The extraction efficiency of OC in water is significantly lower (Chen and Bond, 2010) but several studies consider water-soluble organics as a proxy for all OC.

Particle light absorption (*ABS*) estimated from filter-based optical analyses (detailed in Chapter 5) can be attributed to BC and OC using a two-component model (Kirchstetter et al., 2004; Kirchstetter and Thatcher, 2012). This technique exploits the difference in the spectral absorption dependences of these components (Figure 1). It is assumed that absorption at wavelengths greater than a certain threshold (λ_t) is due to BC alone. Values of λ_t in literature range 660-880nm (Kirchstetter et al., 2004; Kirchstetter and Thatcher, 2012; Pokhrel et al., 2017). A fixed spectral dependence of light absorption by BC is assumed, consistent with a body of experimental observations and theoretical analyses for freshly emitted small BC particles (Kirchstetter et al., 2004; Andreae and Gelencsér, 2006; Bond et al., 2013).This dependence is parameterized by BC absorption Angstrom exponent (AAE_{BC}). OC contribution to wavelengths smaller than λ_t is estimated as:

$$ABS_{OC}(\lambda) = ABS_{PM} - ABS_{BC} = ABS_{PM} - ABS_{PM,700}\left(\frac{\lambda}{700}\right)^{-AAE_{BC}} \quad (6.1)$$

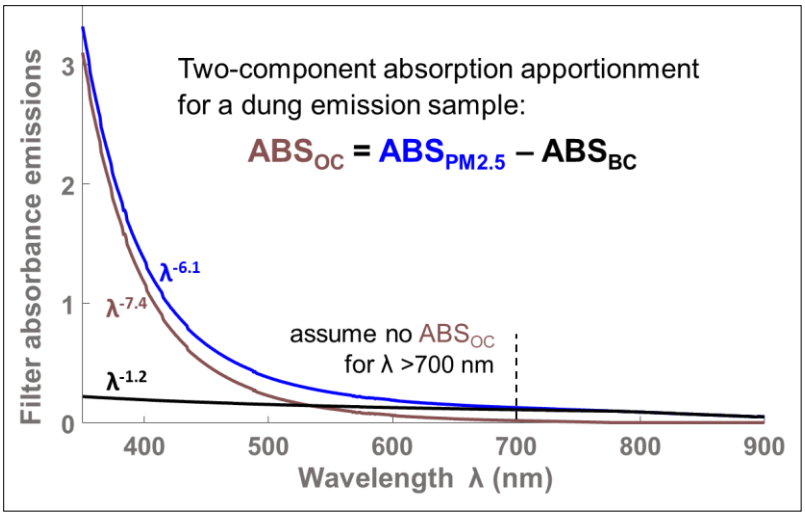

Figure 6.1: Absorption spectrum for a sample of dung emissions is deconvoluted by assigning all absorption at wavelengths greater than λ_t (chosen as 700 nm here) to BC and extrapolating BC absorption at smaller wavelengths using a fixed BC AAE (1.2 in the figure).

Kirchstetter et al. (2004) found that the values of OC absorption estimated using AAE_{BC} of 1 compared well with those calculated from acetone extracts of the aerosol samples. However, the validity of this assumption requires further testing against first principle measurements (Andreae and Gelencsér, 2006; Lack and Langridge, 2013; Laskin et al., 2015).

6.2. Preliminary study of light absorption by cookstove OC emissions

6.2.1. Sampling and analysis

Between October and December 2014, we conducted sampling of particulate matter emissions from traditional "three-stone" cookstoves in rural households in Chhattisgarh, a state in central India. This region has witnessed accelerated warming and anomalous rainfall patterns (Jain and Kumar, 2012; Khavse et al., 2014), which in turn have impacted the agricultural yield, food security, and livelihood (Sastri, 2009; Murali and Afifi, 2014). Over 97% of the households in rural Chhattisgarh use solid biomass fuels for cooking purposes (Census, 2011). On a national

level, 62%, 12% and 11% of rural households rely primarily on fuel-wood, agricultural residue and dung cake, respectively, to meet their cooking energy needs. Mud *chulhas* and three-stone On an average, they have similar particulate emissions characteristics (Habib et al., 2008; MacCarty et al., 2008), and are often treated as a single 'baseline biomass stove' (Pandey et al., 2014) technology category.

Three households that primarily used one of the three primary solid fuel types (one each for users of fuel-wood, agricultural residue, dung cake) were selected in rural Chhattisgarh, India. Additionally, based on the typical practice in the region, a fourth fuel category was identified – mixed fuel (a combination of roughly 25% dung cake, 60% fuel-wood, 10% agricultural residue and 5% coal cake), which was used in each of these households. The fuels were locally purchased or scavenged by the households, which did not facilitate the quantitative determination of their moisture content. Sampling was conducted during one of the two typical cooking times: morning (around 6:30AM to 9:00AM) and evening (around 5:30 PM to 7:30PM). The households prepared their regular meals consisting of rice, vegetables, and/or *chapatis* (wheat-flour breads).

The sampler inlets were placed at ~ 1 m from the emission point to allow for cooling and dilution with ambient air. Emissions of particulate matter with aerodynamic diameter smaller than 2.5 μm (or $PM_{2.5}$) were drawn from the plume of each source through Harvard sharp impactors using MiniVol portable air samplers (AirMetrics Model 4.2). Pre-fired 47 mm quartz-fiber filters and Teflon membrane filters were mounted to the air samplers. Flow rates through the filters were programmed at 5 LPM. Sampling duration was varied between 15 and 65 min, depending on the cooking operation at hand. Five quartz-fiber and five Teflon filters were used to collect aerosol samples emitted from each of the four fuel types. The aerosol deposit yields ranged 0.5–1.8 mg/filter. Field blank collection was carried out before each of the morning and evening cooking

activities. Aerosols were also deposited on Transmission Electron Microscopy (TEM) grids (Ted Pella, Inc.) to characterize their morphology.

Relative abundances of Elemental Carbon (EC) and OC in the aerosol samples were estimated using the Interagency Monitoring of Protected Visual Environments (IMPROVE) thermal/optical reflectance (TOR) method (Watson and Valberg, 2001; Chow et al., 2007). In this study, the estimated EC mass in aerosol samples has been approximated to be the BC mass (Venkataraman et al., 2005; Chakrabarty et al., 2014). This approximation, while having found wide usage in the aerosol community, has its limitations. EC is operationally defined as the fraction of carbon that is oxidized above a set temperature during thermal or thermal-optical analysis (Andreae and Gelencsér, 2006). Corresponding to a particular temperature threshold and the protocol used, corrections are applied to best estimate the mass of pure carbon in its refractory (or graphitic) form (Andreae and Gelencsér, 2006; Chow et al., 2007). In theory, BC and EC are equivalent proxies for combustion generated refractory carbon (Andreae and Gelencsér, 2006; Bond et al., 2013). Experimentally, their measurements have potential sources of bias, especially in the presence of OC (including light absorbing OC or LAOC) in the sample. Past studies have estimated these biases to result in at least a factor of 2 uncertainty in BC and EC masses (Andreae and Gelencsér, 2006; Bond et al., 2013; Petzold et al., 2013). Therefore, we qualify our approximation with the caveat that BC in this manuscript refers to the apparent refractory carbon.

The absorption coefficients of sampled aerosols in Teflon media were measured using a PerkinElmer LAMBDA 35 ultraviolet-visible spectrophotometer (Zhong and Jang, 2011). In this instrument, a double integrating sphere system detects the intensity of radiation, with a wavelength between 200-1100 nm, transmitted or reflected through a sample deposited on a filter medium. The spectral resolution of this instrument is 1 nm. For wavelengths ranging 300-900 nm, we

measured the transmittances through field-blank and loaded filters. The relative lowering of transmission through a loaded filter, compared to a blank filter, could be attributed primarily to light absorption by the deposited aerosols. From this, the Beer-Lambert Law (Kirchstetter et al., 2004; Zhong and Jang, 2011) is used to relate aerosol absorbance (*ABS*) to light attenuation (*ATN*) through the filter as:

$$ATN(\lambda) = \ln\left(\frac{I_0(\lambda)}{I(\lambda)}\right) \quad (1A)$$

$$ABS(\lambda) \approx \frac{ATN(\lambda)}{C} \quad (1B)$$

where *C* is a correction factor (=1.5±0.15), that accounts for increased path length due to multiple scattering in Teflon filters (Zhong and Jang, 2011; Drinovec et al., 2014), and I_0 and *I* are the radiation intensity transmittance (%) values through blank and loaded filters. A normally distributed instrument uncertainty was applied to the measured transmittance values based on the observed random error, which was within 5% of the average measurement values. The resulting uncertainty in *ATN* (= $\ln(I_0/I)$) was estimated by analytically propagating the instrument error. The output uncertainties also followed a normal distribution. The confidence intervals for *ABS* were calculated by combining in quadrature the relative uncertainties in *C* and *ATN* (equation 1B).

Another artifact pertinent to filter based measurements is the loading effect of absorbing aerosols, which serves to lower the apparent attenuation with increasing aerosol loading. Empirical calibration factors for filter measurements of BC absorption (Weingartner et al., 2003; Arnott et al., 2005; Drinovec et al., 2014) typically correct for this artifact, but similar corrections are not available for LAOC loading artifact. We evaluated this effect for the present samples by plotting the filter mass loading values against *ATN* at 350 nm (Figure S2). A weak linear relationship

(R^2=0.35) was found to best fit the data. Similar results were obtained for *ATN* values at 550 and 880 nm as functions of the mass loading. This does not provide any conclusive evidence on the effects of filter mass loading on the *ATN* values in this study. Based on previous studies, the absorption related loading artifact for aerosols emitted from biomass burning is expected to be weak (Kirchstetter and Thatcher, 2012). Additionally, high loading of scattering aerosols (like OC) results in an increase in optical path (Subramanian et al., 2007; Cappa et al., 2008; Lack et al., 2008), leading to the overestimation of *ABS*. The net effect of high loadings of (absorbing and scattering) aerosols depends on the optical nature and relative abundances of BC, LAOC and non-absorbing OC. We noted here that the development of filter artifact correction factors for biomass cookstove (or other OC dominated) emissions was needed to improve the accuracy of filter-based analyses. To that end, we conducted the study discussed in Chapter 5 and the results of that study were applied to future analysis.

We attributed the entire attenuation at λ_t = 880 nm to BC (Chakrabarty et al., 2010; Kirchstetter and Thatcher, 2012) and estimated ABS_{OC} using equation 6.1 a mean AAE_{BC} value of 1. In order to account for the variability in the wavelength dependence of light absorption by BC externally mixed with non-absorbing OC, we assumed a range of 0.7-1.3 for AAE_{BC} (Schnaiter et al., 2006; Gyawali et al., 2009; Chung et al., 2011; Lack and Langridge, 2013). For the above range of AAE_{BC} values, the variation in ABS_{OC} at 350 nm, with respect to its mean value at AAE_{BC} =1, was 6-14% (Figure 6.2). Therefore, one standard deviation uncertainties (±6-14%) were assigned to the deconvolution method and combined analytically with the other uncertainties in equation 1.

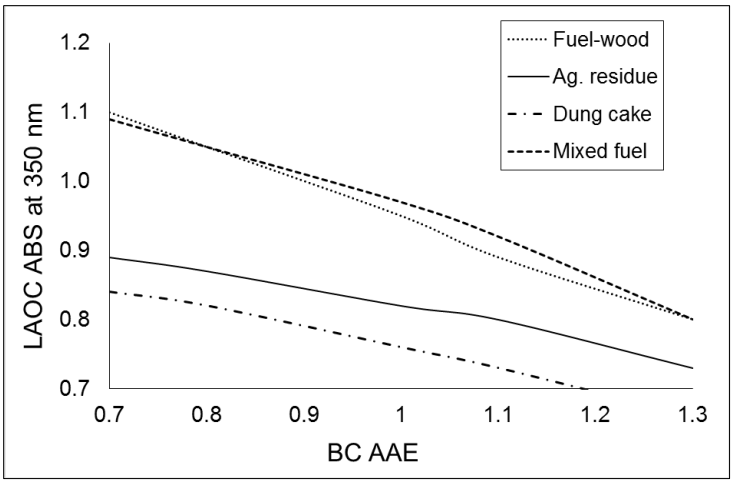

Figure 6.2: Average LAOC ABS values at 350 nm wavelength as functions of BC AAE for fuel-wood, agricultural residue, dung cake and mixed fuel.

Using the ratio of OC and EC content from IMPROVE-TOR analysis, and assuming a mean value of 1.9 (with a standard deviation of 0.15) for organic matter (OM) to OC ratio (Turpin and Lim, 2001; Pitchford et al., 2007; Chen, 2011), the total $PM_{2.5}$ mass was apportioned to BC and OC mass as:

$$m_{BC} = \frac{m_{PM\,2.5}}{1+1.9\frac{OC}{EC}} \tag{6.2}$$

$$m_{OC} = m_{BC}\frac{OC}{EC} \tag{6.3}$$

where m_{BC} and m_{OC} are the respective values of BC and OC masses, and OC/EC is the mean ratio of OC to EC mass for each fuel type. The MAC values for the bulk aerosol deposits, BC and OC mass were calculated as:

$$MAC(\lambda) = \frac{A}{m}ABS(\lambda) \tag{6.4}$$

$$MAC_{BC}(\lambda) = \frac{A}{m_{BC}} \frac{ATN_{BC}(\lambda)}{C} \tag{6.5}$$

$$MAC_{OC}(\lambda) = \frac{A}{m_{OC}} \frac{ATN_{LAOC}(\lambda)}{C} \tag{6.6}$$

where A is the area of the filter and m is the mass of aerosol deposited. Confidence intervals around the mean MAC values were estimated from analytical propagation of the underlying uncertainties. A lognormal distribution was used to calculate asymmetric 95% confidence intervals when the resulting uncertainty (ratio of standard deviation to mean) was greater than 30%. Since *ATN* is the only directly measured quantity which captures the wavelength dependence of light absorption, we calculated AAEs by fitting power law curves to the *ATN* datasets in the wavelength range of 350-550 nm. Values of *ABS* and MAC were calculated by multiplying the measured *ATN* values with wavelength independent quantities. Therefore, the uncertainties in AAE arise only from the uncertainties in *ATN*.

The total $PM_{2.5}$ *ATN* and its LAOC attributable fraction were integrated over spectral solar irradiance between λ = 300 and 900 nm to estimate the fraction of light absorbed by LAOC (instead of BC):

$$F_{LAOC} = \frac{\int_{300nm}^{900nm} ATN_{LAOC}(\lambda) i(\lambda) d\lambda}{\int_{300nm}^{900nm} ATN_{PM_{2.5}}(\lambda) i(\lambda) d\lambda} \tag{6.7}$$

where F_{LAOC} is the fraction of the visible solar radiation absorption attributable to LAOC (W/g $PM_{2.5}$), and i is the solar insolation as a function of wavelength λ (W/m^2 nm).

6.2.2. Appearance of filter samples and deposited particles

The color of the particulate matter collected on quartz and Teflon filters was yellow-brown to brown (Figure 6.3), consistent with previous observations of LAOC-dominated filter samples from biomass burning (Andreae and Gelencsér, 2006; Chakrabarty et al., 2010). Figure 6.4A shows typical TEM images of an amorphous OC particle (Chakrabarty et al., 2010). Such particles, with sizes ranging 100-300 nm, were found in abundance in the samples collected from different fuel emissions in this study. These particles were co-emitted with BC aggregates (Figure 6.4B), composed of 40-70 nm diameter monomers.

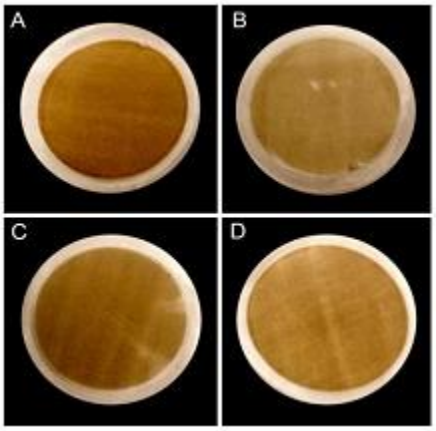

Figure 6.3: Images of Teflon filter samples of aerosols from the combustion of (A) fuel-wood, (B) agricultural residue, (C) dung-cake and (D) mixed fuel in traditional cookstoves.

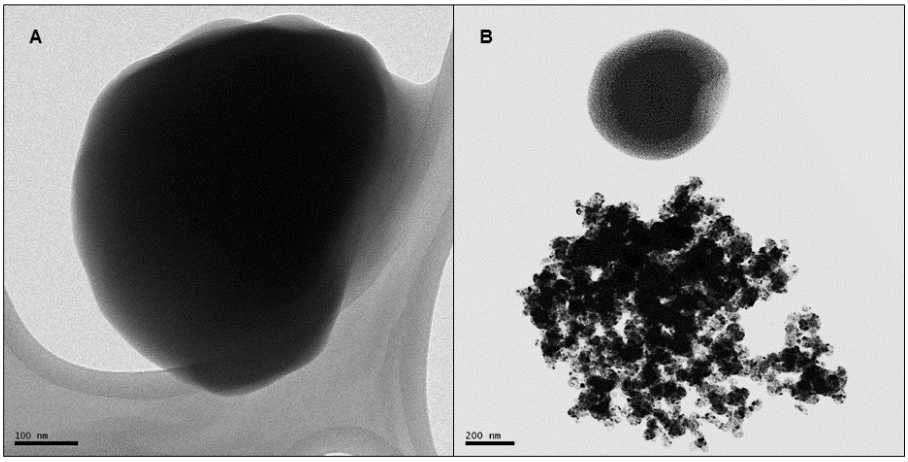

Figure 6.4: TEM images of (A) an amorphous OC particle typically emitted from fuels in this study and (B) OC particle with co-emitted BC aggregate.

6.2.3. Absorbance and MAC values of PM, BC and OC

Average aerosol *ABS* for $PM_{2.5}$ emissions from the four fuel types are shown in Figure 6.5A. The de-convoluted spectra for BC and LAOC (per equation 6.1) show that the majority of the aerosol *ABS* in the 300-500 nm wavelength range could be attributed to LAOC. Consistent with previous studies, absorption by biomass-emitted LAOC nearly drops to zero around 600 nm (Kirchstetter et al., 2004; Kirchstetter and Thatcher, 2012).

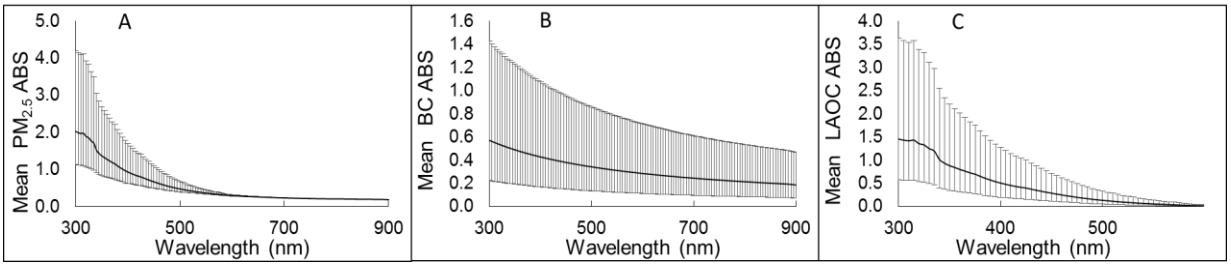

Figure 6.5**:** Average biomass ABS values for (A) $PM_{2.5}$ emissions, and their (B) BC and (C) LAOC components. Error bars represent 95% CI around the means, based on the standard errors of the means.

Estimated OC/EC ratios for each biomass fuel sample are presented in Table 6.1. A mean ratio of 12 was measured for fuel-wood, which is within the range of values reported from past field

measurements (0.5-13.5) by Roden et al. (2006). However, this ratio is 3-30 times higher than those typically reported from laboratory-based experiments (Habib et al., 2008; MacCarty et al., 2008). Differences in testing procedure, fuel characteristics, and operating conditions make direct comparisons between field and laboratory measurements difficult, but there is evidence that real-world cooking conditions result in a higher number of smoldering events and higher particulate organic content than standard laboratory testing protocols (Roden et al., 2009). The mean OC/EC ratios for agricultural residue and dung cakes were a factor of 8-20 and 1.5-5 higher, respectively, than previous laboratory measurements (Parashar et al., 2005; Habib et al., 2008; Saud et al., 2012). Habib et al. (2008) suggested that the low density and high surface-to-volume ratios of rice straw and other crop residues could lead to large amounts of emissions of OM. This may explain why this study found the OC/EC ratios for agricultural residue to be 4-5 times higher than those for other biomass fuels.

Table 6.1: Ratio of OC to BC mass and optical properties (MAC and AAE) for aerosol samples by biomass fuel type.

Fuel type	OC/EC[1,2]	$PM_{2.5}$ MAC at 550 nm[1] (m^2/g)	BC MAC at 550 nm[1] (m^2/g)	OC MAC at 350 nm[1,3] (m^2/g)	$PM_{2.5}$ AAE[1,4]	OC AAE[1,4]
Fuel-wood	12.1 (3.2-31.0)	1.3 (0.67-2.5)	12.2 (6.1-32.4)	4.4 (1.3-12)	2.4 (2.2-2.7)	5.8 (5.6-5.9)
Agricultural residue	60 (24-133)	0.6 (0.2-1.5)	32.2 (10.6-80.8)	3.6 (1.1-9.4)	3.3 (3.0-3.7)	5.8 (5.5-6.0)
Dung cake	15.4 (11-22)	0.5 (0.29-0.86)	15.1 (3.4-34.3)	3.4 (2-5.4)	3.6 (3.3-3.6)	7.7 (7.5-7.9)
Mixed fuel	14.5 (11-20)	0.9 (0.61-1.15)	17.9 (7.6-37.4)	4.1 (2.5-6.4)	3.0 (2.8-3.1)	6.0 (5.8-6.1)

[1] All values expressed as means (95 % confidence intervals)
[2] OC/EC values listed here are from the IMPROVE-TOR method
[3] OC MAC ~ 0.001-.2 at 550 nm
[4] AAE is between 550 nm and 350 nm

We find that the values of $PM_{2.5}$ MAC (Table 6.1, see Figure 6.6 for detailed plots) for fuel-wood and agricultural residue in this study are slightly lower than those reported in Habib et al. (2008) and Roden et al. (2006), while our AAE values are higher. This is consistent with the substantially larger OC content measured in emissions from those fuel types in this study, compared to Habib et al. (2008). Our estimates of BC MAC (Table 6.1) fall within the broad range of values reported in literature (collated in Chen (2011)). The only exception being the BC MAC value estimated for agricultural residue emissions, which are significantly higher compared to those for other fuels. Samples from this particular fuel showed very low EC content and a large uncertainty in the OC/EC ratios (Table 6.1).

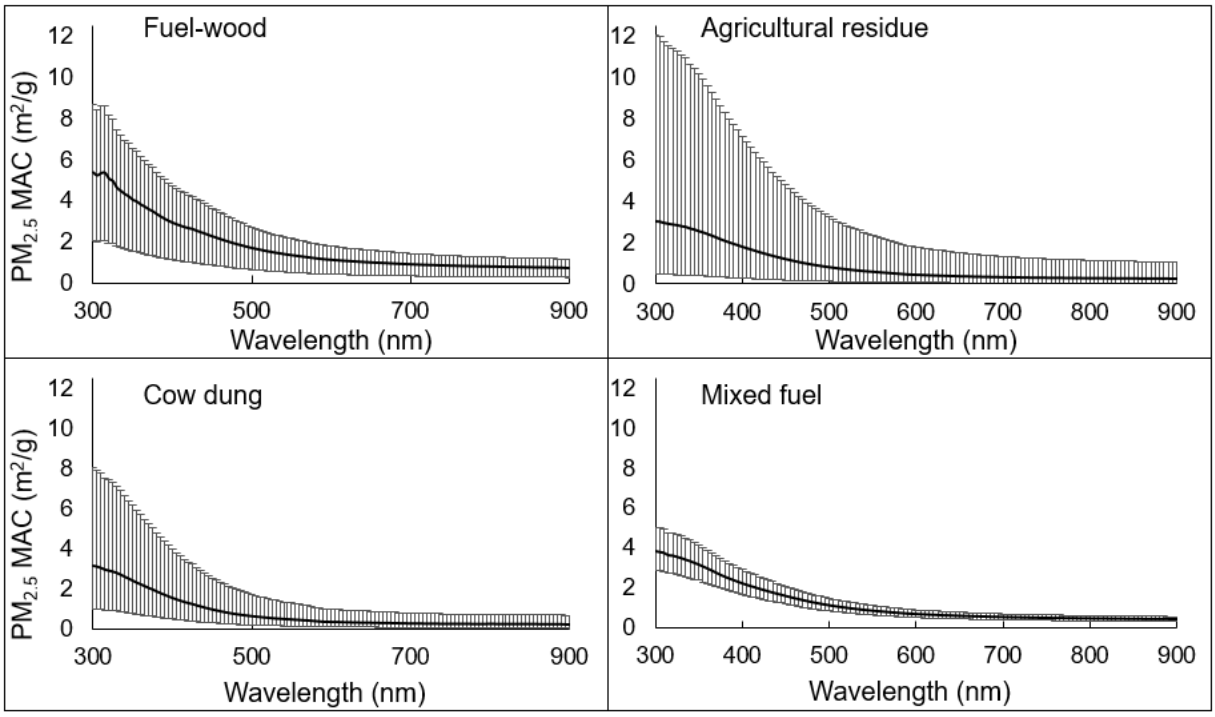

Figure 6.6: Fuel-wise $PM_{2.5}$ MAC values (m^2/g) as a function of the wavelength of incident radiation. The error bars represent 95% CI around the means, based on the standard errors of the means.

The average MAC values for OC emissions from the four fuel types are shown in Figure 6.7. We estimate average MAC values of 0.1 and 3.1 m^2g^{-1} at 550 and 350 nm, respectively, with a mean AAE of 6.3 (±1.8) in this wavelength range. We found that the OC MAC values for different fuel types showed little variability: ~ 10% variation from the overall mean, while the uncertainty in each fuel ranged between 20-50%. Previous estimates of OC MAC for woody-biomass burning in the United States (Kirchstetter et al., 2004; Lack et al., 2012; Washenfelder et al., 2015) are also shown for comparison. While the methodology for apportioning the OC component of aerosol absorption varies between the studies, there is good agreement between the resulting MAC values.

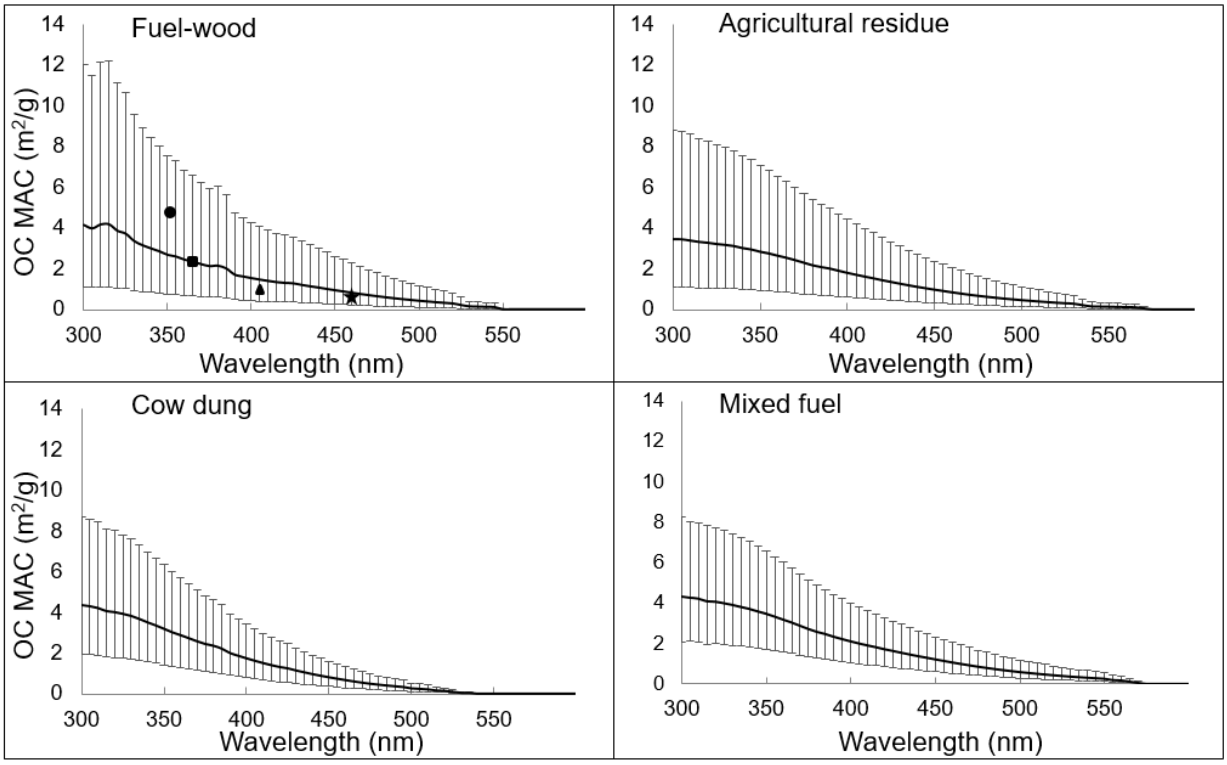

Figure 6.7: Fuel-wise OC MAC values (m^2/g) as a function of the wavelength of incident radiation. The error bars represent 95% CI around the mean. Symbols represent the mean OC MAC values reported from wood burning in literature [circle = Kirchstetter et al. (2004) square = Washenfelder et al. (2015); triangle = Lack et al. (2012); star = Chen (2011)].

As 70% of the incoming solar radiation energy is distributed in the 300-900 nm range, the integration of total $PM_{2.5}$ *ABS* and its LAOC component over solar insolation (in $Wm^{-2}nm^{-1}$) in this range gives a measure of their overall absorption behavior. Figure 6.8A shows the fraction of the total *ABS* attributed to LAOC in a typical aerosol sample from each fuel type, as a function of wavelength. Figure 6.8B shows the overall fraction of solar radiation in the 300-900 nm wavelength range that would be absorbed by LAOC rather than BC. Since aerosol scattering measurements were not conducted as part of this study, we could not compute the overall direct forcing efficiency, which could have provided a more quantitative estimate of the net climate impacts of LAOC. Nevertheless, our results indicate that LAOC contributes significantly (26-45%) to light absorption by real-world cookstove emissions. Agricultural residue emissions have the

highest OC/EC ratio (Table 6.1) and therefore the highest contribution to light absorption by LAOC. Compared to Kirchstetter and Thatcher (2012), we attribute a larger portion of the total absorption by biomass burning aerosol to LAOC, highlighting regional differences in the fuel properties and combustion technologies.

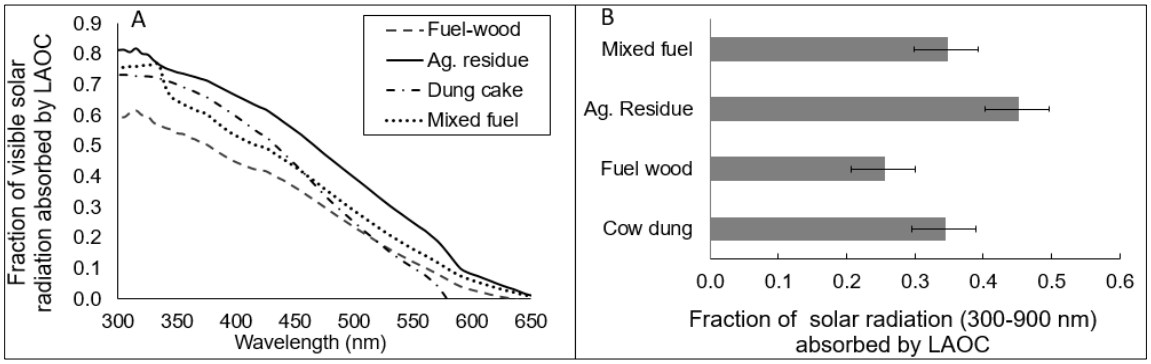

Figure 6.8. (A) Fraction of the total aerosol absorbance attributed to light absorbing OC as a function of wavelength. (B) Fraction of solar radiation (in the 300-900 nm range) absorption (Wm^{-2} aerosol) attributed to LAOC, per biomass fuel type. Error bars represent 1 standard error about the mean.

6.3. Analysis of comprehensive field study samples with updated filter correction

6.3.1. Sampling and analysis

Experimental methods for the field study conducted between December 19 and 30th of 2015 in Chhattisgarh, India have been detailed in Chapter 4. Briefly, thirty cooking tests with three fuel types (fuelwood, agricultural residue and cattle dung) were performed on a traditional mud *chulha*. Fuels were sourced from different regions that have a biomass user population. Each cooking test involved the preparation of a local meal item. A Testo-350 gas analyser continuously measured carbon monoxide (CO) and carbon dioxide (CO_2) during the cooking tests. $PM_{2.5}$ samples were collected on 47 mm Teflon membrane and quartz fiber filters using Minivol (5 L min^{-1}) samplers (AirMetrics Model 4.2), during different times in each cooking cycle. Teflon filters were weighed

before and after sampling using a microbalance at Pt. Harishankar Shukla University, Raipur, India to obtain the net mass deposited. Both sets of filters were stored in a freezer (-20 ºC) after each day of sampling. At the end of the study, the quartz filters were transported to Desert Research Institute, Nevada, where they were analyzed using the Interagency Monitoring of Protected Visual Environments – A (IMPROVE_A) thermal-optical reflectance (TOR) method (Chow et al., 2007; 2011) to determine elemental and organic carbon fractions in the sampled particulates. The Teflon filters were brought to Washington University in St Louis for optical analysis. For each filter, sample-side transmittance (T_s) and reflectance (R_s) were measured for wavelengths 350-900 nm (Pandey et al., 2019b) using a Perkin-Elmer LAMBDA 35 UV-vis spectrophotometer. The relevant optical depth (OD_s) of the filter-particle system was calculated as:

$$OD_s(\lambda) = \ln(\frac{1-R_s(\lambda)}{T_s\,(\lambda)}) \quad (6.8)$$

This optical depth was converted to particle-phase light absorption optical depth (ABS_{PM}) using the empirical correction scheme developed for carbonaceous aerosols in Chapter 5:

$$ABS_{PM}(\lambda) = 0.48\,(OD_s(\lambda))^{1.32} \quad (6.9)$$

The assumptions in the apportionment analysis were updated to reflect recent findings: BC particles emitted from biomass burning are likely to be coated with organic material that enhances light absorption with respect to pure BC. While the wavelength dependence of BC light absorption is described by an AAE of 1, modeling (Liu et al., 2018) and experimental (Gyawali et al., 2013) studies show that coated fractal-like BC aggregates have AAE ranging 0.9-1.5. A central BC AAE value of 1.2 (with 0.9 and 1.5 as lower and upper extremes, respectively) was used to describe BC spectral behavior here. All light absorption for wavelengths larger than λ_t = 700 nm was attributed to coated BC, and BC light absorption at smaller wavelengths was estimated from BC absorption

at 700 nm using the above AAE value. A lower value of λ_t was used here than in Pandey et al. (2016) because most samples in this study had negligible absorption at wavelengths greater than 700 nm. This was because care was taken to avoid overloading the filter samples so as not to exceed the limits of validity of our artifact correction scheme. OC light absorption was estimated as the difference between the total and coated BC absorption values. While the true value of BC AAE for each sample is uncertain, the use of a reasonable range of BC AAE values allows us to constrain OC contribution to light absorption.

Particulate absorption cross-sections were normalized by fuel consumption to estimate absorption emission factors (AEFs). The carbon mass balance technique was used to estimate the amount of fuel consumed during each sample collection interval, Δt_s. Absorption emission factors were calculated as:

$$\mathrm{AEF}_{PM} = \mathrm{ABS}_{PM} \times A_s \times \frac{\mathrm{CMF_{fuel}} \times Q \times \Delta t_s}{\Delta \mathrm{C_{CO_2}}\left(\frac{\mathrm{M_C}}{\mathrm{M_{CO_2}}}\right) + \Delta \mathrm{C_{CO}}\left(\frac{\mathrm{M_C}}{\mathrm{M_{CO}}}\right)} \qquad \backslash\ (6.10)$$

where A_s is the sample area (in m^2) on the filter and the last term on the right-hand side is the inverse of the mass of fuel consumed (g^{-1}). ΔC_{CO2} and ΔC_{CO} are the concentrations above ambient levels (background measured before each cooking test) of CO_2 and CO in g m^{-3}, respectively. M_C, M_{CO2}, and M_{CO} are the atomic or molecular weights of C, CO_2, and CO in g $mole^{-1}$. CMF_{fuel} is the carbon mass fraction of the fuel, which ranged from 33% to 50% for the tested fuels. Q is the volumetric flow rate through the filter, in m^3s^{-1}. Absorbances of the OC and BC components were used to calculated absorption emission factors (AEF_{OC} and AEF_{BC}, respectively), in a similar manner to the AEF_{PM} calculation above.

Dimensionless absorption or *ABS* for $PM_{2.5}$, BC and OC was also normalized by their respective mass loadings (in g/m^2) to calculate the corresponding mass absorption cross-sections ($MAC_{PM/BC/OC}$):

$$\mathrm{MAC}_{PM/OC/BC} = \mathrm{ABS}_{PM/OC/BC} \times \frac{1}{L_{PM/OC/BC}} \quad (6.11)$$

OC contribution to forcing by cookstove emissions was isolated by calculating a MAC value for $PM_{2.5}$ emissions with only BC-attributed light absorption:

$$\mathrm{MAC}_{PM,noOC} = \frac{\mathrm{ABS}_{BC}}{L_{PM}} = (\mathrm{ABS}_{PM} - ABS_{OC}) \times \frac{1}{L_{PM}} = \mathrm{ABS}_{PM}(1 - f_{OC}) \times \frac{1}{L_{PM}} \quad (6.12)$$

6.3.2. Absorption emission factors and light absorption emissions of BC and OC

Real-world cookstove operation can be treated as a series of combustion events situated between strongly flaming and pure smoldering conditions (Chen et al., 2012). Intrinsic optical properties of emitted particles are largely a function of burn conditions: previous cookstove studies observed strongly absorbing (BC like) emissions during strong flaming and a range of weakly absorbing emissions during other phases (Roden et al., 2006; Chen et al., 2012). Expectedly, AEFs in this study varied by the observed combustion conditions, with smoldering phase AEF values lower than AEFs for steady flaming conditions (Figure 6.9A). The unsteady flame conditions during the ignition phase are reflected in the large variability in ignition AEFs. Variability in burn conditions drives optical characteristics more than fuel type (Weyant et al., 2019): the differences between AEFs for the three fuel categories were statistically insignificant (unpaired Student's *t*-test, differences between groups not significant at p=0.05). Pooled AEF data for all samples show an approximately lognormal distribution factor with a large spread. We report a combined geometric mean of 3.7 m^2kg^{-1} fuel and 95% confidence intervals (CI) of 0.6-23.3 m^2kg^{-1} fuel.

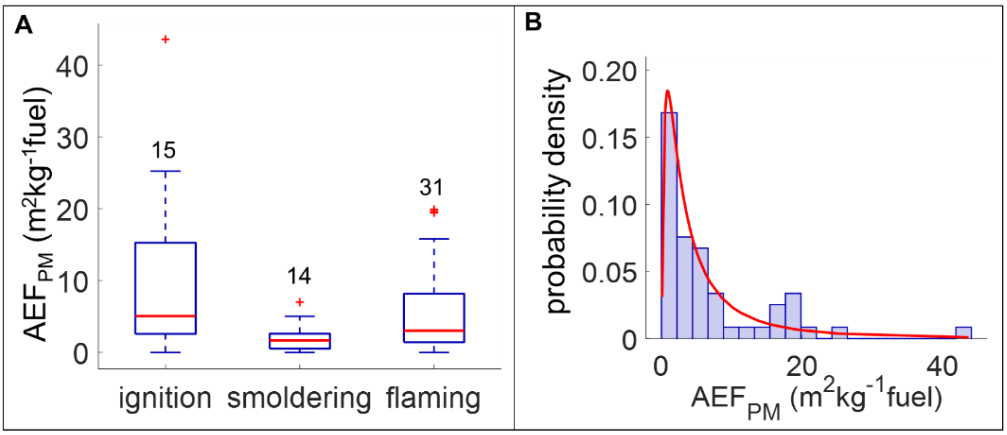

Figure 6.9: $PM_{2.5}$ absorption emission factors, or AEF_{PM} in m^2kg^{-1} fuel consumed, (A) grouped by observed combustion phase: boxes denote the upper and lower quartiles and whiskers denote 1.5 times the interquartile range, outliers are shown as red + symbols, number of samples for each category are specified above the whiskers and (B) shown as a histogram of all samples, overlaid by a fitted lognormal distribution.

Distributions of OC and BC AEF values are shown in Figure 6.10. For BC AAE of 1.2, we determined the ratio of geometric mean values of OC AEF to PM absorption at 550 nm as 0.37; this ratio for different BC AAE values ranged 0.30-0.43. Previous apportionment analyses of savanna wildfire smoke (Kirchstetter et al., 2004) and residential fireplace emissions (Kirchstetter and Thatcher, 2012) showed lower OC contributions to light absorption (13-32% at 500 nm). These absorption emission factors were combined with fuel use data to estimate annual light absorbing emissions, in Gm^2y^{-1} (Figure 6.11). Bottom-up biomass fuel use estimates disaggregated at the district level (Pandey et al., 2014) and multiplied by biomass-average AEFs. These emissions were gridded to a 0.1 by 0.1º spatial resolution. Mean value and 95% CI for absorption cross-section emissions from OC were 577 (64-2266) $Gm^2\ y^{-1}$, while those from BC were 988 (110-3897) Gg y^{-1}. Such optical inventories can be used to compare sectoral contributions to light absorption by BC and OC and discern patterns in the spatial distributions of these contributions. Figure 6.11 demonstrates absorption emissions hotspots over the Indo-Gangetic Plain, which is

associated with a higher than average aerosol burden (David et al., 2018) with a large contribution from the residential sector (Chowdhury et al., 2019).

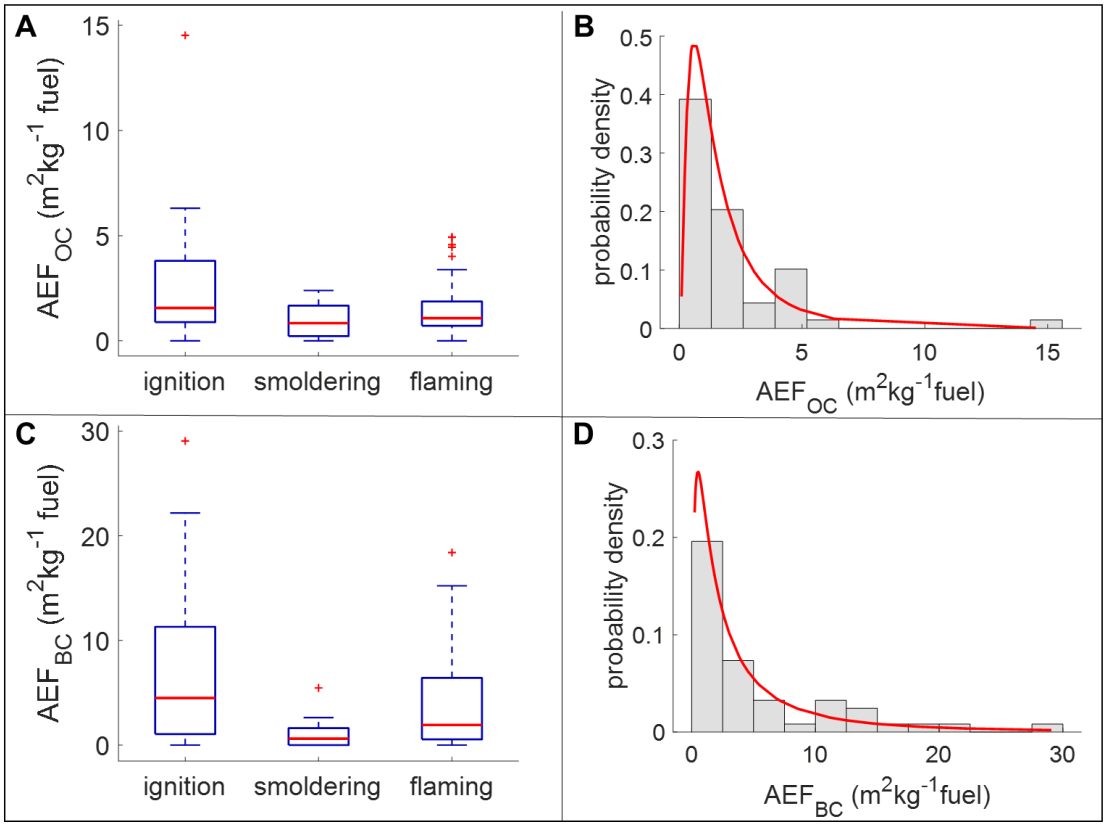

Figure 6.10: Absorption emission factors in m^2kg^{-1} fuel consumed: (A) AEF_{OC} grouped by observed combustion phase: boxes denote the upper and lower quartiles and whiskers denote 1.5 times the interquartile range, outliers are shown as red + symbols, number of samples

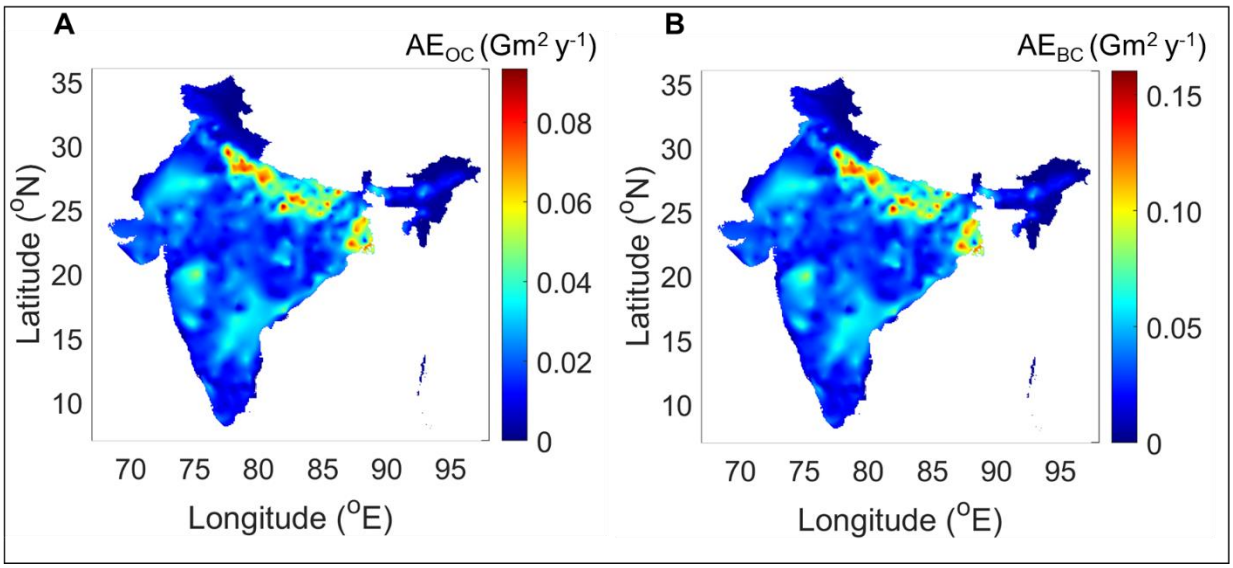

Figure 6.11: Spatial distribution of annual emissions expressed as light absorption cross-section (AE: Gm^2y^{-1}) at 550 nm attributed to (A) OC and (B) BC components of cookstoves emissions in India. BC AAE = 1.2 was used.

6.3.3. Intensive optical properties of OC and their radiative impact

Estimating radiative impact of emissions requires optical cross-sections normalized to pollutant mass. Average MAC values for OC emissions and the contribution of OC to total light absorption, integrated over solar irradiance in 350-900 nm wavelength range, are reported in Table 6.3. We further calculated PM MAC values with and without OC absorption (distribution plots are in Appendix A3) to evaluate the contribution of OC to direct radiative forcing by cookstove emissions. MAC_{PM} values have an approximately lognormal distribution with average and 95% confidence intervals of 0.54 (0.10-1.46) m^2g^{-1}. When OC light absorption is set to zero, $MAC_{PM,no-OC}$ can be calculated by normalizing the remaining (BC only) absorption to PM mass. This quantity depends on the assumed values of BC AAE and also exhibits a lognormal distribution with a large spread. Mean values of $MAC_{PM,no-OC}$ ranged 0.39-0.45 m^2g^{-1}. The large, overlapping ranges of MAC_{PM} and $MAC_{PM,no-OC}$ pose a challenge in constraining OC contribution to direct forcing. However, these parameters do not vary independently of each other: at 550 nm wavelength, higher

absorption efficiencies of cookstove emissions are associated with a larger contribution from BC (Figure 6.13A). In other words, MAC_{PM} and $MAC_{PM,no\text{-}OC}$ are positively correlated and their dependence can be captured by a linear relationship (Figure 6.13B).

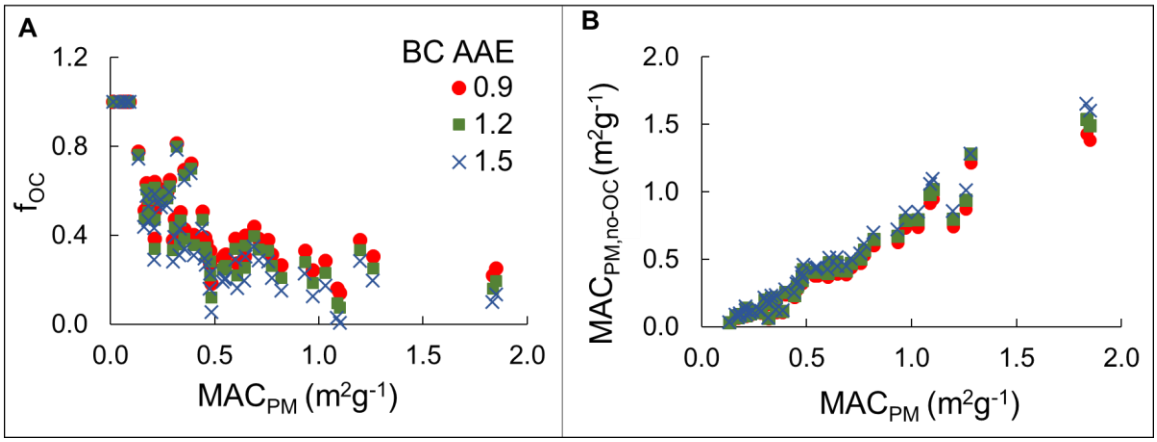

Figure 6.12: (A) The contribution of OC light absorption to MAC_{PM} at 550 nm, f_{OC}, decreases with increasing values of MAC_{PM}. This implies that (B) $MAC_{PM.no\text{-}OC}$ is positively correlated with MAC_{PM}. Linear fits between the two parameters are in Table 6.2.

Table 6.2: Slope (m), intercept (c) and adjusted R^2 for the linear fits: $MAC_{PM,no\text{-}OC}$ =m* MAC_{PM} + c.

	BC AAE		
	0.9	1.2	1.5
m	0.82	0.88	0.94
c	-0.09	-0.09	-0.1
Adjusted R^2	0.97	0.97	0.97

This correlation (Table 6.2) was exploited for forcing calculations. MAC_{PM} was sampled from the distribution observed (Appendix A3), then $MAC_{PM,no\text{-}OC}$ was calculated from the linear fit above. Bounds for cookstove emissions mass scattering cross-section (MSC) values were taken from measurements on traditional south Asian *chulhas* (Weyant et al., 2019) as 1.5-2.5 m^2g^{-1}. Simple forcing efficiency (SFE) was calculated as a function of MAC and MSC (Bond and Bergstrom,

2006). While the magnitude of SFE is dependent on the choice of MSC, for a fixed MSC, change in SFE due to OC light absorption (SFE_{PM} -$SFE_{PM,no\text{-}OC}$) only depends on the respective MAC values. OC contributions to SFE are reported as a function of the BC AAE used for absorption apportionment in Table 6.3. OC absorption added 8.6-12.1 Wg^{-1} to forcing over ground and 36.3-51.5 Wg^{-1} to forcing over snow by fresh cookstove emissions. For MSC = 1.5 m^2g^{-1}, SFE for cookstoves $PM_{2.5}$ emissions over ground was estimated as 11±23 Wg^{-1}. Using the mean value of this estimate, we observe that if all cookstove OC was non-absorbing, it would purely offset BC forcing, leading to a mean net forcing efficiency of -1.1-2.4 Wg^{-1}. Distributions of SFE estimates with and without OC absorption and those of SFE attributed to OC are in Appendix A3.

Table 6.3: Simple forcing efficiency of cookstove emissions attributed to OC light absorption (in Wg^{-1} $PM_{2.5}$), MAC_{OC} (in Wg^{-1} PM), AAE_{OC}, and contribution of OC to $PM_{2.5}$ light absorption (percentage of total absorption). These estimates depend on the value of BC AAE used in absorption apportionment. All values are reported as mean±1 standard deviation.

		BC AAE		
		0.9	1.2	1.5
SFE attributed to OC (Wg^{-1})	ground	12.1±3.9	10.3±2.6	8.6±1.3
	snow	51.4±16.9	43.9±11.3	36.3±5.7
MAC_{OC} (m^2g^{-1})	550 nm	0.41±0.33	0.36±0.26	0.29±0.20
	350 nm	2.79±1.89	2.53±1.69	2.21±1.54
AAE_{OC} (350-700 nm)		5.8±1.3	5.9±1.3	6.0±1.8
Integrated (350-900 nm) OC contribution to light absorption (%)		56 ±26	52 ±28	48 ±30

6.4. Comparison with findings in literature

Absorption and scattering cross-sections of $PM_{2.5}$ emitted from cookstoves are compared in Table 6.4. The measurement wavelengths differed in these studies, but the reported AAE values can be used to compare the findings. With the improved filter artifact correction method, we find lower average MAC values than our results in Pandey et al. (2016). Our estimates are also significantly

lower than those reported from filter-based measurements in other studies but close to those from the PAS measurements (Stockwell et al., 2016; Jayarathne et al., 2018), which range 0.1-0.6 at 550 nm (extrapolated from observations at 405 nm using reported AAE values). In to the findings included in the table below, Stockwell et al. (2016) also measured absorption at 870 nm. This measurement was used to apportion total absorption to BC and OC, using a BC AAE of 1, yielding an estimate of 80-93% OC contribution to particle light absorption at 405 nm. Our estimates of the corresponding OC contribution range 50-70%. Weyant et al., (2019) used a linear regression model with an interaction term to express the total AEF as a function of the mass emission factors of OC and EC:

$$AEF_{PM} = a_1 EF_{EC} + a_2 EF_{OC} + a_3 EF_{EC} * EF_{OC} \quad (6.13)$$

The coefficients of regressions a1 and a2 may be taken to represent MAC values of EC and OC, respectively but the presence of the interaction term complicates this interpretation. Given the complex interplay between combustion conditions, EC and OC abundance in the resulting emissions and their associated absorption efficiencies, the explanatory power of such an analysis is uncertain. With that caveat, we note the estimated ~10% OC contribution to light absorption at 530 nm in the above study, compared to an estimate of ~40% in our work.

Table 6.4: Summary of optical cross-sections of particulate emissions from biomass cookstoves.

Study	Absorption measurement method	MAC (m^2g^{-1})[a]	AAE	MSC (m^2g^{-1})[a]
Roden et al. (2006)	PSAP, Bond et al. (1999) correction	2.8[b] 530 nm	1.8[c]	2.2[b] 530 nm
Habib et al. (2008)	Integrating plate, Bond et al. (1999) correction	0.5-2.7[d] 525 nm	0-3.4[d]	-
Pandey et al. (2016)	UV-vis spectrometer, Zhong and Jang (2011) constant correction factor	0.5-1.3[d] 550 nm	2.4-3.6[d]	-
Stockwell et al. (2016)	PAS	0.4[e,g], 1.5[f,g] 405 nm	3.0[e], 4.6[f]	3.7 [e,g], 3.4[f,g]
Weyant et al. (2019)	PSAP, Bond et al. (1999) correction	1.6-6.6[h,i] 530 nm	1.6-2.3[h]	1.7-3.0[h] 530 nm
Pandey et al. (2019a)	UV-vis spectrometer, Pandey et al. (2019a) correction	0.36-0.7[j] 550 nm	2.7-3.0[j]	-

[a]Wavelength for each measurement is specified
[b]Mean values for wood burning Honduran cookstoves. Standard deviations are ~0.6
[c]AAE reported by Chen et al., 2011 (an extended analysis of observations from Roden et al., 2006)
[d]Range of values reported from field cookstove tests involving various common biomass fuels (wood, agricultural residues and dung)
[e]MAC, AAE and MSC for dung cooking fires
[f]MAC, AAE and MSC for wood cooking fires
[g]MAC and MSC were estimated by combining absorption and scattering emission factors, respectively, with corresponding PM emission factors reported in Jayarathne et al., 2018 (based on the same field study)
[h]Range of values reported from field tests of South Asian chulhas, not speciated by fuel type
[i]MAC_{PM} estimated from reported values of MAC_{EC} using the EC and PM emission factors provided
[d]Range of values reported from field cookstove tests involving various common biomass fuels. MAC values showed the trend: dung<wood<agricultural residue

We suggest the use of MAC_{OC} = 0.3-0.5 m^2g^{-1} at 550 nm and AAE_{OC} = 6 for emissions from traditional Indian cookstoves. Given the link between combustion conditions and OC light absorption (Saleh et al., 2014; Saleh et al., 2018), these values could also represent other biomass combustion sources with BC/OC ratios ~0.1-0.2. Recent global radiative models that evaluated the

enhancement in aerosol light absorption due to OC (Feng et al., 2013; Wang et al., 2014) assumed that a fraction (50-66%) of the OC is light-absorbing and derived the index of refraction of this component using reported absorption efficiencies of solvent extracted OC particles . When normalized to the mass of all OC (as in this work), the absorption cross-sections employed in these studies ranged 0.05-0.47 m^2g^{-1} at 550 nm and 1.50-2.27 m^2g^{-1} at 350 nm. Cookstove emitted OC has an absorption efficiency comparable to that of "strongly absorbing" type of OC modeled in (Feng et al., 2013), which was linked with shifting the net global radiative forcing of organic aerosols from cooling to warming. Likewise, our simple forcing calculations suggest that OC light absorption could tip the net impact of carbonaceous cookstove emissions to positive direct forcing.

References

Andreae, M. and Gelencsér, A.: Black carbon or brown carbon? The nature of light-absorbing carbonaceous aerosols, Atmos. Chem. Phys., 6, 3131-3148, 2006.

Arnott, W. P., Hamasha, K., Moosmüller, H., Sheridan, P. J., and Ogren, J. A.: Towards aerosol light-absorption measurements with a 7-wavelength aethalometer: Evaluation with a photoacoustic instrument and 3-wavelength nephelometer, Aerosol Sci. Technol., 39, 17-29, 2005.

Aurell, J., Gullett, B. K., and Tabor, D.: Emissions from southeastern US Grasslands and pine savannas: Comparison of aerial and ground field measurements with laboratory burns, Atmos. Environ., 111, 170-178, 2015.

Bond, T. C., Anderson, T. L., and Campbell, D.: Calibration and intercomparison of filter-based measurements of visible light absorption by aerosols, Aerosol Sci. Technol., 30, 582-600, 1999.

Bond, T. C. and Bergstrom, R. W.: Light absorption by carbonaceous particles: An investigative review, Aerosol Sci. Technol., 40, 27-67, 2006.

Bond, T. C., Doherty, S. J., Fahey, D., Forster, P., Berntsen, T., DeAngelo, B., Flanner, M., Ghan, S., Kärcher, B., and Koch, D.: Bounding the role of black carbon in the climate system: A scientific assessment, J. Geophys. Res.: Atmos., 118, 5380-5552, 2013.

Cappa, C. D., Lack, D. A., Burkholder, J. B., and Ravishankara, A.: Bias in filter-based aerosol light absorption measurements due to organic aerosol loading: Evidence from laboratory measurements, Aerosol Sci. Technol., 42, 1022-1032, 2008.

Cappa, C. D., Onasch, T. B., Massoli, P., Worsnop, D. R., Bates, T. S., Cross, E. S., Davidovits, P., Hakala, J., Hayden, K. L., and Jobson, B. T.: Radiative absorption enhancements due to the mixing state of atmospheric black carbon, Science, 337, 1078-1081, 2012.

Cappa, C. D., Onasch, T. B., Massoli, P., Worsnop, D. R., Bates, T. S., Cross, E. S., Davidovits, P., Hakala, J., Hayden, K. L., and Jobson, B. T.: Response to comment on" Radiative absorption enhancements due to the mixing state of atmospheric black carbon", Science, 339, 393-393, 2013.

Carmichael, G. R., Adhikary, B., Kulkarni, S., D'Allura, A., Tang, Y., Streets, D., Zhang, Q., Bond, T. C., Ramanathan, V., and Jamroensan, A.: Asian aerosols: current and year 2030 distributions and implications to human health and regional climate change, Environ. Sci. Technol., 43, 5811-5817, 2009.

Census: Houselisting and Housing Census Data Office of The Registrar General and Census Commissioner, M. o. H. A., Goverment of India. (Ed.), New Delhi., 2011.

Chakrabarty, R., Moosmüller, H., Chen, L.-W., Lewis, K., Arnott, W., Mazzoleni, C., Dubey, M., Wold, C., Hao, W., and Kreidenweis, S.: Brown carbon in tar balls from smoldering biomass combustion, Atmos. Chem. Phys., 10, 6363-6370, 2010.

Chakrabarty, R. K., Pervez, S., Chow, J. C., Watson, J. G., Dewangan, S., Robles, J., and Tian, G.: Funeral pyres in South Asia: Brown carbon aerosol emissions and climate impacts, Environmental Science & Technology Letters, 1, 44-48, 2014.

Chen, Y.: Characterization of carbonaceous aerosols from biofuel combustion: emissions and climate relevant properties, 2011. Lawrence Berkeley National Laboratory, 2011.

Chen, Y. and Bond, T.: Light absorption by organic carbon from wood combustion, Atmos. Chem. Phys., 10, 1773-1787, 2010.

Chen, Y., Roden, C. A., and Bond, T. C.: Characterizing biofuel combustion with patterns of real-time emission data (PaRTED), Environ. Sci. Technol., 46, 6110-6117, 2012.
Cheng, Y., He, K.-b., Du, Z.-y., Engling, G., Liu, J.-m., Ma, Y.-l., Zheng, M., and Weber, R. J.: The characteristics of brown carbon aerosol during winter in Beijing, Atmos. Environ., 127, 355-364, 2016.
Chow, J. C., Watson, J. G., Chen, L.-W. A., Chang, M. O., Robinson, N. F., Trimble, D., and Kohl, S.: The IMPROVE_A temperature protocol for thermal/optical carbon analysis: maintaining consistency with a long-term database, Journal of the Air & Waste Management Association, 57, 1014-1023, 2007.
Chow, J. C., Watson, J. G., Robles, J., Wang, X. L., Chen, L.-W. A., Trimble, D. L., Kohl, S. D., Tropp, R. J., and Fung, K. K.: Quality assurance and quality control for thermal/optical analysis of aerosol samples for organic and elemental carbon, Analytical and Bioanalytical Chemistry, 401, 3141-3152, 2011.
Chowdhury, S., Dey, S., Guttikunda, S., Pillarisetti, A., Smith, K. R., and Di Girolamo, L.: Indian annual ambient air quality standard is achievable by completely mitigating emissions from household sources, Proceedings of the National Academy of Sciences, 2019. 201900888, 2019.
Chung, C. E., Lee, K., and Müller, D.: Effect of internal mixture on black carbon radiative forcing, Tellus B, 64, 2011.
Chung, C. E., Ramanathan, V., and Decremer, D.: Observationally constrained estimates of carbonaceous aerosol radiative forcing, Proceedings of the National Academy of Sciences, 109, 11624-11629, 2012.
David, L. M., Ravishankara, A., Kodros, J. K., Venkataraman, C., Sadavarte, P., Pierce, J. R., Chaliyakunnel, S., and Millet, D. B.: Aerosol optical depth over India, J. Geophys. Res.: Atmos., 123, 3688-3703, 2018.
Davies, N. W., Fox, C., Szpek, K., Cotterell, M. I., Taylor, J. W., Allan, J. D., Williams, P. I., Trembath, J., Haywood, J. M., and Langridge, J. M.: Evaluating biases in filter-based aerosol absorption measurements using photoacoustic spectroscopy, Atmos. Meas. Tech. Discuss., 2019, 1-38, 2019.
Drinovec, L., Močnik, G., Zotter, P., Prévôt, A., Ruckstuhl, C., Coz, E., Rupakheti, M., Sciare, J., Müller, T., and Wiedensohler, A.: The" dual-spot" Aethalometer: an improved measurement of aerosol black carbon with real-time loading compensation, Atmos. Meas. Tech. Discuss., 7, 10179-10220, 2014.
Feng, Y., Ramanathan, V., and Kotamarthi, V.: Brown carbon: a significant atmospheric absorber of solar radiation?, Atmos. Chem. Phys., 13, 8607-8621, 2013.
Gyawali, M., Arnott, W., Lewis, K., and Moosmüller, H.: In situ aerosol optics in Reno, NV, USA during and after the summer 2008 California wildfires and the influence of absorbing and non-absorbing organic coatings on spectral light absorption, Atmos. Chem. Phys., 9, 8007-8015, 2009.
Gyawali, M., Arnott, W. P., Zaveri, R. A., Song, C., Pekour, M., Flowers, B., Dubey, M. K., Setyan, A., Zhang, Q., and Harworth, J.: Evolution of multispectral aerosol optical properties in a biogenically-influenced urban environment during the CARES campaign, Atmospheric Chemistry and Physics Discussions, 13, 7113-7150, 2013.
Habib, G., Venkataraman, C., Bond, T. C., and Schauer, J. J.: Chemical, microphysical and optical properties of primary particles from the combustion of biomass fuels, Environ. Sci. Technol., 42, 8829-8834, 2008.

Holder, A., Gullett, B., Urbanski, S., Elleman, R., O'Neill, S., Tabor, D., Mitchell, W., and Baker, K.: Emissions from prescribed burning of agricultural fields in the Pacific Northwest, Atmos. Environ., 166, 22-33, 2017.

Jain, S. K. and Kumar, V.: Trend analysis of rainfall and temperature data for India, Current Science(Bangalore), 102, 37-49, 2012.

Jayarathne, T., Stockwell, C. E., Bhave, P. V., Praveen, P. S., Rathnayake, C. M., Islam, M., Panday, A. K., Adhikari, S., Maharjan, R., and Goetz, J. D.: Nepal Ambient Monitoring and Source Testing Experiment (NAMaSTE): emissions of particulate matter from wood-and dung-fueled cooking fires, garbage and crop residue burning, brick kilns, and other sources, Atmos. Chem. Phys., 18, 2259-2286, 2018.

Khavse, R., Deshmukh, R., Manikandan, N., Chaudhary, J., and Khaushik, D.: Statistical Analysis of Temperature and Rainfall Trend in Raipur District of Chhattisgarh, Current World Environment, 10, 305-312, 2014.

Kirchstetter, T. W., Novakov, T., and Hobbs, P. V.: Evidence that the spectral dependence of light absorption by aerosols is affected by organic carbon, J. Geophys. Res.: Atmos., 109, 2004.

Kirchstetter, T. W. and Thatcher, T.: Contribution of organic carbon to wood smoke particulate matter absorption of solar radiation, Atmos. Chem. Phys., 12, 6067-6072, 2012.

Lack, D. and Langridge, J.: On the attribution of black and brown carbon light absorption using the Ångström exponent, Atmos. Chem. Phys., 13, 10535-10543, 2013.

Lack, D. A., Cappa, C. D., Covert, D. S., Baynard, T., Massoli, P., Sierau, B., Bates, T. S., Quinn, P. K., Lovejoy, E. R., and Ravishankara, A.: Bias in filter-based aerosol light absorption measurements due to organic aerosol loading: Evidence from ambient measurements, Aerosol Sci. Technol., 42, 1033-1041, 2008.

Lack, D. A., Langridge, J. M., Bahreini, R., Cappa, C. D., Middlebrook, A. M., and Schwarz, J. P.: Brown carbon and internal mixing in biomass burning particles, Proceedings of the National Academy of Sciences, 109, 14802-14807, 2012.

Laskin, A., Laskin, J., and Nizkorodov, S. A.: Chemistry of Atmospheric Brown Carbon, Chem. Rev., 115, 4335-4382, 2015.

Liu, C., Chung, C. E., Yin, Y., and Schnaiter, M.: The absorption Ångström exponent of black carbon: from numerical aspects, Atmos. Chem. Phys., 18, 6259-6273, 2018.

Liu, J., Bergin, M., Guo, H., King, L., Kotra, N., Edgerton, E., and Weber, R.: Size-resolved measurements of brown carbon in water and methanol extracts and estimates of their contribution to ambient fine-particle light absorption, Atmos. Chem. Phys., 13, 12389-12404, 2013.

MacCarty, N., Ogle, D., Still, D., Bond, T., and Roden, C.: A laboratory comparison of the global warming impact of five major types of biomass cooking stoves, Energy for sustainable development, 12, 56-65, 2008.

Murali, J. and Afifi, T.: Rainfall variability, food security and human mobility in the Janjgir-Champa district of Chhattisgarh state, India, Climate and Development, 6, 28-37, 2014.

Pandey, A., Hsu, A., Pervez, S., and Chakrabarty, R. K.: Light absorption by organic aerosol emissions rivals that of black carbon from residential biomass fuels in south Asia. Manuscript submitted for publication, 2019a.

Pandey, A., Patel, S., Pervez, S., Tiwari, S., Yadama, G., Chow, J. C., Watson, J. G., Biswas, P., and Chakrabarty, R. K.: Aerosol emissions factors from traditional biomass cookstoves in India: insights from field measurements, Atmos. Chem. Phys., 17, 13721-13729, 2017.

Pandey, A., Pervez, S., and Chakrabarty, R. K.: Filter-based measurements of UV–vis mass absorption cross sections of organic carbon aerosol from residential biomass combustion: Preliminary findings and sources of uncertainty, J. Quant. Spectrosc. Radiat. Transfer, 182, 296-304, 2016.

Pandey, A., Sadavarte, P., Rao, A. B., and Venkataraman, C.: Trends in multi-pollutant emissions from a technology-linked inventory for India: II. Residential, agricultural and informal industry sectors, Atmos. Environ., 99, 341-352, 2014.

Pandey, A., Shetty, N. J., and Chakrabarty, R. K.: Aerosol light absorption from optical measurements of PTFE membrane filter samples: sensitivity analysis of optical depth measures, Atmos. Meas. Tech., 12, 1365-1373, 2019b.

Parashar, D., Gadi, R., Mandal, T., and Mitra, A.: Carbonaceous aerosol emissions from India, Atmos. Environ., 39, 7861-7871, 2005.

Petzold, A., Ogren, J., Fiebig, M., Laj, P., Li, S.-M., Baltensperger, U., Holzer-Popp, T., Kinne, S., Pappalardo, G., and Sugimoto, N.: Recommendations for reporting" black carbon" measurements, Atmos. Chem. Phys., 13, 8365-8379, 2013.

Pitchford, M., Malm, W., Schichtel, B., Kumar, N., Lowenthal, D., and Hand, J.: Revised algorithm for estimating light extinction from IMPROVE particle speciation data, Journal of the Air & Waste Management Association, 57, 1326-1336, 2007.

Pokhrel, R. P., Beamesderfer, E. R., Wagner, N. L., Langridge, J. M., Lack, D. A., Jayarathne, T., Stone, E. A., Stockwell, C. E., Yokelson, R. J., and Murphy, S. M.: Relative importance of black carbon, brown carbon, and absorption enhancement from clear coatings in biomass burning emissions, Atmos. Chem. Phys., 17, 5063-5078, 2017.

Ramanathan, V. and Carmichael, G.: Global and regional climate changes due to black carbon, Nature geoscience, 1, 221-227, 2008.

Ramanathan, V., Crutzen, P., Kiehl, J., and Rosenfeld, D.: Aerosols, climate, and the hydrological cycle, Science, 294, 2119-2124, 2001.

Roden, C. A., Bond, T. C., Conway, S., and Pinel, A. B. O.: Emission factors and real-time optical properties of particles emitted from traditional wood burning cookstoves, Environ. Sci. Technol., 40, 6750-6757, 2006.

Roden, C. A., Bond, T. C., Conway, S., Pinel, A. B. O., MacCarty, N., and Still, D.: Laboratory and field investigations of particulate and carbon monoxide emissions from traditional and improved cookstoves, Atmos. Environ., 43, 1170-1181, 2009.

Saleh, R., Cheng, Z., and Atwi, K.: The brown–black continuum of light-absorbing combustion aerosols, Environ. Sci. Technol. Lett., 5, 508-513, 2018.

Saleh, R., Hennigan, C., McMeeking, G., Chuang, W., Robinson, E., Coe, H., Donahue, N., and Robinson, A.: Absorptivity of brown carbon in fresh and photo-chemically aged biomass-burning emissions, Atmos. Chem. Phys., 13, 7683-7693, 2013.

Saleh, R., Robinson, E. S., Tkacik, D. S., Ahern, A. T., Liu, S., Aiken, A. C., Sullivan, R. C., Presto, A. A., Dubey, M. K., and Yokelson, R. J.: Brownness of organics in aerosols from biomass burning linked to their black carbon content, Nature Geoscience, 7, 647-650, 2014.

Sastri, A.: Long range regional climate fluctu-ations/changes and their impacts on agriculture: A case study for Chhattisgarh State in Central India, 2009, W3.

Saud, T., Gautam, R., Mandal, T., Gadi, R., Singh, D., Sharma, S., Dahiya, M., and Saxena, M.: Emission estimates of organic and elemental carbon from household biomass fuel used over the Indo-Gangetic Plain (IGP), India, Atmos. Environ., 61, 212-220, 2012.

Schnaiter, M., Gimmler, M., Llamas, I., Linke, C., Jäger, C., and Mutschke, H.: Strong spectral dependence of light absorption by organic carbon particles formed by propane combustion, Atmos. Chem. Phys., 6, 2981-2990, 2006.

Stockwell, C. E., Christian, T. J., Goetz, J. D., Jayarathne, T., Bhave, P. V., Praveen, P. S., Adhikari, S., Maharjan, R., DeCarlo, P. F., and Stone, E. A.: Nepal Ambient Monitoring and Source Testing Experiment (NAMaSTE): emissions of trace gases and light-absorbing carbon from wood and dung cooking fires, garbage and crop residue burning, brick kilns, and other sources, Atmos. Chem. Phys., 16, 11043-11081, 2016.

Strand, T., Gullett, B., Urbanski, S., O'Neill, S., Potter, B., Aurell, J., Holder, A., Larkin, N., Moore, M., and Rorig, M.: Grassland and forest understorey biomass emissions from prescribed fires in the south-eastern United States–RxCADRE 2012, International Journal of Wildland Fire, 25, 102-113, 2016.

Subramanian, R., Roden, C. A., Boparai, P., and Bond, T. C.: Yellow beads and missing particles: Trouble ahead for filter-based absorption measurements, Aerosol Sci. Technol., 41, 630-637, 2007.

Sun, H., Biedermann, L., and Bond, T. C.: Color of brown carbon: A model for ultraviolet and visible light absorption by organic carbon aerosol, Geophys. Res. Lett., 34, 2007.

Turpin, B. J. and Lim, H.-J.: Species contributions to PM2. 5 mass concentrations: Revisiting common assumptions for estimating organic mass, Aerosol Sci. Technol., 35, 602-610, 2001.

Venkataraman, C., Habib, G., Eiguren-Fernandez, A., Miguel, A., and Friedlander, S.: Residential biofuels in South Asia: carbonaceous aerosol emissions and climate impacts, Science, 307, 1454-1456, 2005.

Wang, X., Heald, C., Ridley, D., Schwarz, J., Spackman, J., Perring, A., Coe, H., Liu, D., and Clarke, A.: Exploiting simultaneous observational constraints on mass and absorption to estimate the global direct radiative forcing of black carbon and brown carbon, Atmos. Chem. Phys., 14, 10989-11010, 2014.

Washenfelder, R., Attwood, A., Brock, C., Guo, H., Xu, L., Weber, R., Ng, N., Allen, H., Ayres, B., and Baumann, K.: Biomass burning dominates brown carbon absorption in the rural southeastern United States, Geophys. Res. Lett., 42, 653-664, 2015.

Watson, A. Y. and Valberg, P. A.: Carbon black and soot: two different substances, AIHAJ-American Industrial Hygiene Association, 62, 218-228, 2001.

Weingartner, E., Saathoff, H., Schnaiter, M., Streit, N., Bitnar, B., and Baltensperger, U.: Absorption of light by soot particles: determination of the absorption coefficient by means of aethalometers, J. Aerosol Sci, 34, 1445-1463, 2003.

Weyant, C. L., Chen, P., Vaidya, A., Li, C., Zhang, Q., Thompson, R., Ellis, J., Chen, Y., Kang, S., and Shrestha, G. R.: Emission measurements from traditional biomass cookstoves in South Asia and Tibet, Environ. Sci. Technol., 2019. 2019.

Xie, M., Hays, M. D., and Holder, A. L.: Light-absorbing organic carbon from prescribed and laboratory biomass burning and gasoline vehicle emissions, Scientific reports, 7, 7318, 2017.

Zhong, M. and Jang, M.: Light absorption coefficient measurement of SOA using a UV–Visible spectrometer connected with an integrating sphere, Atmos. Environ., 45, 4263-4271, 2011.

Chapter 7: Conclusions

7.1. BC optical parameterization

To bridge the gap between optical models that explicitly handle the fractal morphology of BC aggregates and radiative models that assume spherical morphology for all aerosols, I have developed relationships between numerically-exact calculations of BC optical properties and equivalent aerosol (mobility, mass equivalent and vacuum aerodynamic) diameters, for freshly emitted and aged aggregates. The above descriptors of particle size are measured by widely used aerosol instrumentation such as SMPS, SP2, and the SP-AMS. A major finding was that a larger fractal dimension (representing atmospherically aged BC) corresponds to more intense interactions between monomers, from a more compact structure, and usually serves to intensify the variation of radiative properties with aggregate size. One critical area for future research is to assess the range in BC refractive index upon coating of BC particles with organic and inorganic aerosols.

Radiative transfer models typically use the upscatter fraction to represent scattering directionality: β is estimated from asymmetry parameter calculated from Mie theory or the backscatter ratio measured using a nephelometer. An approximate analytical expression (the HG phase function) for the angular distribution of light scattered by small particles is commonly used to aid the above computations. I examined the applicability of relationships based on the HG phase function to fractal BC aggregates:

- Upscatter fractions derived using these approximate relationships are lower than its actual values.
- Improved parameterizations from my study can be used to connect the three directionality parameters for collapsed aggregates

- For open aggregates, analytical expressions cannot accurately describe the parameter relationships for large particles (mass equivalent diameter > 200 nm) because one-to-one relationships do not exist.

The error in β from use of approximate HG-based relationships could be up to 35%, the corresponding error in simple forcing efficiency is within 8%. Further evaluation is needed on the suitability of HG-based relationships for coated fractal aggregates and nonideally shaped particles like mineral dust.

7.2. Aerosol emissions from biomass cookstoves

My field study of traditional cookstove (*chulha*) performance in India, using a variety of regionally significant fuels showed that cookstoves are a larger culprit in particulate pollution in India than previously estimated (Pandey et al., 2014). The major findings from this study are:

- Emission factor differences for four types wood fuels from different regions of India were statistically insignificant because the variability in emissions for a given fuel type was comparable to the differences in average emission rates for different wood fuels. Agricultural residues and dung are associated with larger emissions than fuel-wood.
- Ignition and rekindling consistently produce much more emissions than steady flaming conditions. Real-time particle concentrations (based on light scattering) and CO concentration measurements fluctuate over a cooking cycle, in contrast with findings from laboratory studies.
- Ratios of fuel-wise cookstove PM emission factors from our field study to those in the SMOG inventory (an average of best available values published till date) ranged 2.2-2.5, while those for OC emission factors ranged 2.5-4.2. Other recent field evaluations of cookstove performance support these findings: on average, real-world $PM_{2.5}$, OC

and EC emission factors are larger than their counterparts from simulated cooking cycles (water boiling test) by factors of 2.1, 1.5 and 3.1, respectively

- Over field and WBT studies, OC mass constituted approximately 60% of the total particle mass. This indicates that studies that understimate PM emission factors likely use cooking cycles characterized by more frequent strong flaming conditions than actual cooking.

7.3. Filter artifact correction for UV-vis spectroscopy on Teflon membrane filters

Teflon filters are routinely used for gravimetric and elemental analysis across monitoring networks and field and laboratory source characterization studies. UV-vis spectrophotometers are used to measure transmittance and reflectance measurements for these filters, in order to estimate the absorption properties of deposited particles. Artifacts associated with this estimation are not well-characterized. I compared *in-situ* aerosol light-absorption observations with optical measurements made on concurrently collected filter samples, Through radiative transfer modeling, I assessed the suitability of three measures of filter-based optical depth for robustly describing particulate-phase light absorption over a range of single scattering albedo (SSA) values: (1) OD_s–a measure of transmission of the fraction of incident radiation that is not backscattered by the filter system–utilizes transmittance and reflectance of the sample side of the filter, (2) the commonly-used OD_c uses transmittance and reflectance of the clean side of the filter, and (3) *ATN* or the Beer-Lambert attenuation. The key findings were:

- OD_s showed the least sensitivity to SSA, for fixed filter loading. Therefore, this measure is the best choice for estimating aerosol light absorption from filter optical measurements for a wide range of aerosol types.

- A simple, wavelength-independent formulation can be used for calculating aerosol MAC and absorption coefficients from measurements of OD_s.
- The ratio between in-situ particulate absorption optical depth and OD_s is inversely proportional to aerosol SSA.

In many measurement systems, such as the Hybrid Integrating Plate and Sphere method (Bond et al., 1999) used by the IMPROVE network, transmittance and reflectance are measured on the clean side of the filter and the optical depth OD_c is calculated (Campbell et al., 1995; White et al., 2016). The relationship between aerosol optical depth, $\tau_{a,s}$, and OD_c showed a larger variability across varying SSA than that between $\tau_{a,s}$ and OD_s. Therefore, we suggest further evaluation of OD_s as an optical depth measure that can be empirically connected to particulate phase light absorption for a range of aerosol types.

7.4. Light absorption by cookstove OC emissions

Climate models have conventionally neglected atmospheric light absorption by OC. Among the key inputs needed for in expanding the conventional discussion of aerosol climate impacts are MAC and AAE values for OC aerosols. OC physical and optical properties like refractoriness, polarity and crucially, absorption efficiency span a large inter-linked range, and show a dependence on combustion conditions. My analysis of in-use cookstove performance showed that cookstove PM emissions are dominated by thermally-stable OC indicating a potential for significant light absorption. I applied my recently-developed artifact correction scheme to optical measurements on the Teflon filter samples collected during the cookstove field study. I used a two-component model to apportion total particle light absorption to BC and OC, exploiting the difference in their spectral absorption dependences. I concluded that:

- OC contributes nearly as much as BC to light absorption by cookstove emissions at mid-visible wavelengths. This estimate is well-constrained with respect to the potential variability in BC AAE.
- Estimated MAC and AAE values of OC emissions are in agreement with those used for a "strongly absorbing" type of OC included in recent climate modeling exercises.
- OC light absorption has a significant positive contribution to the direct forcing efficiency of carbonaceous cookstove emissions.

Taken as a whole, my findings indicate that replacement of traditional cookstoves with clean technologies could mitigate aerosol related warming in addition to reducing particulate exposure and the associated disease burden (Chowdhury et al., 2019) in South Asia. However, if these clean technologies include advanced biomass stoves, improved laboratory testing (Chen et al., 2012) and field validation are crucial for evaluating the extent, if any, of the health and climate benefits of technology replacement. Light-absorbing OC should be addressed as a distinct short-lived-climate-forcing agent in discussions of cookstove impacts in India. These findings may also be applicable to other regions of Asia, as well as Africa and South America, where cooking with solid biomass fuels is prevalent.

References

Bond, T. C., Anderson, T. L., and Campbell, D.: Calibration and intercomparison of filter-based measurements of visible light absorption by aerosols, Aerosol Sci. Technol., 30, 582-600, 1999.

Campbell, D., Copeland, S., and Cahill, T.: Measurement of aerosol absorption coefficient from Teflon filters using integrating plate and integrating sphere techniques, Aerosol Sci. Technol., 22, 287-292, 1995.

Chen, Y., Roden, C. A., and Bond, T. C.: Characterizing biofuel combustion with patterns of real-time emission data (PaRTED), Environ. Sci. Technol., 46, 6110-6117, 2012.

Chowdhury, S., Dey, S., Guttikunda, S., Pillarisetti, A., Smith, K. R., and Di Girolamo, L.: Indian annual ambient air quality standard is achievable by completely mitigating emissions from household sources, Proceedings of the National Academy of Sciences, 2019. 201900888, 2019.

Pandey, A., Sadavarte, P., Rao, A. B., and Venkataraman, C.: Trends in multi-pollutant emissions from a technology-linked inventory for India: II. Residential, agricultural and informal industry sectors, Atmos. Environ., 99, 341-352, 2014.

White, W. H., Trzepla, K., Hyslop, N. P., and Schichtel, B. A.: A critical review of filter transmittance measurements for aerosol light absorption, and de novo calibration for a decade of monitoring on PTFE membranes, Aerosol Sci. Technol., 50, 984-1002, 2016.

Appendix

A1. Two-stream radiative transfer model

Consider the layer of filter in which sampled particles are embedded to be a one-dimensional uniform medium with an optical thickness τ_0, a single scattering albedo $\omega<1$ and a scattering asymmetry parameter g. Now, consider a 'forward' direction: at any point in the medium the energy intensity propagating in this direction is given by I_f. Conversely, the backward propagation intensity is I_b.

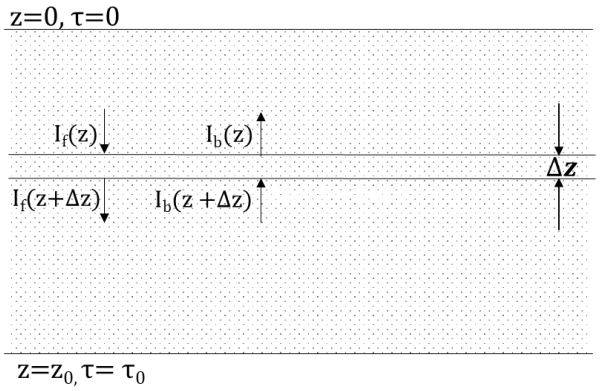

Figure A1.1: Transmission and reflection of radiation through a one-dimensional, uniformly multiple-scattering medium.

Energy conservation in the medium can be written as(Bohren, 1987):

$$\frac{d(I_f - I_b)}{d\tau} = -(1-\omega_0)(I_f + I_b) \quad \text{(A1.1a)}$$

$$\frac{d(I_f + I_b)}{d\tau} = -(1-\omega_0 g))(I_f - I_b) \quad \text{(A1.1b)}$$

The general solution of the above equations has the following form:

$$(I_f - I_b) = p_1 \exp(-K\tau) + p_2 \exp(K\tau) \quad \text{(A1.2a)}$$

$$(I_f + I_b) = q_1 \exp(-K\tau) + q_2 \exp(K\tau) \quad \text{(A1.2b)}$$

where $K = \sqrt{(1-\omega_0)(1-\omega_0 g)}$

Assume that the medium is (1) illuminated from the top: $I_f(\tau = 0) = I_0$ and (2) does not reflect at the opposite edge: $I_b(\tau = \tau_0) = 0$. Reflectance R_l and transmittance T_l of the medium are respectively defined as: $I_b(\tau = 0) = R_l$ and $I_f(\tau = \tau_0) = T_l$. With these boundary conditions, the constants p_1, p_2, q_1 and q_2 can be estimated. Then the quantities of interest, R_l and T_l, are given by(Arnott et al., 2005):

$$R_l = \frac{\omega_0(1-g)\sinh(K\tau_0)}{[2K-\omega_0(1-g)\sinh(K\tau_0)+2K\cosh(K\tau_0)]} \quad \text{(A1.3a)}$$

$$T_l = \frac{2}{[2K-\omega_0(1-g)\sinh(K\tau_0)+2K\cosh(K\tau_0)]} \quad \text{(A1.3b)}$$

The subscript *l* is used in the equations above to denote the properties of a composite aerosol-filter layer. τ_0 denotes the total optical depth of the layer:

$$\tau_0 = \tau_{e,l} = \tau_{e,f+}\tau_{a,s} + \tau_{sc,s} \quad \text{(A1.4)}$$

Subscripts *e*, *a* and *sc* denote extinction, absorption and scattering optical depths. The second subscript *f* corresponds to the portion of the filter that was penetrated by the aerosol, while *s* represents the aerosol sample. Equation (A1.4) can be rewritten as:

$$\tau_{e,l} = \chi\tau_{e,F+}\tau_{a,s}\left(\frac{1+SSA}{1-SSA}\right) \quad \text{(A1.5)}$$

where χ is the penetration depth of the aerosols in the filter (assumed 0.1 in this study). The optical depth of the filter in the first layer is proportional to the penetration depth and the optical depth of

a blank filter, $\tau_{e.F.}$ In equation A1.5, SSA is the single scattering albedo of the deposited aerosols. The single scattering albedo and asymmetry parameter of this composite layer are given by:

$$\omega_0 = \frac{\tau_{a,s}\left(\frac{SSA}{1-SSA}\right)+\chi\tau_{e,F}}{\tau_{a,s}\left(\frac{1+SSA}{1-SSA}\right)+\chi\tau_{e,F}} \quad \text{(A1.6)}$$

$$g = \frac{g_s \times \tau_{a,s}\left(\frac{SSA}{1-SSA}\right)+g_F \times \chi\tau_{e,F}}{\tau_{a,s}\left(\frac{SSA}{1-SSA}\right)+\chi\tau_{e,F}} \quad \text{(A1.7)}$$

The respective asymmetry parameters of the particles and filter are denoted by g_s and g_F. In this study, was g_s fixed at 0.6 (based on Martins et al. (1998); Reid et al. (2005)).

For the pristine portion of the filter (no aerosol embedded, therefore single scattering albedo is unity), the solution to Equations (A1.1a) and (A1.1b) is greatly simplified. The reflectance (*R2*) and transmittance (*T2*) of this layer is given by:

$$R_f = \frac{(1-\chi)\tau_F^*}{1+(1-\chi)\tau_F^*} \quad \text{(A1.8a)}$$

$$T_f = \frac{1}{1+(1-\chi)\tau_F^*} \quad \text{(A1.8b)}$$

where $\tau_F^* = \left(1 - g_F\right)\tau_F$ is estimated from the measurements of transmittance and reflectance through blank filters. Since a blank filter is non-absorbing, equations (A1.8a) and (A1.8b) can be applied to it, setting χ as zero (i.e. no loading). Measured transmittance through 20 lab blank PTFE membrane filters for wavelengths ranging 350-550 nm was 0.7±0.02. This range (2 standard deviations are ~6% around the mean) is slightly narrower than that (~10%) observed by White et al., 2016 for 534 passively exposed field blanks from the IMPROVE network. It is comparable to the variability in transmittance (~7%) of 150 clean blanks reported by Presler-Jur, 2017.

For T_{blank}=0.7, τ^*_F is calculated as:

$$\tau_F^* = \frac{1}{T_{blank}} - 1 = 0.43 \quad \text{(A1.9)}$$

This value of τ^*_F was used in the fixed blank optics assumption (as discussed in Chapter 1.5) when examining the sensitivity to filter optical measures to a given model input. Some calculations were also performed assuming a realistic range of randomly-varying blank filter properties.

It can be shown that all calculations in equations A1.3a through A1.8b require only τ^*_F and not τ_F and g_F. Therefore, any non-zero value can be assumed for τ_F and g_F can be calculated such that the value of τ^*_F is satisfied. With these filter properties (τ_F and g_F), and assumed aerosol penetration depth χ (see Figure 5.5 for sensitivity of model outputs to this parameter) and asymmetry parameter g_s, R_l, R_f, T_l and T_f were calculated for a range of aerosol properties ($\tau_{a,s}$ and SSA). Then, overall filter transmittance and reflectance, with light incident on the sample side of the filter, were estimated by performing an energy balance (Gorbunov et al., 2002):

$$T_s = \frac{T_l T_f}{1 - R_l R_f} \quad \text{(A1.10a)}$$

$$R_s = R_l + \frac{T_l^2 R_f}{1 - R_l R_f} \quad \text{(A1.10b)}$$

The optical behavior of PTFE filters was modeled for SSA varied between 0.2 and 0.99, and $\tau_{a,s}$ between 0 and 1. A surface plot of OD_s as a function of SSA and $\tau_{a,s}$ over the above input range is shown in Figure A1.2

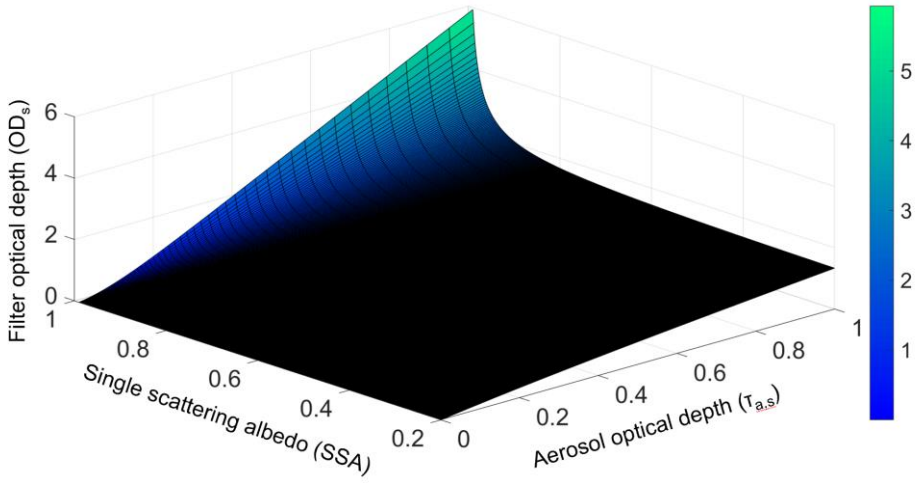

Figure A1.2: Modeled filter optical depth (OD_s) as a function of single scattering albedo (SSA) and aerosol optical depth ($\tau_{a,s}$) of deposited aerosols.

A2. List of aerosol emission factors by fuel and burn phase.

Table A2.1: Emission factors of $PM_{2.5}$, CO, OC and EC (in g pollutant kg^{-1} fuel) for each test fuel and combustion phase.

Fuel	Burn phase	Emission factor (g/kg fuel)			
		$PM_{2.5}$	CO	OC	EC
U.P. dung	Ignition	15	28	7.86	0.87
	Smoldering	28	121	20.40	1.41
	Smoldering	19	80	10.53	0.56
	Smoldering	8	54	5.62	0.05
	Ignition	11	35	0.38	0.00
	Steady flame	5	51	2.78	0.34
	Steady flame	5	39	2.81	0.73
Bihar dung	Ignition	62	10	7.92	0.92
	Steady flame	18	51	7.57	1.10
	Smoldering	35	172	25.23	2.39
	Ignition	32	103	20.55	1.17
	Smoldering	1	61	0.66	0.05
	Smoldering	4	41	1.97	0.19
Chh. rice straw	Ignition	31	110	10.44	0.01
	Smoldering	27	244	14.60	2.36
	Steady flame	17	75	12.12	3.64
	Steady flame	4	59	3.64	0.58
	Steady flame	4	57	3.45	0.47
	Steady flame	6	47	2.70	0.33
	Smoldering	5	55	2.60	0.42
Chh. t*ur* stalk	Ignition	7	129	0.80	0.00
	Steady flame	5	233	19.00	5.20
	Steady flame	15	163	2.96	0.59
	Ignition	32	144	16.37	4.02
	Steady flame	7	42	9.78	1.96
	Ignition	15	117	5.96	2.00
	Smoldering	12	142	3.74	0.26
	Ignition	4	0	4.43	3.88
	Steady flame	11	69	5.02	0.99
	Steady flame	30	72	12.82	0.68
Punjab wood	Ignition	3	68	0.80	0.68
	Steady flame	11	265	5.72	1.10
	Steady flame	3	142	0.69	0.07
	Steady flame	7	219	3.19	0.85
Raj. wood	Ignition	14	28	3.70	1.89

	Ignition	49	317	19.43	3.13
	Steady flame	16	239	9.53	2.53
	Steady flame	13	175	4.17	1.03
	Steady flame	8	153	3.05	0.61
	Smoldering	16	299	6.30	0.71
	Steady flame	32	123	12.56	2.61
	Steady flame	10	152	2.40	0.38
	Steady flame	0	117	0.00	0.00
	Ignition	7	150	5.04	1.23
	Smoldering	11	155	2.57	0.13
	Ignition	10	46	11.39	2.50
	Steady flame	7	65	3.30	0.50
	Steady flame	10	65	2.81	0.55
	Steady flame	5	48	3.86	1.19
	Steady flame	7	42	1.67	0.40
	Smoldering	0	17	0.09	0.01
U.P. wood	Steady flame	5	72	1.20	0.42
	Smoldering	3	148	3.02	0.67
	Smoldering	3	169	0.79	0.14
	Steady flame	4	317	3.90	1.29
	Steady flame	5	107	2.38	0.48
	Ignition	5	68	0.74	0.61
	Steady flame	5	135	1.86	0.26
	Smoldering	5	130	3.20	0.53
A.P. wood	Steady flame	3	39	1.47	0.18
	Ignition	15	136	9.42	0.82
	Steady flame	12	136	6.46	0.41
	Smoldering	6	124	2.70	0.41

A3. Radiative forcing efficiency of cookstove emissions: probability distributions

Probability density distributions of the MAC values for cookstove emissions, with and without OC absorption (respectively, MAC_{PM} and $MAC_{PM,no\text{-}OC}$) are shown in Figure A3.1. The distribution in panel A was combined with the empirical linear fits described in Chapter 6.3.3 to estimate $MAC_{PM,no\text{-}OC}$ as a function of MAC_{PM} for different assumptions of BC AAE.

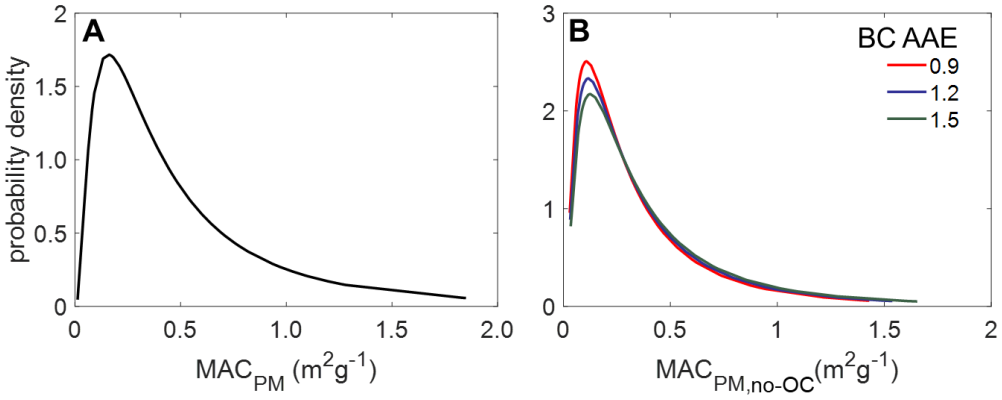

Figure A3.1: Probability distributions of (A) MAC_{PM} and (B) $MAC_{PM,no\text{-}OC}$ for all samples in this study.

Simple forcing efficiency (Wg^{-1} aerosol) is given by:

$$SFE = -\frac{1}{4}S(\lambda)\tau_{atm}^2(1-Fc)\times[2(1-\alpha_s)^2\beta.MSC(\lambda)-4\alpha_s.MAC(\lambda)] \quad \text{(A3.1)}$$

SFE calculations were performed for 550 nm wavelength (λ). The following atmospheric parameters were fixed: solar irradiance (S=1370 Wm^{-2}) atmospheric transmissivity (τ_{atm} = 0.79), cloud fraction (F_c=0.6) and surface albedo (α_s=0.19 for ground and 0.8 for snow). Particle upscatter fraction (β) was fixed at 0.15. With the above parameters fixed, SFE is a function of MAC and MSC values. MSC was not measured in this study but the relationship between OC light absorption

and SFE can be demonstrated by calculating SFE with MAC_{PM} and $MAC_{PM,no\text{-}OC}$, in turn. In Figure A3.2 S3, the distribution of SFE values over ground and snow for MSC=1.5m^2g^{-1} is shown.

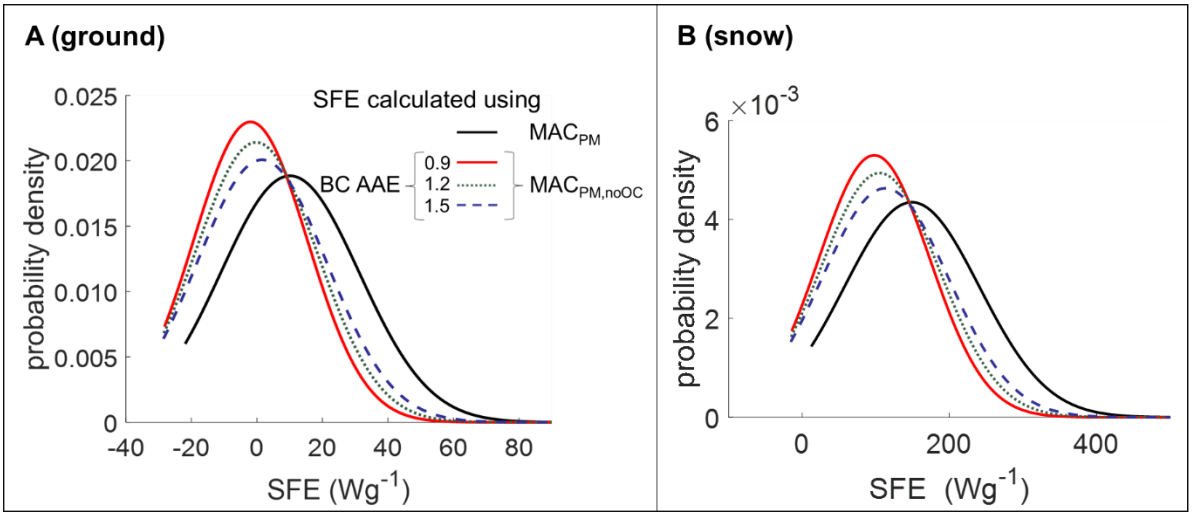

Figure A3.2: Probability distributions of simple forcing efficiency of cookstove particulate emissions over (A) ground and (B) snow. Forcing was calculated with and without OC light absorption, with a fixed MSC =1.5 m^2g^{-1}.

The difference between SFE_{PM} and $SFE_{PM,no\text{-}OC}$ depends only the difference in the respective MAC values:

$$SFE_{PM} - SFE_{PM,noOC} = S(\lambda)\tau_{atm}^2(1-Fc)\alpha_s \times \left[MAC_{PM}(\lambda) - MAC_{PM,noOC}(\lambda)\right] \quad \text{(A3.2)}$$

This difference can be interpreted as the contribution of OC light absorption to forcing by cookstove emissions. Estimated probability distributions of SFE attributed to OC light absorption are shown in Figure A3.3.

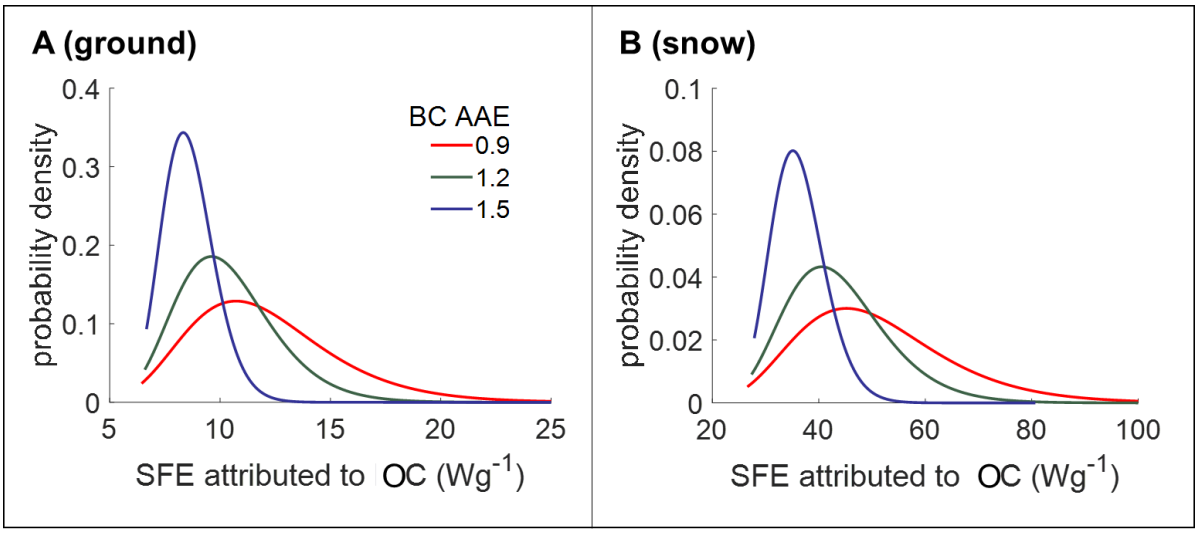

Figure A3.3: Probability distributions of simple forcing efficiency of cookstove particulate emissions attributed to OC light absorption over (A) ground and (B) snow.

References

Arnott, W. P., Hamasha, K., Moosmüller, H., Sheridan, P. J., and Ogren, J. A.: Towards aerosol light-absorption measurements with a 7-wavelength aethalometer: Evaluation with a photoacoustic instrument and 3-wavelength nephelometer, Aerosol Sci. Technol., 39, 17-29, 2005.

Bohren, C. F.: Multiple scattering of light and some of its observable consequences, Am. J. Phys, 55, 524-533, 1987.

Gorbunov, B., Hamilton, R., and Hitzenberger, R.: Modeling radiative transfer by aerosol particles on a filter, Aerosol Science & Technology, 36, 123-135, 2002.

Martins, J. V., Artaxo, P., Liousse, C., Reid, J. S., Hobbs, P. V., and Kaufman, Y. J.: Effects of black carbon content, particle size, and mixing on light absorption by aerosols from biomass burning in Brazil, Journal of Geophysical Research: Atmospheres, 103, 32041-32050, 1998.

Reid, J., Koppmann, R., Eck, T., and Eleuterio, D.: A review of biomass burning emissions part II: intensive physical properties of biomass burning particles, Atmos. Chem. Phys., 5, 799-825, 2005.